THESIS

Infrared studies on water ice distribution in the Taurus dark cloud

Koji MURAKAWA

Infrared studies on water ice distribution in the Taurus dark cloud

Koji Murakawa

Department of Astronomical Science,
Graduate University for Advanced Studies

Contents

Acknowledgement

I would like to thank Professor Norio Kaifu and Dr. Motohide Tamura of National Astronomical Observatory (NAO), who supervised me to fulfil this study. Their advice and encouragement have been indispensable for this thesis.

I also would like to express my thanks to Professor Shuji Sato and Dr. Testuya Nagata of Nagoya University as well as Dr. Naoto Kobayashi of NAO who provided me a chance to use their instrument at the telescopes in Wyoming and Arizona.

My thanks are also due to Dr. Masahiko Hayashi, Dr. Saeko Hayashi, Dr. Hideki Takami, member of the CIAO group and the IR seminar, and students in Nagoya University and Kyoto University.

Abstract

We have conducted near-infrared spectroscopy of 62 background stars toward Heiles Cloud 2 in Taurus. We have employed WIRO 2.3 m telescope and MLOF 1.5 m telescope with a low dispersion spectrometer, PASP2, which can simultaneously obtain the spectrum with wavelength range between 1.3 and 4.2 μm. For 55 out of 62 objects, visual extinction A_V and absorption depth of water ice τ_{ICE} have been estimated. The relationship between A_V and τ_{ICE} shows that τ_{ICE} can be detected for A_V>2~5 mag and τ_{ICE} increases with increasing of A_V. This result is consistent with that obtained Whittet et al. 1988, in which 17 field stars in the Taurus dark cloud were selected and A_V threshold is 3.3 mag and τ_{ICE} /A_V is 0.093.

In order to investigate the water ice distribution in the Heiles Cloud 2, the map, in which the τ_{ICE} toward the position of the objects are plotted, is made and is compared with the $C^{18}O$ (J=1-0) map obtained by millimeter observation (Sunada & Kitamura 1997). Water ice detection is strongly correlated with the $C^{18}O$ map: 4 sources of τ_{ICE}>0.5 are associated with the dense $C^{18}O$ filaments and clumps.

Simple geometrical structure of the cloud is modeled to explain the scatter in the A_V threshold. Density of dust in the ellipsoidal cloud is assumed to decrease with square of the distance from the cloud center. The result shows that A_V threshold varies from 2 to 5 magnitudes and τ_{ICE} increases with increasing A_V when the ratio of major to minor axis of the cloud is changed. The variation in the threshold is due to the different contribution of the water-containing, inner portion of the cloud along the line of sight. When the elongation is larger, the overall opacity increases while the contribution of the interior is smaller, and thus the threshold of water ice detection becomes larger.

The water ice features of field stars with sufficiently large water ice absorption is compared with each other. They have similar shapes in the absorption peak and 3.4 μm long wavelength wing. Thus the temperature and the chemical component of the dust appear to be fairly uniform in the Heiles Cloud 2. This is consistent with that there are no evidence of the strong UV source in Heiles Cloud 2.

The water ice feature of field stars is compared with that of deeply embeddedlow mass YSO. The YSOs show slightly deeper absorption at 3.4μm than the former. This suggests that the dust around the low mass

YSOs could be deformed to change the 3.4μm absorption feature in a similar manner observed in massive YSOs.

In addition, interstellar extinction for Heiles Cloud 2 is also discussed. We have found that the power law in the diffuse region with the standard index of 1.8 can be useed for the limited wavelength, between J and K, and between K and L′, but it cannot fit the obtained continuum spectra for the whole wavelength range between 1.3 and 4.2 μm. The indices of the power law of each object was determined by using E_{H-K} and $E_{K-L'}$; the mean value is about 2.6, apparently different from that in the diffuse region. This suggests that the property of the dust in Heiles Cloud 2 might be different from that in the standard diffuse region.

1. Introduction

1-1. Roles of interstellar dust in molecular cloud

Toward the end of their evolution, stars eject their materials in the outer shell. Those are mainly giants, super giants, and asymptotic giant branch (AGB) stars, whose temperature is as cool as 2,000~3,000K. The temperature decreases when the materials are separated away from the central star, and is cooled to about 1,000K when the distance reaches roughly 10 times of the radius of the photosphere. Heavy elements in the interstellar gas are then condensed to become interstellar dust. If the central star is oxygen-rich, the dominant component of the dust is silicate. If carbon-rich, the dominant components are graphite (C) and silicon carbide (SiC). In Fig. 1-1-1, life cycle of interstellar dust is illustrated. Dust formed in the above manner can pass through molecular clouds to proto-planetary nebulae. Thus the end of the central star is the beginning of the dust life cycle. Although the dust is only ~1% of the mass of the interstellar material, it plays the following two important roles in the life cycle: (1) dust as the raw material of proto-planetary system, and (2) dust grain surface chemistry.

Role 1: Dust as raw material of proto-planetary system

It is believed that molecular clouds are formed by gravitational contraction of interstellar material. Typical molecular cloud has a mean density of n_H~10^3H/cm^3, a mass of 10^3~10^6M$_\odot$, and a size of 1~10pc. The cloud is not uniform but has a complex structure, sometimes called filament and clump. High density (~10^5H/cm^3) condensations are also recognized by recent high resolution millimeter observations, called the molecular cloud cores. Young stars with an age of ~10^6yr are associated with a disk-like structure of gas and dust that is formed when stars form. This is also considered to be the site of planetary formation, therefore, called a proto-planetary disk. Details of the formation mechanisms of planet is still controversial. According to the Kyoto model (Hayashi 1977, Nakagawa et al. 1981), the dust in the proto-planetary disk is accreted onto the equatorial plane of the disk and a solid layer is formed. Due to the gravitational instability of the dust layer, the layer will eventually collapse and many planetesimals are made. Therefore, the dust is the raw material of the proto-planetary disk.

Role 2. - Dust as the catalyzer of chemical evolution

In molecular clouds, dust and gas have temperature of 10~20K, and gas particles, atoms, ions and molecules, have a mean velocity of a few x 0.1 km /s. Under these conditions, the particles on the grain surface are absorbed on the grain surface at probability of nearly unity when they collide with the dust. As some of the accreted species will be mobile on the grain surface, the probability of meeting with other particles becomes higher than that in the gas phase. As a result, molecules like H_2, H_2O, and NH_3 are more easily formed. Since molecules accrete on the dust core as solid state, they are called "ice".

Not only accretion but also destruction processes, desorption and dissociation occur on the dust surface. Desorption is to cut molecule-to-molecule bonding, while dissociation is to cut atom-to-atom bonding. In such reactions, interstellar UV field, cosmic ray, and dust-to-dust collision play important roles. Interstellar UV field and cosmic ray can cut the atom-atom bonding in the molecules. Alternatively, the temperature of the ice mantle and dust is raised by collision of the dust particles and/or this radiation. Then some molecules are destroyed to become radicals or to be ejected into gas. In addition, when the radicals formed by the disruption meet others, new organic materials, HCHO, CH_3OH, etc., are formed. As shown in Fig. 1-1-1, formation and desorption of ice mantles and organic materials are repeated on grain surface in molecular clouds. A model of the dust formed in this way is shown in Fig. 1-1-2.

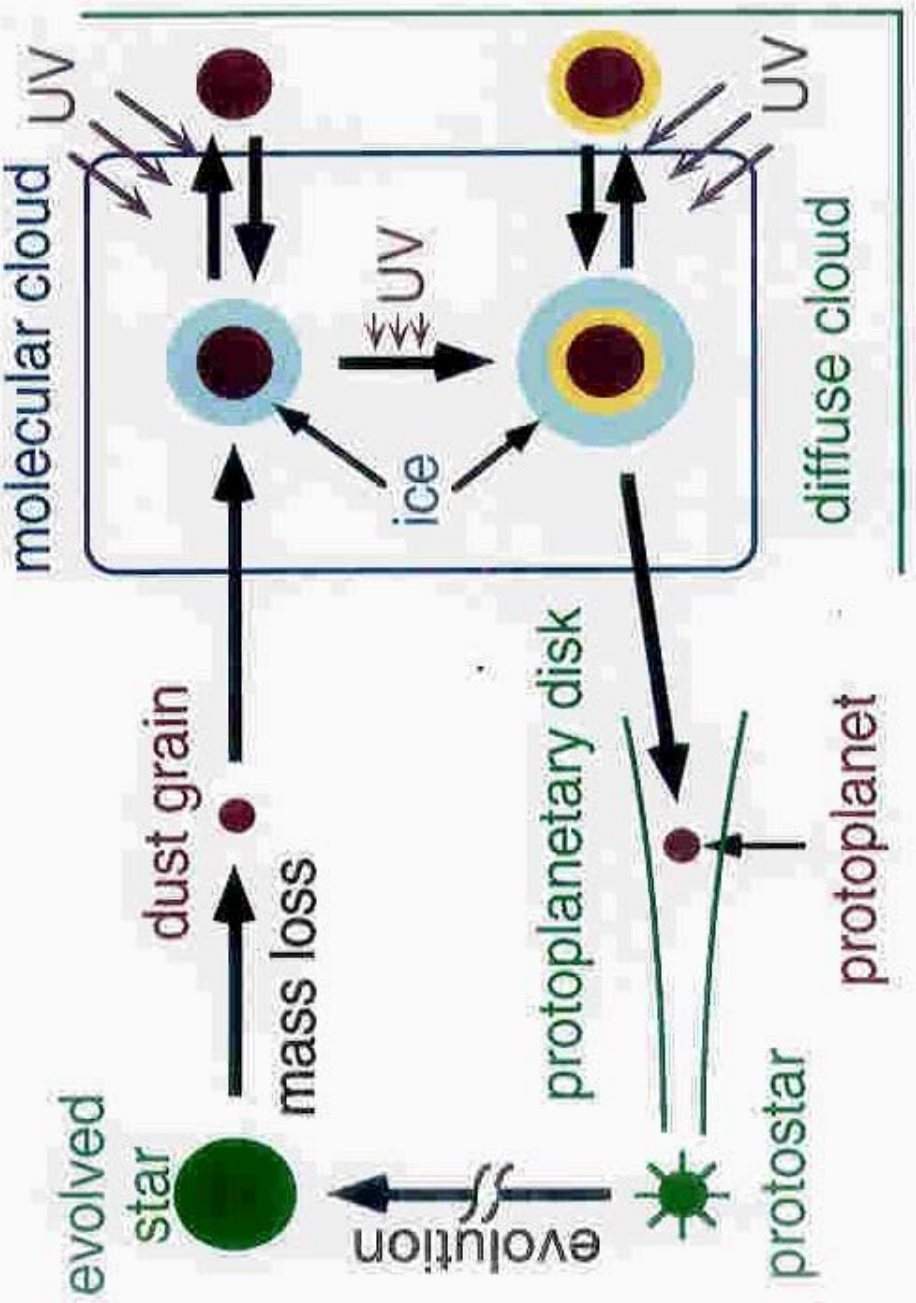

Fig. 1-1-1. The life cycle of the dust in the molecular cloud

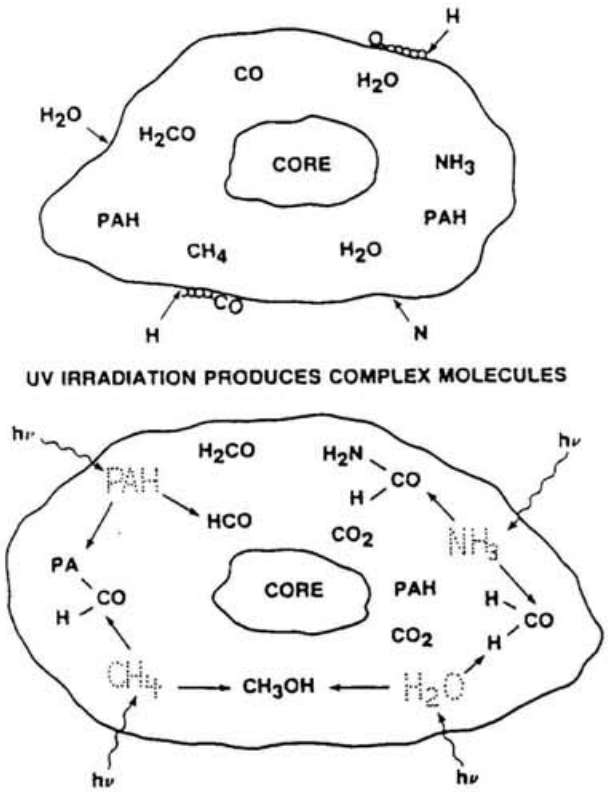

Fig. 1-1-2. Core-mantle model of the interstellar dust (Allamandola, L. J., & Sandford, S. A., 1988)

1-2. Reviews on interstellar ice grains

As descried in the previous section, the interstellar dust itself is the raw material of proto-planetary systems and works as catalysis of chemical reaction. Molecules mainly form on the dust grain surface, called "ice" because its phase is solid. The ice is strongly influenced by the environments dominating the dust. Thus the information of the density, temperature, intensity of interstellar UV field, chemical component, and growth of the ice mantle is obtained by using ice as a probe.

Since molecules in ice mantle have characteristic absorption features in infrared, shown in Table 1-2-1, infrared observation is one of the most suitable methods in the study of the dust. Table 1-2-2 shows the ratio of optical depth of several ices relative to that of water ice (Whittet 1990). Absorption depth of water ice is the deepest among interstellar ices. Furthermore, the abundance of each molecule has been estimated by theoretical research, predicting that water ice occupies 50~70% in the ice mantles. Thus water ice is the most excellent probe of the dust in the cloud.

1-2-1. Water ice in molecular clouds

It was predicted that water ice is one of the abundant components of the ice (van de Hulst 1943, 1949). Water ice was first detected by the 2.5 to 13.5 μm spectroscopy of the Orion BN object (Gillett & Forrest 1973). The obtained spectrum is shown in Fig. 1-2-1. The deep absorption can be seen around 3.1μm. This feature was identified as an O-H stretching mode of the water molecule.

Table 1-2-1*. Molecular vibrational mode.

Molecules	Mode	λ(μm)
H_2O	O-H stretch	3.05
	H-O-H bend	3.0
NH_3	N-H stretch	2.96
CH_4	C-H stretch	3.32
	C-H deformation	7.69
CO	C-O stretch	4.67
CO_2	C-O stretch	4.27
	O-C-O bend	15.3
CH_3OH	O-H stretch	3.08
	C-H stretch	3.35
Silicate	Si-O stretch	9.7
	O-Si-O bend	19.0
SiC	Si-C stretch	11.2

*: Whittet (1992) and see also Allamandola & Sandford (1988).

Table 1-2-2*. Molecular absorption features

λ(μm)	Identification	$\tau_\lambda/\tau_{3.0}$	References
2.85	?	0.2-0.5	1
3.05	H_2O	1.0	1, 2, 3
3.2-3.6	Hydrocarbons?	0.15-0.35	1, 2
4.62	'XCN'	0.0-0.2	4, 5
4.67	CO	0.0-0.2	4, 5, 6
6.0	H_2O	0.20	2, 7
6.85	Hydrocarbons?	0.20	2, 7
9.7	Silicate	0.4-5.0	2, 3
18.5	Silicate	?	8

* : Whittet 1992.

1, Smith et al. 1989. 2, Willner et al. 1982. 3, Whittet 1988. 4, Lacy et al. 1984. 5, Larson et al. 1985. 6, Geballe 1986. 7, Tielens et al. 1984. 8, Aitken et al. 1989.

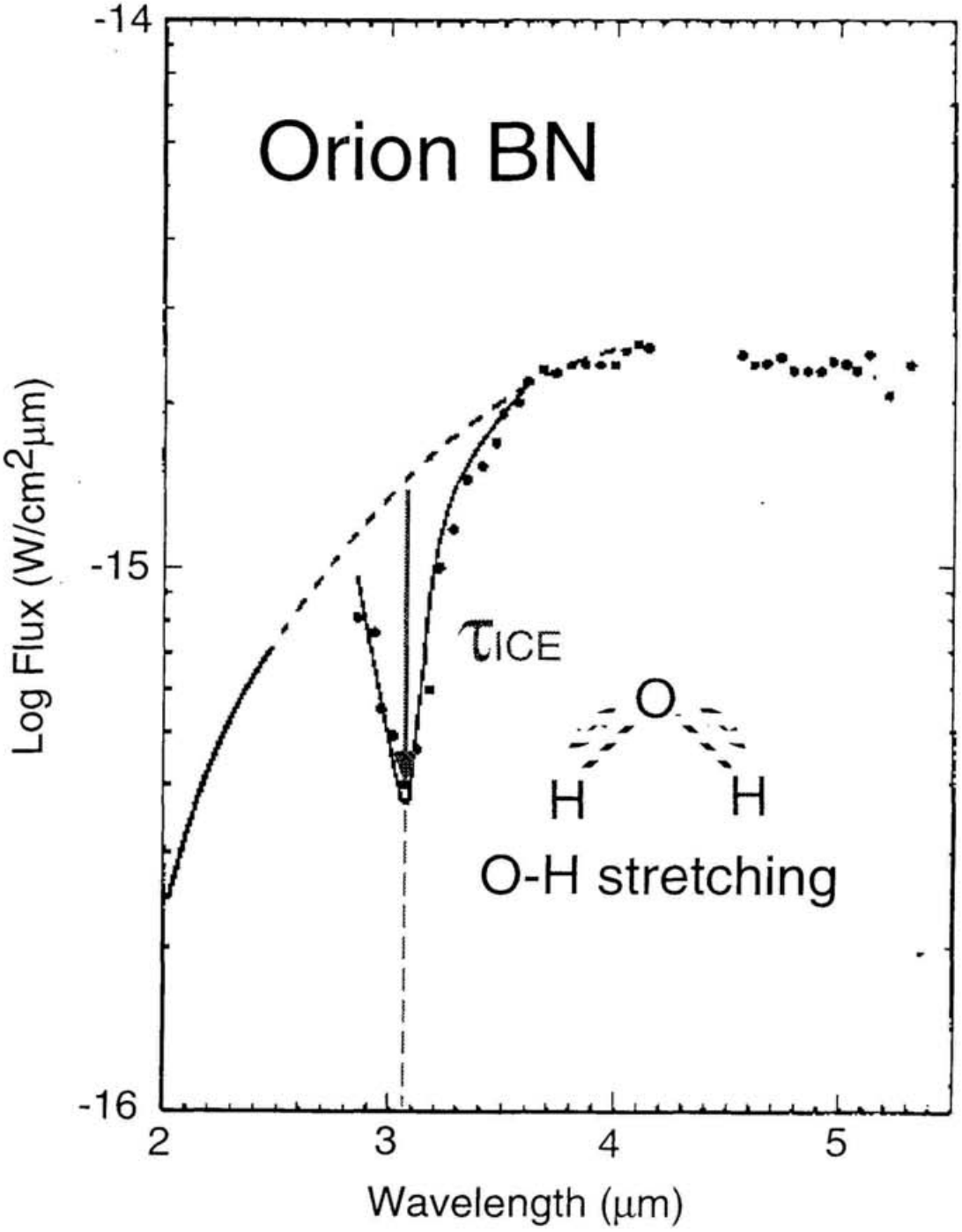

Fig. 1-2-1. 3μm absorption band of the Orion BN (Gillett & Forrest 1973). Dots are observed and solid curve is theoretical calculation.

1-2-1-1. Formation and destruction of water ice

Water ice is formed mainly on grain surface by the reaction,

$$O(G) + H(G) \rightarrow OH(G), \qquad (1\text{-}1\text{-}a)$$

$$OH(G) + H(G) \rightarrow H_2O(G), \qquad (1\text{-}1\text{-}b)$$

where X(G) means that element X is on the grain surface. Namely, water ice is formed by accretion of both hydrogen and oxygen atoms onto the grain surface and by combination of these atoms. Although the reaction rate is not clear because it depends on the structure of grain surface, an upper limit is given by the accretion rate of oxygen atom onto the grain surface,

$$R_{ac} = S_O \sigma_g n_g n_O v_O. \qquad [cm^{-3}\,s^{-1}] \qquad (1\text{-}2)$$

Where σ_g is the mean cross section of grain particle, n_g is number density of grain, n_O is number density of oxygen atom, v_O is mean kinetic velocity of oxygen atom, and S_O is sticking probability when an atom collides on the grain surface. S_O is nearly unity under the condition of the dust temperature of 10~20K. Owing to the lack of knowledge on the precise reaction mechanisms, it is usually assumed that the reaction rate is similar to the accretion rate.

Ice mantle destruction is important since the accretion time scale of $\sim 10^5$ yr for heavy molecules in dense clouds is much shorter than the cloud age of a few x 10^6 yr. Some destruction mechanisms have been proposed and considered, and are shown in Table 1-2-3. In outer cloud, photodesorption mechanism is especially important. The photodesorption rate is expressed by,

$$R_{pd} = Y G_0 \exp(-1.84 A_V) \sigma_g n_g \qquad [cm^{-3}\,s^{-1}] \qquad (1\text{-}3)$$

where Y is photodesorption yield, which is the probability photodesorption occurs and G_0 is the intensity of interstellar UV field. The UV field is shielded in the inner part of the cloud and completely destroys ice mantle in the outer part of cloud. For water ice mantle, the following reactions, although not all, are introduced,

$$H_2O(G) \rightarrow H_2O(gas), \qquad (1\text{-}4\text{-}a)$$

$$H_2O(gas) \xrightarrow{UV} OH(gas) + H(gas). \qquad (1\text{-}4\text{-}b)$$

It is believed that these destruction mechanisms lead to the abundance of H_2O in gas phase.

Previous theoretical studies have attempted to estimate abundance of several molecules formed on grain surface and in gas phase by solving chemical reaction network for principal elements in molecular cloud

(Tielens & Hagen 1982, d'Hendecourt et al. 1985, Breukers 1991). Evolution of molecular abundance in both gas phase and ice mantle was calculated by d'Hendecourt et al. (1985) and the results are shown in Fig. 1-2-2. Cloud density is the constant of $n_H=2x10^4$ cm^{-3}, the temperature of 10K, 551 gas phase chemical reactions, and grain surface chemistries were assumed. The reactions reach a quasi-equilibrium at a time scale of $10^{5\sim6}$ yr and reach an equilibrium at a time scale of $\sim10^7$ yr. If A_V is small, UV intensity increases and the cloud density decreases, therefore, the time scale of reaching equilibrium becomes short. If A_V is large, the opposite situation occurs.

It is clear that water ice is the dominant component in the ice mantle. The total amount of water ice decreases at a time scale of $\sim10^7$ yr, because H_2O production rate slows down due to the reduction of n_H/n_{H2} ratio.

Table 1-2-3*. Water ice desorption mechanisms

Mechanism	Time scale (yr)	Ref.	Comments
UV photodesorption			thickness=0.05μm, $\sigma=8x10^{-18}$ cm^2
UV:$4x10^3$ photons/cm^2s	~$2x10^8$	1,2,3	inside dense cloud
UV:$8x10^7$ photons/cm^2s	~$5x10^5$	1,2,3	outside dense cloud
Explosive heating	>>10^7	4,5,6	
Cosmic Ray spot heating	>10^8	4,7	
Cosmic Ray induced thermal desorption	>>10^8	10	for 0.25μm grains
Thermal desorption			
T_g=10K	~∞	8,9	
T_g=15K	~∞	8,9	

*: Schutte 1995, 1. Hagen et al. 1979, 2. Flannery et al. 1980, 3. Schutte 1995, 4. d'Hendecourt et al. 1982, 5. Leger, Jura & Omnt 1985, 6. Schutte & Greenberg 1991, 7. Bergin, Langer & Goldsmith 1995, 8, Sandford & Allamandola 1990, 9. Blitz & Shu 1980, 10. Westley, Baragiola and Johnson 1995.

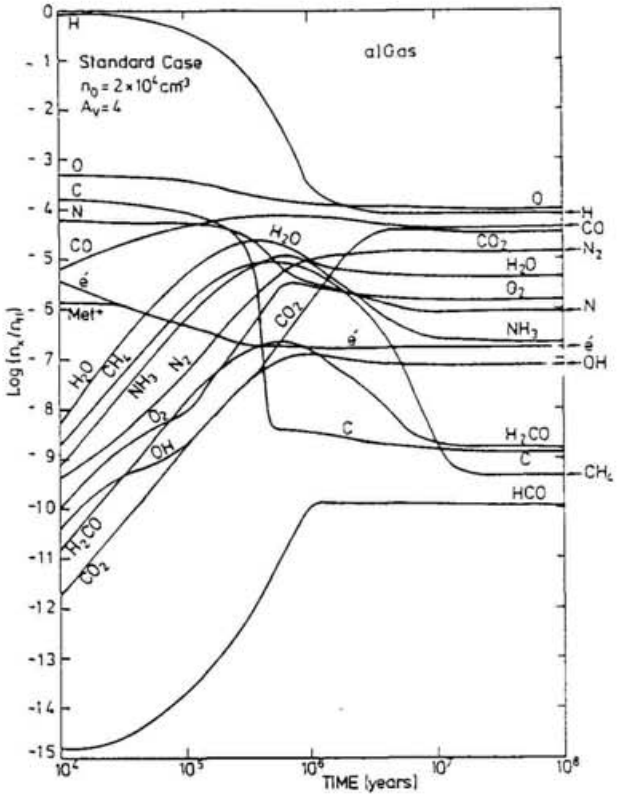

(a) gas phase species

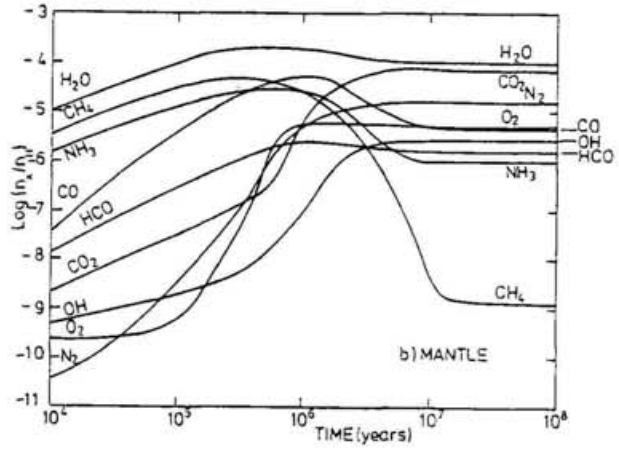

(b) ice mantle

Fig. 1-2-2. Time-dependence of molecular species formed in the molecular cloud. (a) gas phase and (b) ice mantle. For the density of n_H=2x10^4 (cm^{-3}) and A_V=4 mag. (d'Hendecourt et al. 1985)

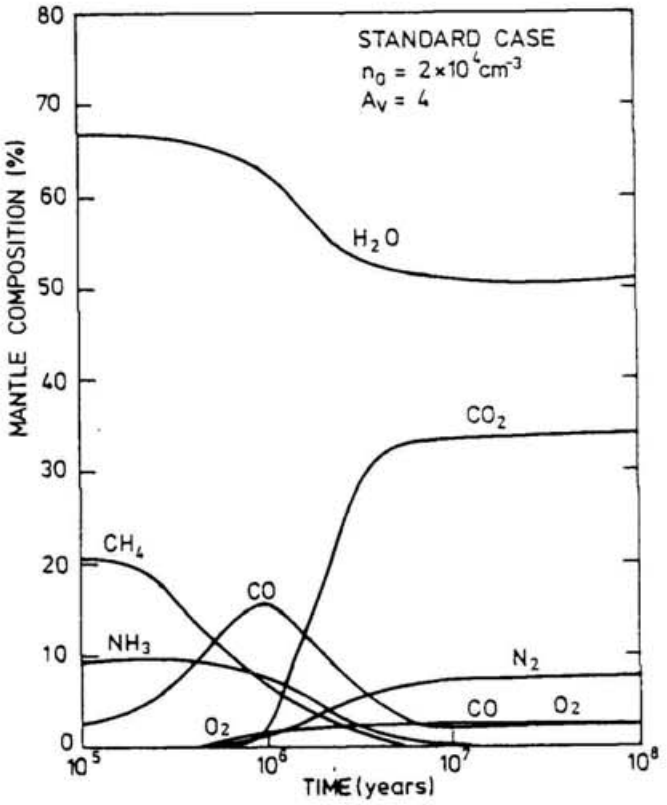

Fig. 1-2-2. Time-dependence of molecular species formed in the molecular cloud. (c) mantle composition. For the density of $n_H=2x10^4$ (cm^{-3}) and $A_V=4$ mag. (d'Hendecourt et al. 1985)

1-2-1-2. Previous observational studies on water ice

Water ice have been detected toward some late type stars, deeply embedded stars and stars shining through molecular cloud. Some of these previous observational studies are reviewed.

1. Late type stars

As described in section 1-1, the dust is actively formed around the late type star in the stage before proto-planetary nebulae. In OH 231.8+4.2, the characteristic absorption feature at 3.1μm shown in Fig. 1-2-3 has been detected. The feature is well fitted by pure water ice model in the laboratory. Thus it is believed that pure water ice forms around late type stars.

2. Young stellar objects (YSOs)

After the first detection of water ice toward the Orion BN object, many researchers have studied deeply embedded young stars. Objects and their absorption depth of water ice are listed in Appendix 1. These observations have revealed the following facts:

(a) High temperature component in the feature

For several young stars, the width of the water ice feature is narrower (van de Buld et al. 1984, Smith et al. 1989). The width is related to the dust temperature: at the temperature T<130K, water ice is formed as amorphous and at 130K<T<150K, as crystal (Hagen, Greenberg & Tielens 1983). In crystal phase, since the molecules is well aligned, the absorption width is narrow. The variation of absorption feature in young stars may be caused when the dust around the disk is heated by the central star. (See Fig. 1-2-4)

(b) Existence of extra molecules

The ice band feature toward YSOs cannot be fitted by a model of pure water ice at ~3.4μm (see Fig. 1-2-5). Therefore it is suggested that ice mantle has extra components such as NH_3 and some organic material with C-H bonding. UV radiation from the central star would change the ice mantle in the disk. This is consistent with the existence of high temperature component in YSOs because such a component may be caused by UV radiation.

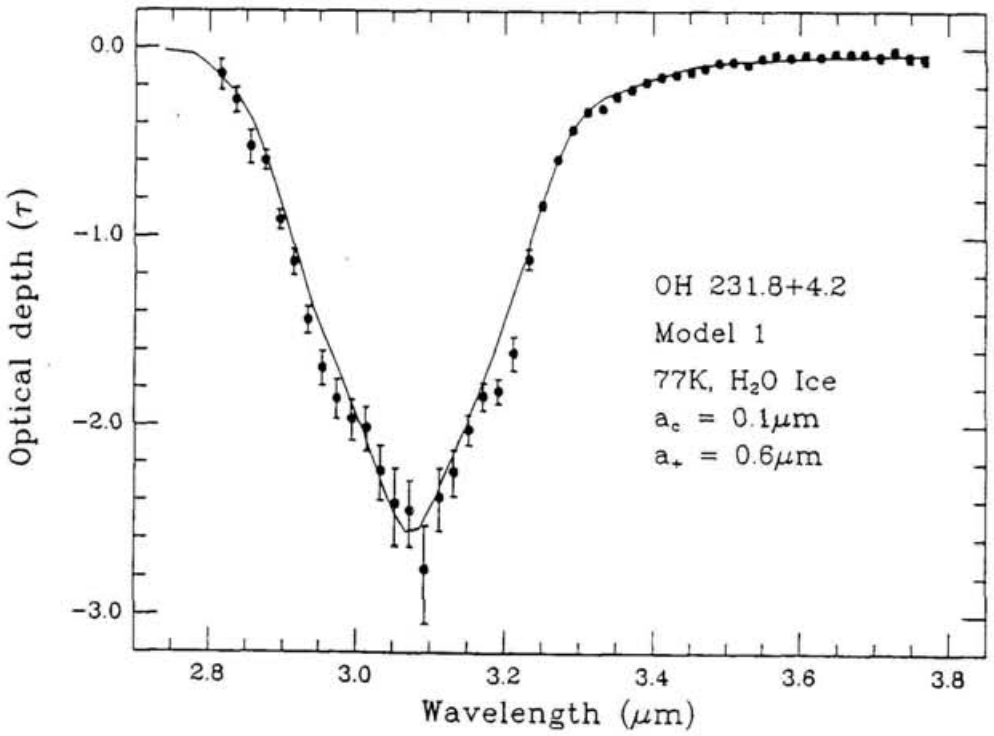

Fig. 1-2-3. The 3μm absorption feature for a late type star of OH 231.8+4.2. Good fitting is obtained with pure water ice made in the laboratory. (Smith et al. 1988)

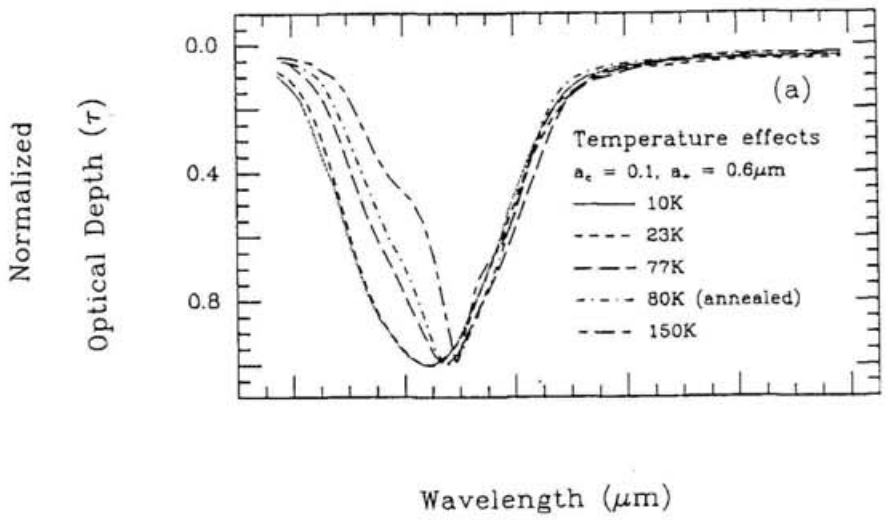

Fig. 1-2-4. Temperature-dependence of width of absorption feature of water ice. At a higher temperature shows a narrower absorption band width. (Smith et al. 1989)

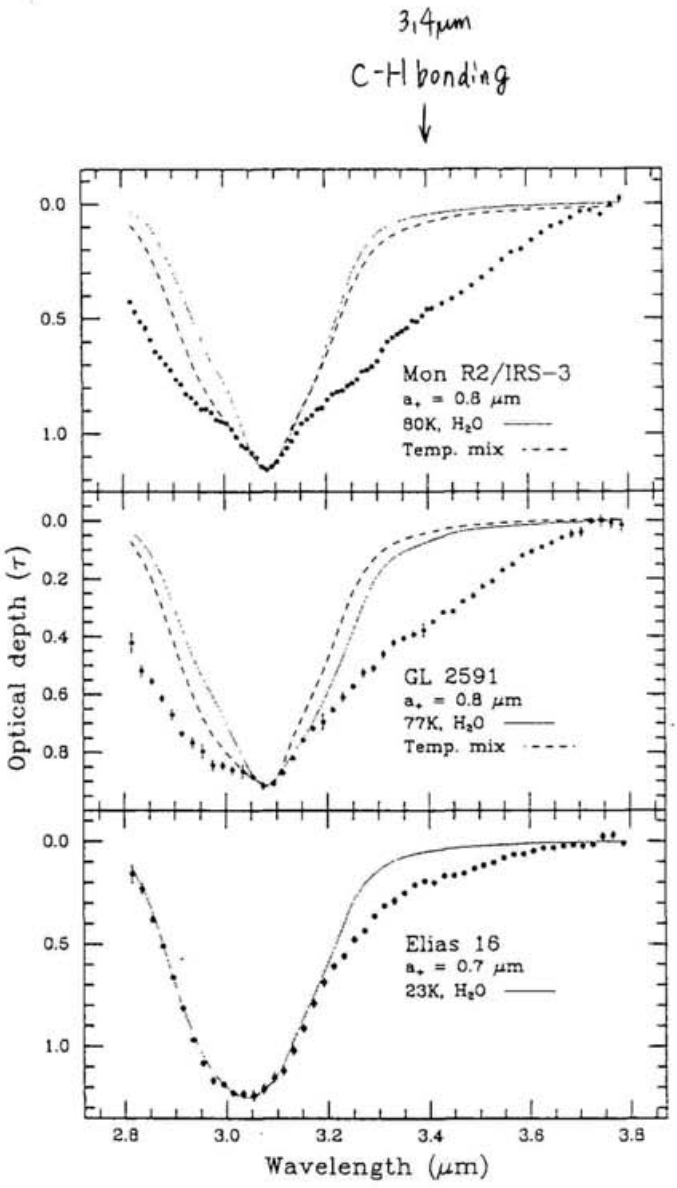

Fig. 1-2-5. Long wavelength wing at 3.4μm, probably due to extra components of NH_3 and some organic materials with C-H bonding. (Smith et al. 1989)

3. Field stars

There is a critical problem in the observations of YSOs; the absorption feature includes two contributions, of disk and of molecular cloud and it is very difficult to separate them. Therefore observations of field stars, shining through molecular cloud, are important for the study of ices in molecular clouds.

Whittet et al. (1983) discovered water ice in molecular clouds by observing field stars shining through the Taurus cloud. The observation were extended to cover 17 field stars by Whittet et al. (1988). Figure 1-2-6 shows ^{13}CO map of the Taurus molecular cloud (Mizuno et al. 1995, Onishi et al. 1996). Filled circles indicate the positions of observed stars by Whittet et al. Note that only a limited number of sources were observed in this large cloud. Optical depth of water ice was estimated and the relationship of visual extinction A_V and τ_{ICE} were shown in Fig. 1-2-7. This result shows that absorption of water ice is not detected for $A_V<3.3$ mag and τ_{ICE} is proportionally increases with increasing of A_V. This leads to next important results, (1) rough distribution of water ice, (2) influence of UV field on the formation and destruction of water ice, and (3) abundance of water ice.

(1) Rough distribution of water ice

Whittet et al. proposed that water ice exists only inside molecular cloud because the relationship between A_V and τ_{ICE} has a A_V threshold. Furthermore, number of water molecules in the line of sight is proportional to that of dust since τ_{ICE} proportionally increases with increasing A_V.

The result can be regarded as a simple onion-shell structure model of a cloud shown in Fig. 1-2-7. There are two regions without water ice along the line of sight for field stars, while there is only one for YSOs.

(2) Influence of UV field on the formation and destruction of water ice

Whittet et al. additionally proposed that UV field contributes the existence of the A_V threshold. While water ice is destroyed by UV field in outer parts of the cloud, it can survive in inner parts because UV field is sufficiently shielded by the outer dust.

Smith et al. (1993) derived the threshold value of A_V from a theoretical consideration. The A_V threshold is defined as the A_V when accretion rate of oxygen atom is equal to photodesorption rate. Both rates are given by

$$R_{ac} = 3\times10^{-16}\, n_H\, T_g^{1/2}, \qquad [s^{-1}] \qquad (1\text{-}5\text{-}a)$$

$$R_{pd} = 10^{-12} \exp(-1.84 A_V). \quad [s^{-1}] \qquad (1\text{-}5\text{-}b)$$

(see also Drain & Salpeter 1979, Boland & de Jong 1982).

Assuming the density to be $n_H \sim 100 cm^{-3}$ and the gas temperature to be T_g=50K, the A_V threshold becomes,

$$A_{V0} \sim 1 \text{ mag.} \qquad (1\text{-}6)$$

This result is valid for a source inside a molecular cloud. Since there are two regions without water ice on both the front and rear sides along the line of sight, A_{V0} becomes about 2 mag for the background field stars.

(3) Abundance of water ice.

The column density of water ice, N_{ICE} (N/cm^2), in the line of sight can be estimated by the absorption depth of water ice derived from,

$$N_{ICE} = \frac{\Delta\nu}{A} \tau_{ICE} . \qquad (1\text{-}7)$$

Where $\Delta\nu$ (cm^{-1}) is the FWHM of absorption profile of water ice and A is the integrated absorbance (cm/molecule), which are taken to be 360 cm^{-1} and 2.0×10^{-16} cm/molecule, respectively (Allamandola and Sandford 1988).

In addition, the column density of hydrogen N_H (N/cm^2) is derived from A_V by the relationship, $N_H = 1.9 \times 10^{21} A_V$ (Bolin, Savage and Drake 1978). The ratio of N_{ICE} to N_H is given by,

$$\frac{N_{ICE}}{N_H} = \frac{\Delta\nu}{A} \frac{\tau_{ICE}}{A_V} = 9.5 \times 10^{-4} \frac{\tau_{ICE}}{A_V} . \qquad (1\text{-}8)$$

For example, for τ_{ICE} is 1, N_{ICE} is 1.8×10^{18} (N/cm^2) and for $\tau_{ICE}/A_V \sim 0.093$ obtained by Whittet et al., N_{ICE}/N_H is 8.8×10^{-5}. The N_{ICE} is equal to the column density of oxygen atom N_O, since there is one oxygen atom in a water molecule. Thus $N_{ICE}/N_H = N_O/N_H$. The N_O/N_H is about 0.13 times of initial fraction if solar cosmic abundance, $(N_O/N_H)^* = 8.5 \times 10^{-4}$ (Chronological Scientific Tables, 1997), is assumed. Namely about 10% of oxygen atoms is consumed as water ice. Furthermore, if the ratio of $\Delta N/A$ is constant in both dense and thin regions, this suggests that size distribution of grain core and thickness of ice mantle of the dust in dense region are similar to that in diffuse region.

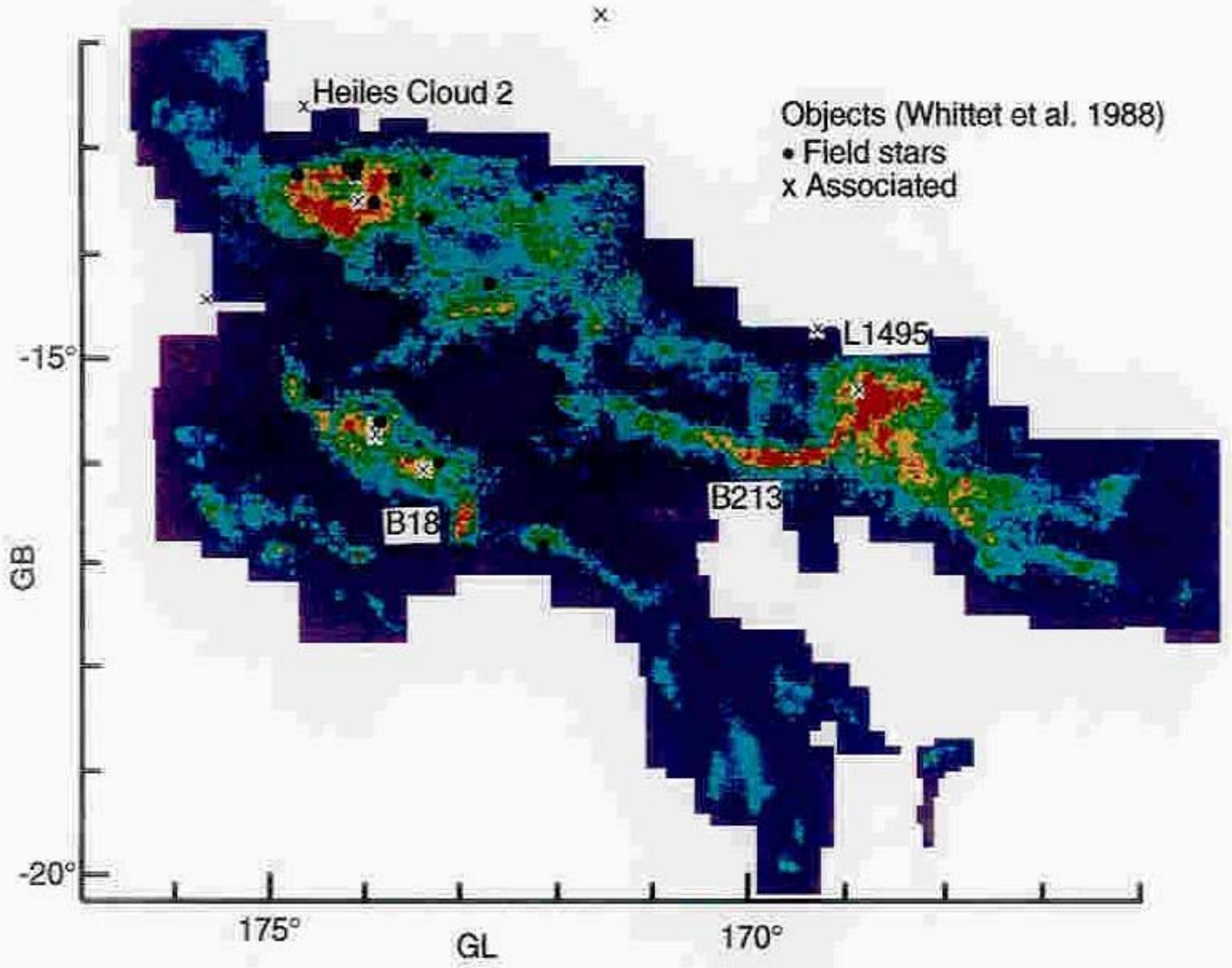

Fig. 1-2-6. ^{13}CO map of the Taurus molecular cloud Nagoya university 4m. 2' beam = 17,000 A.U. (Onishi et al. 1996)

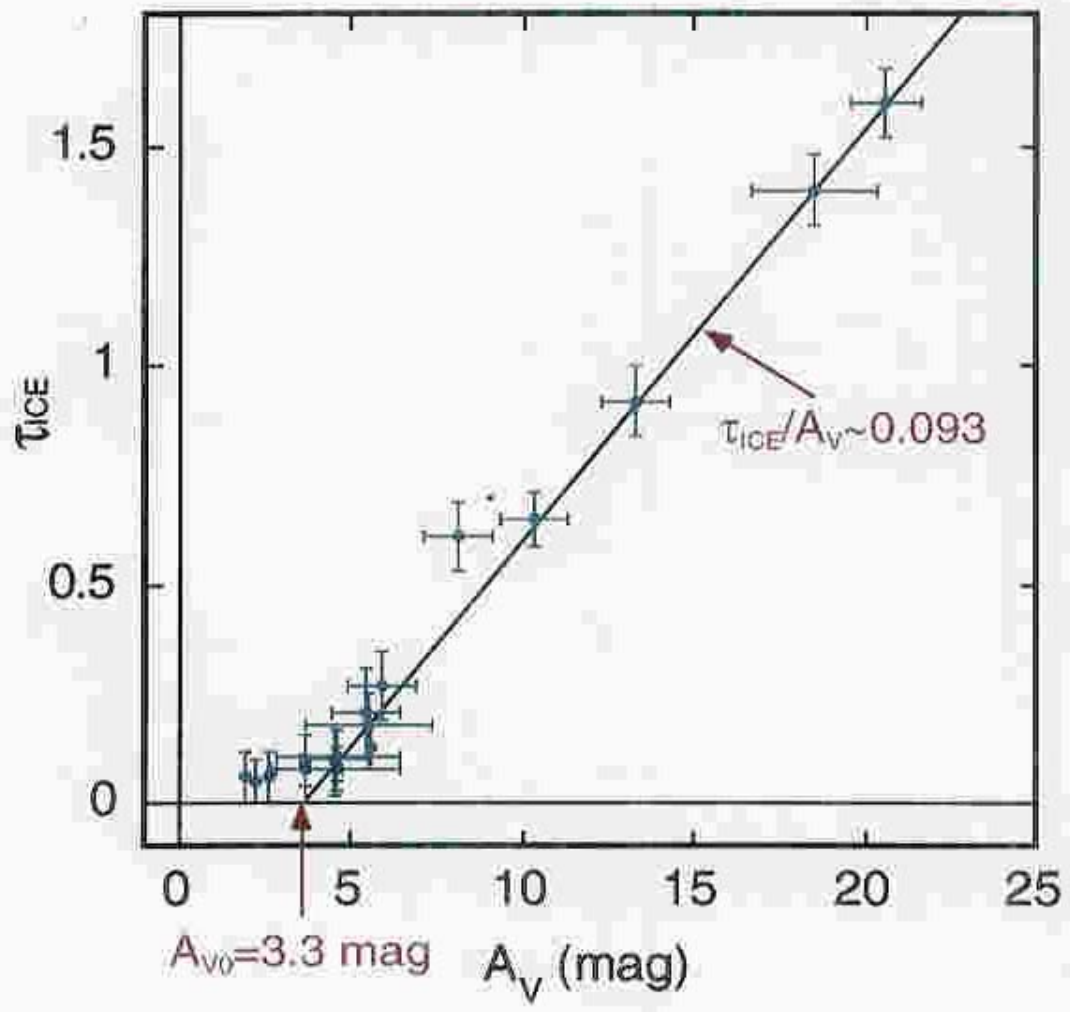

Fig. 1-2-7. A_V vs. τ_{ICE} (by Whittet et al. 1988). Absorption of water ice is not detected for $A_V < 3.3$ mag. The τ_{ICE} proportionally increases with increasing A_V for $A_V > 3.3$ mag.

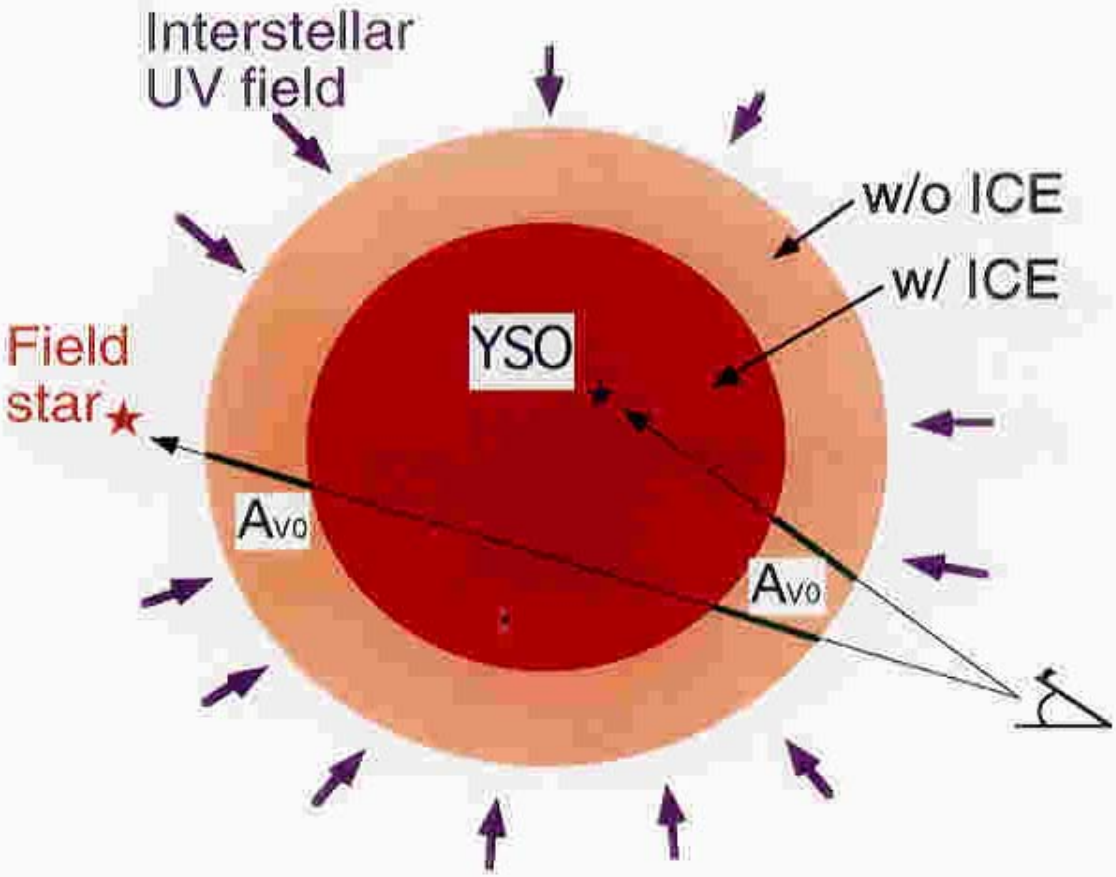

Fig. 1-2-8. Simple onion-shell structure of a molecular cloud. Existence of a A_V threshold in the diagram of A_V vs. τ_{ICE}, suggests that water ice does not exist in outer parts of the cloud. This is due to the photodesorption by interstellar UV field. In inner parts of the cloud, UV field is shielded by the dust in outer parts. Water ice can exist in which the formation rate of water ice become larger than the destruction rate. There are two parts without water ice in the line of sight for field star while there is only one for YSO. Thus A_{V0} of a field star is twice of that of a YSO.

4. Others observational works on water ice

Observations of water ice in molecular clouds have also been conducted for several other clouds. The A_V threshold is summarized in Table 1-2-4 (see also Williams et al. 1992). The value for the Taurus cloud is about 3 mag, the smallest in the molecular clouds, while that for the ρ Oph is more than 10 mag. Such variations of A_{V0} is probably caused by the variation of intensity of interstellar UV field.

As shown in Table 1-2-5 the value, τ_{ICE}/A_V, is generally constant of 0.06~0.1. In addition, τ_{ICE} proportionally increases with increasing A_V without depending on the regions. This means that the abundance of water ice is proportional to that of the dust, and the growth of water ice does not depend on the regions although the intensity of the UV radiation has variations among the regions.

Table. 1-2-5*. Summary of published water ice observations toward molecular cloud.

Clouds	A_{V0} (mag)	τ_{ICE}/A_V	References
Taurus	3.3	0.093±0.001	Whittet et al. 1988
	2.6	0.059±0.003	Smith et al. 1993
ρ Ophiuchi	~ 25	0.094	Harris et al. 1978
	≥ 12.5	-	Whittet & Blades 1980
	10-15	0.06±0.01	Tanaka et al. 1990
Corona Australis	>15	-	Whittet & Blades 1980
	3.4	0.066±0.006	Whittet et al. 1996
	3.3 (10-15)†	0.093 (0.06) †	Tanaka et al. 1994
Serpens	5-10	0.066	Eiroa & Hodapp 1989

*: See also Williams et al. 1992.

†: adopted value by Whittet et al. 1988 for field stars and in bracket by Tanaka et al. 1990 for YSOs.

1-2-2. Extinction by interstellar dust

In previous sections, roles of dust in molecular cloud was described and several previous studies about material formation on the dust surface, distribution of the material and the evolution of the materials were reviewed. In this section, another aspect dust is considered, namely, extinction by dust.

Interstellar dust extinct light incident into it and change its spectrum. The properties of the extinction strongly depends on chemical component, size distribution, shape, temperature and column density of dust. Therefore, such physical and chemical properties of dust can be obtained by investigation of characterization of interstellar extinction.

In addition, it is important to find the characterization of interstellar extinction for recovery of intrinsic spectrum of object observed through the dust.

1-2-2-1. Observational studies

The color excess between two wavelengths ($\lambda 1$ and $\lambda 2$) is defined as

$$E(\lambda 1-\lambda 2)=(\lambda 1-\lambda 2)o-(\lambda 1-\lambda 2)i. \qquad (1\text{-}5)$$

Where $(\lambda 1-\lambda 2)o$ is observed color and $(\lambda 1-\lambda 2)i$ is intrinsic color of a star shining through a cloud. It is usual that the extinction is normalized by the color excess at B and V bands,

$$\left.\frac{E(\lambda-\lambda 1)}{E(\lambda 2-\lambda 1)}\right|_{\lambda 1=V,\lambda 2=B} = \frac{E_{\lambda-V}}{E_{B-V}}. \qquad (1\text{-}6)$$

Extinction curve from UV to infrared for diffuse region is shown in Fig. 1-2-9. The transverse axis means wavenumber (μm^{-1}). The extinction generally increases with increasing the wavenumber. Since the infinite wavelength is considered to give zero absorption, Eq. (1-6) gives,

$$\left.\frac{E_{\lambda-V}}{E_{B-V}}\right|_{\lambda\to\infty} = -\frac{A_V}{E_{B-V}} = -R_V \qquad (1\text{-}7)$$

R_V is called the ratio of total-to-selective extinction. Thus visual extinction, A_V can be estimated by extrapolating to wavenumber to zero and using R_V.

The R_V is 3.1 for standard diffuse interstellar medium (Savage and Mathis 1979). Martin and Whittet (1990) summarized the results of interstellar extinction for several regions. These results as well as those

obtained by several other groups are listed in the Table 1-2-6. R_V has a range of values depending on the regions, 3.5 for the Taurus dark cloud (Straizys et al. 1982, Straizys et al. 1985) and 4.2 for the ρ Oph cloud. The variations of R_V is due to different size distributions of dust; R_V increases when the dust size increases. In the Taurus dark cloud the grain size is larger than that in the diffuse regions because the grains are covered with ice mantles (Straizys et al. 1985).

The observations also suggest that the extinction curve can be approximated by an exponential function,

$$\frac{E_{\lambda-V}}{E_{B-V}} = e\lambda^{-\alpha} - R_V, \text{ or } A_\lambda = \beta\lambda^{-\alpha}. \qquad (1\text{-}8, 9)$$

in the wavelength range from visible to infrared. Martin and Whittet (1990) conclud that the index α has a common value of ~1.84 between I (0.8 μm) and M (5.0μm) bands for the ρ Oph and the diffuse regions. This corresponds to the slope of 1.60 on the JHK color-color diagram. However, the index α is about unity at visible wavelengths and is about 1.8 at infrared wavelengths. This might suggest that an change of the index occurs at near J band.

Table 1-2-6. Extinction law

Sample	Range	α	R_V	references
Diffuse region				
	M to I	1.84±0.03	3.05±0.01	1
		1.64	~3.1	2
	4.5 to 1.5	1.85±0.05	-	3
	N to U	1.51	3.04	4
Dense clouds				
ρ Oph cloud	M to I	1.85±0.09	4.26±0.04	1
Taurus dark cloud	N to V	-	3.5	5
Herchel 36		-	5.3	6
Galactic center				
Tr 14/16	K to J	1.87	4.17	1
	N to J	-	3.09±0.03	7

1. Martin & Whittet 1990. 2. Savage & Mathis 1979. 3. Landini et al. 1984. 4. van de Hulst 1949. 5. Straizys et al. 1985. 6. Mathis 1990. 7. Rieke et al. 1985.

1-2-2-2. Theoretical studies

The extinction by interstellar dust was modeled by van de Hulst (1949) based on the Mie's scattering theory (Mie 1909). Extinction A_λ can be expressed with extinction coefficient Q_{ext},

$$A_\lambda = -2.5\log_{10} e \int_{a\,min}^{a\,max} \pi a^2 Q_{ext}(a,\lambda) n(a) da \qquad (1\text{-}10)$$

Where a is radius of the particle, n(a)da is the column density per unit dust size and $\pi a^2 Q_{ext}$ is the extinction cross section, C_{ext}. The Q_{ext}, in addition, can be separated by absorption term, Q_{abs}, and scattering term, Q_{sca}:

$$Q_{ext}=Q_{abs}+Q_{sca}. \qquad (1\text{-}11)$$

Fig. 1-2-10 shows the result of calculation of Q_{ext}, Q_{abs} and Q_{sca} for one spherical particle with a complex refractive index of m=1.60-0.05xi, which is mean refractive index of the interstellar dust (Whittet 1992). The transverse axis in Fig. 1-2-10 is the size parameter defined as,

$$q=2\pi a/\lambda. \qquad (1\text{-}12)$$

If $q<<1$, Q_{abs} and Q_{sca} are approximated by,

$$Q_{abs} \approx 4q\Im\left(\frac{m^2-1}{m^2+2}\right), \text{ and}$$
$$Q_{sca} \approx \frac{8}{3}q^4\left|\frac{m^2-1}{m^2+2}\right|^2, \qquad (1\text{-}13)$$

respectively.

The Rayleigh scattering corresponds to this $Q_{sca}(\propto\lambda^{-4})$. If the particle has absorption, $Q_{abs}(\propto\lambda^{-1})$ is more dominant than Q_{sca} for $q<<1$. If $q>>1$, Q_{ext} is close to the constant value 2, which means the extinction cross section is the twice of the geometrical cross section of the particle. In most cases of the extinction in the interstellar cloud, the range of $0<q<2\pi$ is of interest because the radius of the particle is ~0.5μm. The wavelength dependence of the Q_{ext} is about $q\sim q^4$, thus, the wavelength dependence of A_λ is predicted $A_\lambda\propto\lambda^{-1}\sim\lambda^{-4}$.

Many attempts to determine the chemical components and size distributions of the interstellar dust have been conducted. Savage et al. (1975) claimed that 220nm bump is caused by graphite. Mathis, Rumple & Nordsieck (1977) modeled the size distribution of the dust based on the observational results by Code et al. (1976) and Nandy et al. (1975) and in addition, estimated the chemical component of graphite and olivine. According to this model the number of the dust particle with a radius of a is proportional to $a^{-3.5}$ and the lower and upper limits of the size are $0.005<a<0.25$ μm. Their size distribution is often used as a standard dust

model (the classical MRN model). Note, however, Draine & Lee (1984) estimated that the chemical component of the interstellar dust is $10^{-25.16}$:$10^{-25.11}$ of graphite versus silicate. Therefore, a modified MRN model which has taken this into account is used in these days. Fig. 1-2-11 shows a result of calculation of A_λ with the modified MRN model. This result clearly shows that index of A_λ power law changes near J band, and the index is about 1.3 between B and I bands, and is about 1.8 between I and M.

In addition, interstellar extinction for dust with ice mantle have been considered (Drain & Lee 1984). Smith et al. (1993) estimated morphology of ice mantle for field stars in the Taurus dark cloud by calculation of Mie scattering theory with ice-coated sphere. The extinction coefficient is expressed in eq(A2-1, A2-8 & A2-9) in Appendix 2. In the literature, one of possible distributions of ice mantle thickness is that there are two populations, one has ice mantle with constant thickness of 0.35μm and another one is bear grain and the ratio of two population is $1:3\times10^4$. In Fig. 1-2-12, extinction A_λ for such dust is compared with that for bear dust without mantles. Water ice absorption feature clearly appears at near 3.1μm. For other wavelength range, power index of A_λ rarely changes and extinction slightly increases.

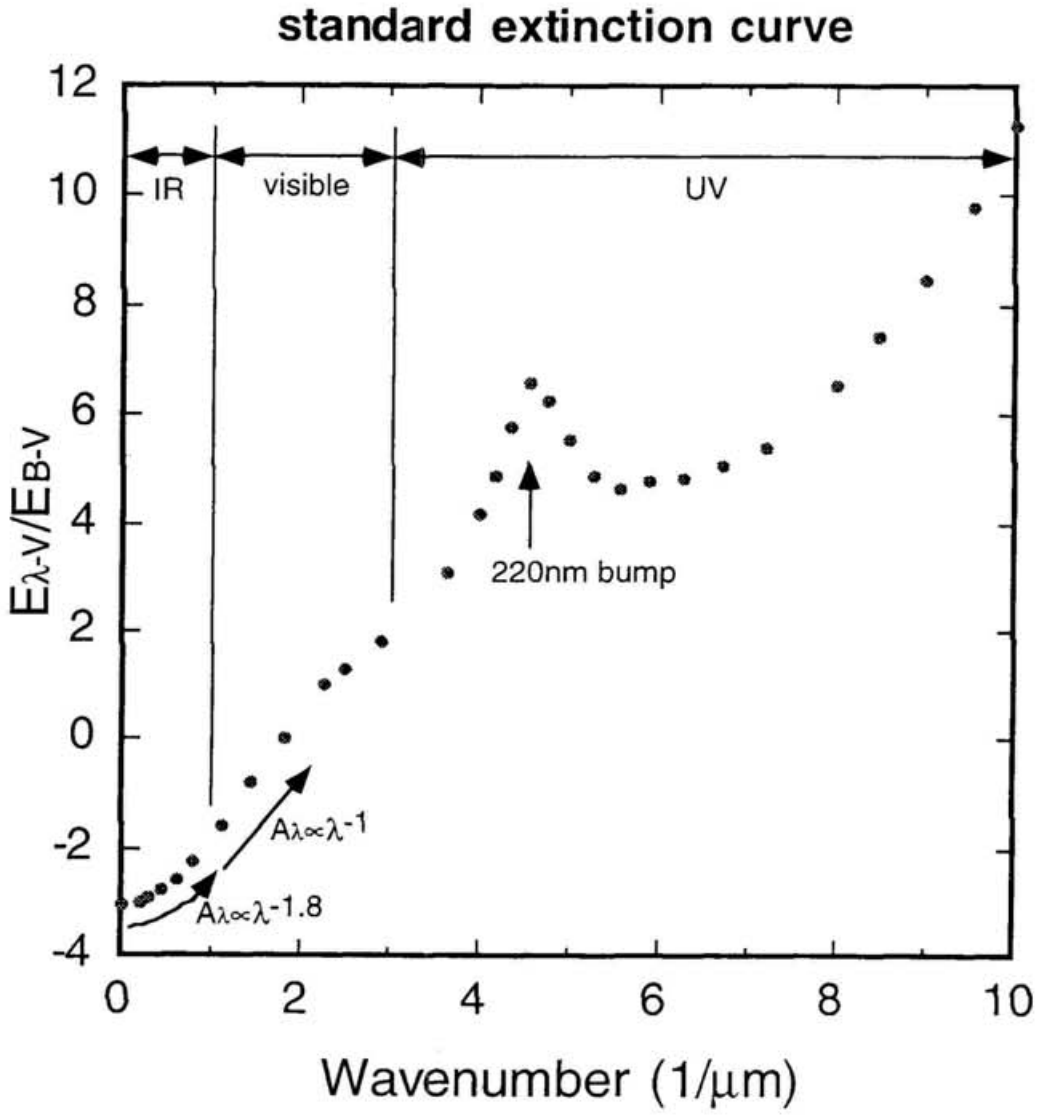

Fig. 1-2-9. Extinction curve for the standard diffuse cloud. (Whittet et al. 1992). The $A_\lambda \propto \lambda^{-1.8}$ at near infrared and $\propto \lambda^{-1.0}$ at visible wavelength. The R_v is about 3.1. There is a bump at 220nm of carbonaceous material.

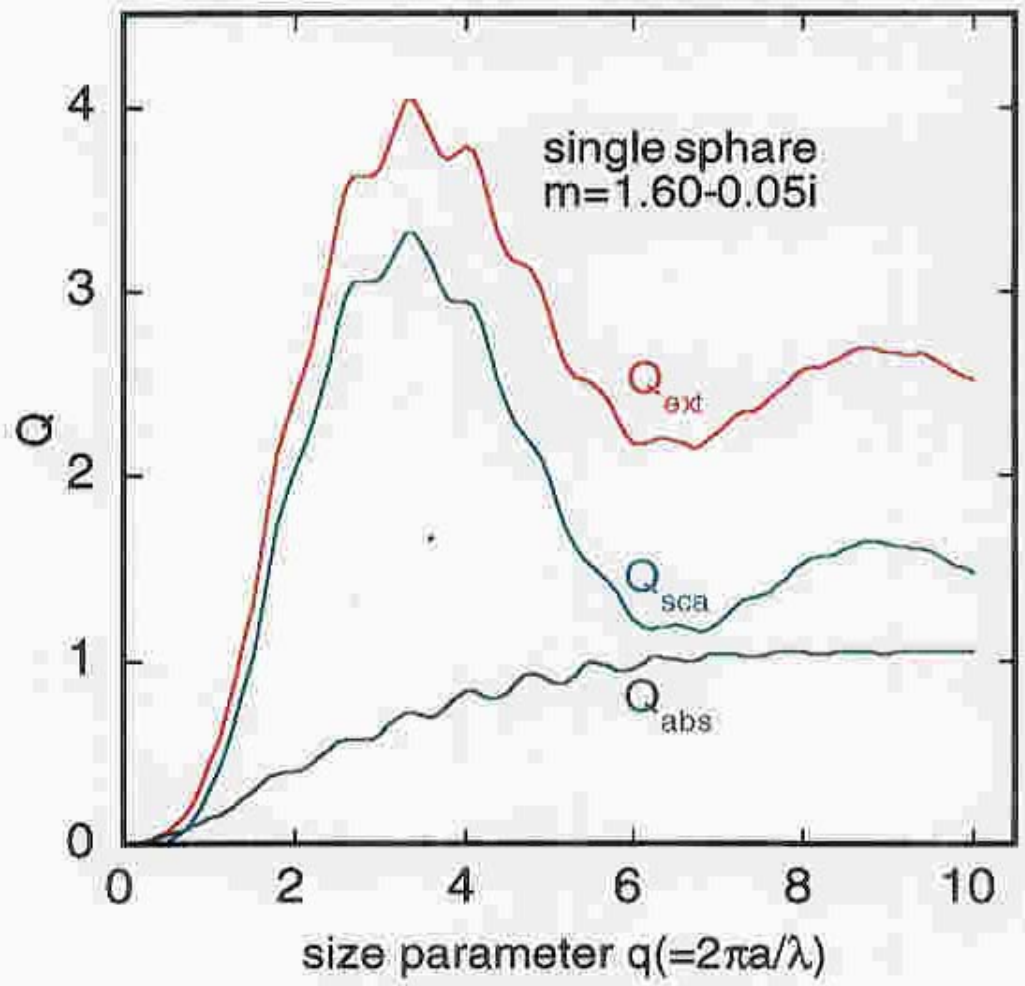

Fig. 1-2-10. Extinction coefficient for a single sphere. The refractive index is m=1.60-0.05i, which is mean value for interstellar dust. $Q_{ext} = Q_{sca} + Q_{abs}$. For $q<<1$, $Q_{sca} \propto \lambda^{-4}$, corresponds to Rayleigh scattering, $Q_{abs} \propto \lambda^{-1}$. For $q>>1$ Q_{ext} comes constant.

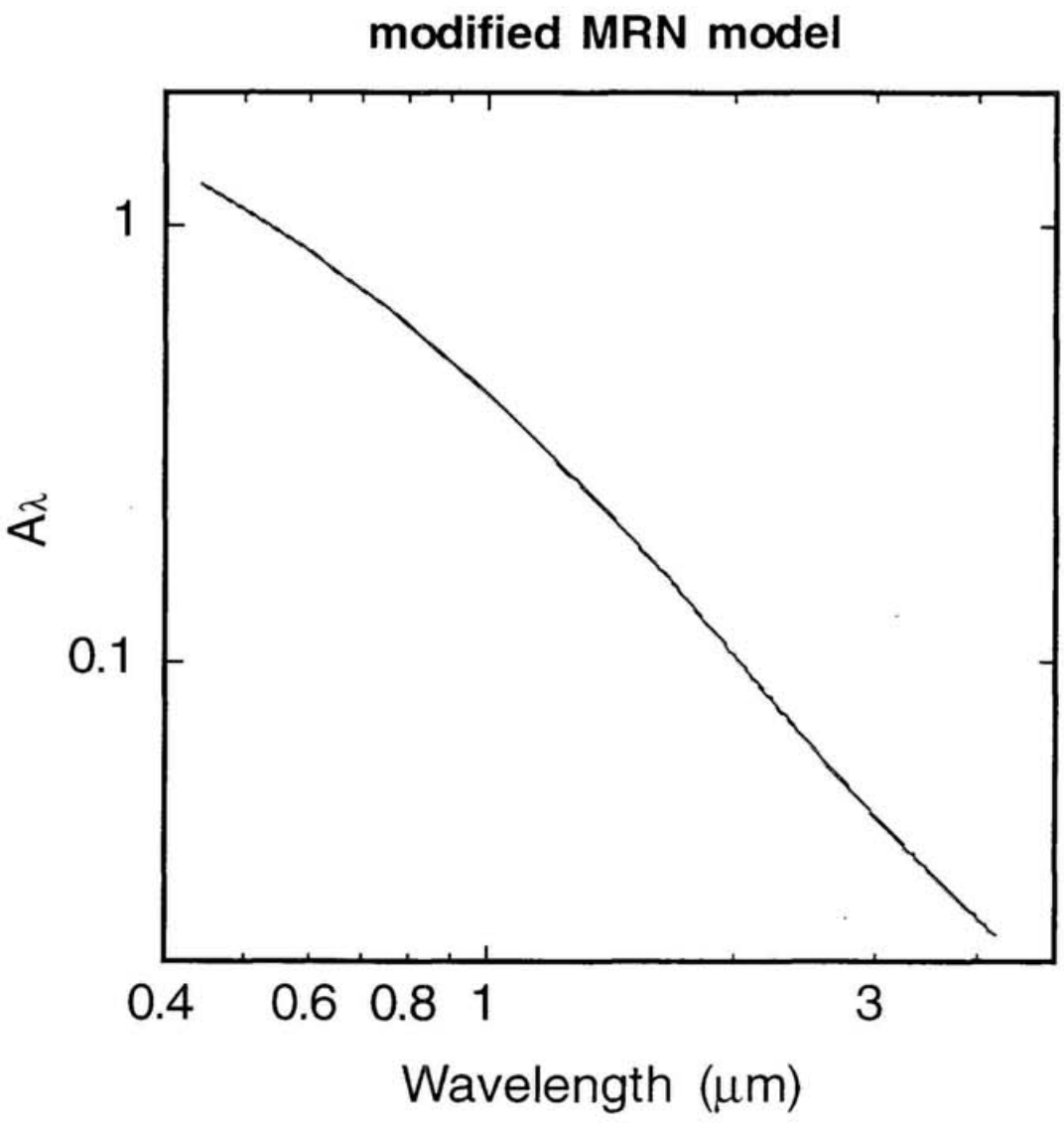

Fig. 1-2-11. Extinction curve of modified MRN model. The shape and size distribution are same as MRN model, however chemical component is different. For the modified model by Draine & Lee (1984), silicate is used instead of olivine. The refractive indices of graphite and silicate are given in Draine (1985). The A_λ can be approximated by power function for J to M. The power index is about 1.8 at J to M.

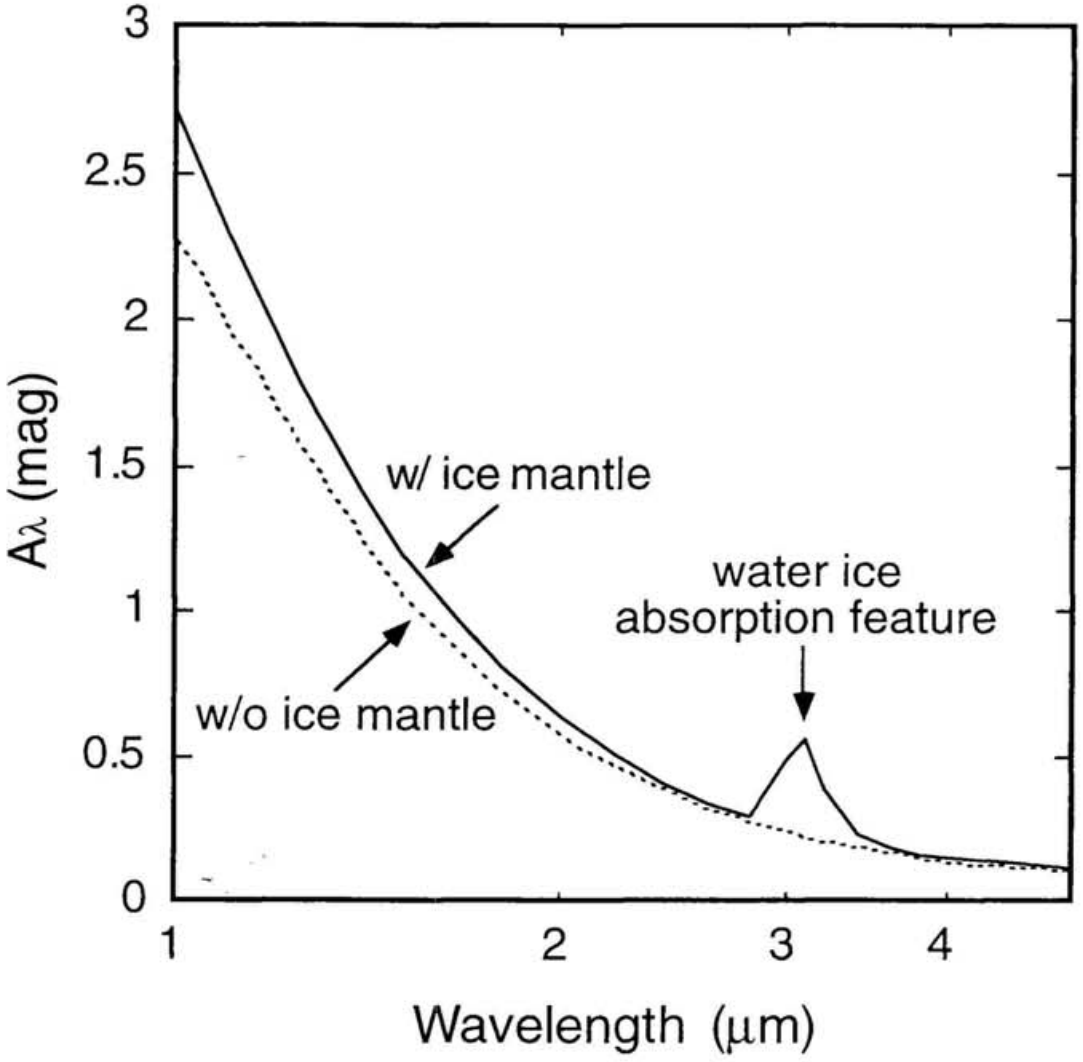

Fig. 1-2-12. Extinction curve for dust with ice mantle. The model of dust is used as a field star in the Taurus dark cloud, Elias 13 (A_V=12 mag, τ_{ICE}=0.54) (Smith et al. 1993). In this model, two population of dust grain are considered, one is bear grain and another one is ice-coated grain, and the ratio of components is $1:3x10^4$.

1-3. Motivation and aim of this thesis

As described in the last section, the existence of water ice in a molecular cloud was demonstrated by Whittet et al. (1983, 1988), who showed that ice mantle is evaporated or disorbed in the outer part of the Taurus molecular cloud and can survive in the inner cloud. However, detailed distributions of water ice in a molecular cloud have never been revealed so far. Recently, high resolution maps of the Taurus molecular cloud have been obtained by radio observations (Schloerb et al. 1984, Onish et al. 1995, Mizuno et al. 1996, Sunada and Kitamura 1997). As shown in the ^{13}CO map in Fig. 1-2-4, the actual molecular cloud has some complex structures such as filaments and clumps. Therefore it is interesting to ask what is the relationship between the region of the filametary and clumpy structures and the region where water ice exists. When we study the water ice mantles (τ_{ICE}) of a large number of field stars with ranging from low to high visual extinction (A_V), concentrating on only one cloud, can we see the good linear relationship between A_V and τ_{ICE}? What is the relationship between the CO distribution obtained by radio observations and that of water ice? The details of the observations for answering these questions will be described in section 2-1.

In order to derive the water ice distribution in a cloud, it is necessary to observe a number of sources toward a cloud. However this has been very difficult with the conventional instruments which employed a single detector with CVF (a circular variable filter). With the instrument having such a narrow wavelength coverage, it was difficult to cancel the temporal variations of the condition of sky. To solve this problem, Kobayashi et al. (1996) developed a spectrometer called PASP2 (Prism Array Spectro-photo Polarimeter 2). Although this instrument, with a 32 ch InSb detector, has a relatively low-resolving power of wavelength ($\lambda/\Delta\lambda$~40), it can simultaneously acquire a wide wavelength coverage from 1.26 to 4.20μm. Thus an accurate spectrum can be obtained in a short integration time. As a result, we have been able to obtain the spectrum of 62 sources.

Besides the spectral features, the continuum spectra of the background stars shining through clouds will provide us valuable information of the interstellar extinction, i.e., the reddening law in the molecular cloud. The comparison of the reddening law in the dense cloud with that in the diffuse interstellar medium is very intriguing. Since we have observed as many as

62 field stars, compared with only 5 stars previously studied, we hope that we can improve the statistical accuracy for the discussion. Therefore, we will discuss the reddening law in the dense cloud at near-infrared wavelength in section 3-2.

2. 1.3~4.2μm spectroscopy of dust in the Taurus dark cloud

2-1. Observations

2-1-1. Region and objects

We have studied Heiles Cloud 2, a part of the Taurus molecular cloud complex whose map in the $C^{18}O$ line is shown in Fig. 2-1-1. The distance is about 140 pc (Elias 1978), and the size of this cloud is about 3 pc. The total mass of the cloud is estimated to be $330M_{\odot}$ (Mizuno et al. 1995), the age of the T Tauri stars formed in this cloud is ~$6x10^6$ yr (Cohen and Kuhi 1979). In Heiles Cloud 2, star formation occurs spontaneously and is quietly progressing. This situation is different from that in the Orion molecular cloud. Stars born in this region are low mass stars similar to the sun. There is no evidence of strong heating source and shocks in this region. Thus there are no sources of strong ultraviolet radiaton that destroys the ice mantles.

In this region, both field stars shining through the cloud as well as young stellar objects (YSOs) associated with the cloud have been found by Elias (1978), Kim (1990), Tamura et al. (1987, 1991), and Itoh et al. (1996). The criterion to distinguish the field stars from YSOs is whether the location for the objects on the JHK color-color diagram lies within the region where the colors of dwarfs and giants are distributed. 62 out of the 76 field stars whose magnitudes are brighter than 9 mag at K band were observed. The H-K color of the observed sources ranges from 0 to 1.9, which corresponds to A_V of 0 to 21 mag. The intrinsic color of 12 sources out of our 62 sources have been estimated by Elias (1978). In addition, standard stars, HR1394 (F0V, Te=7,700 K, m_V=4.49), HR1497 (B3V, Te=17,900K, m_V=4.28), and HR1590 (A0V, Te=9,900K, m_V=5.81), were observed for calibration of telluric and instrumental corrections. These are selected because the spectral type of the stars is approximated the planck function and the location of the stars is near the Heiles Cloud 2.

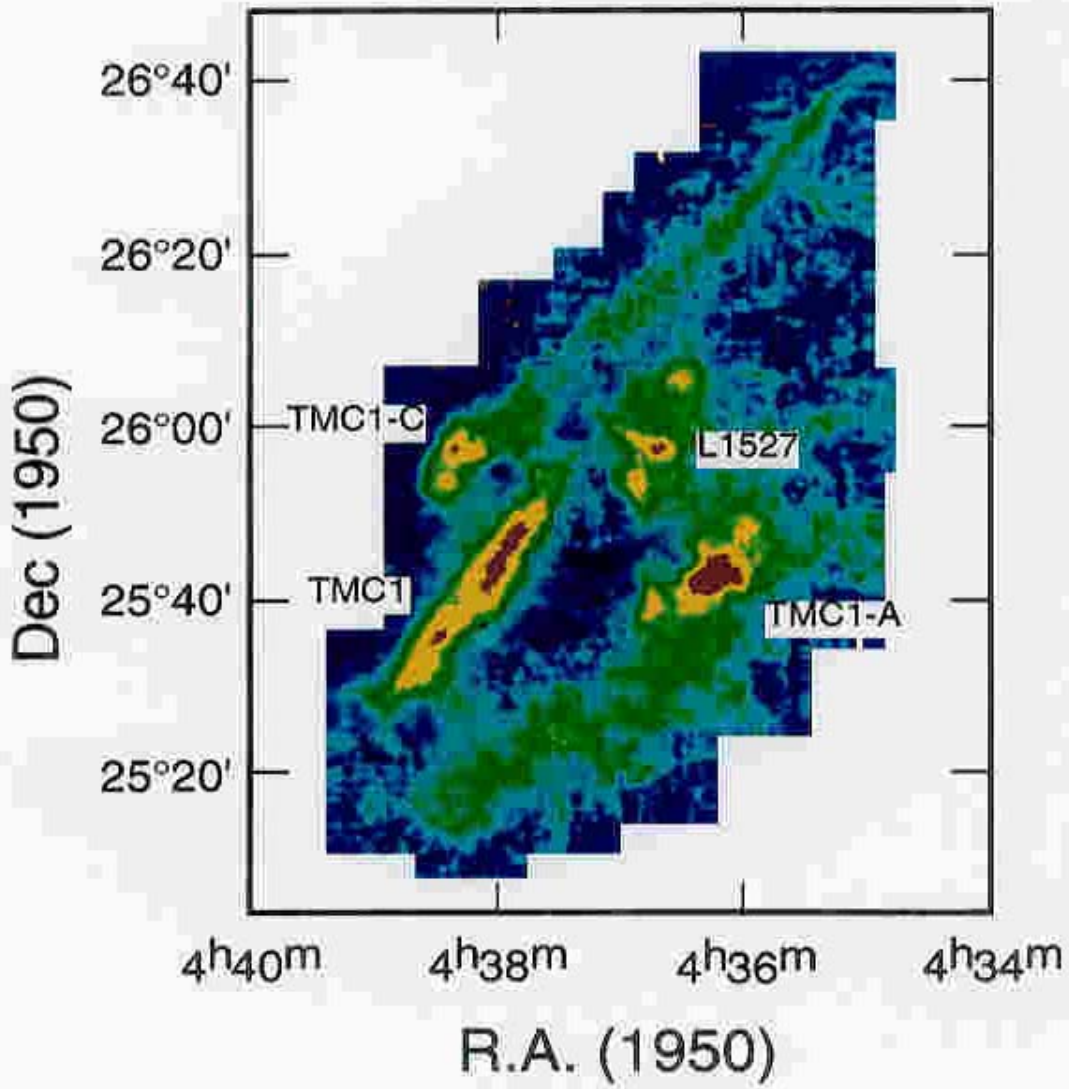

Fig. 2-1-1. $C^{18}O$ map of Heiles Cloud 2. Nobeyama 45m (Sunada & Kitamura 1997). 17″ beam = 2,400 A.U. if the distance to the Taurus is assumed 140pc. The red areas means high column density and blue areas means low column density. The 4 filaments and clumps are clearly seen.

2-1-2. Observational log and instrument, PASP2

The observations were conducted in three separate runs. The observing dates and facilities are as follows: (1) from 28 through 30 in October 1994 with 2.3m Infrared telescope in Wyoming Infrared Observatory (WIRO), (2) from 5 through 9 in November 1994 with 1.5m telescope in Mt. Lemmon Observation Facility (MLOF) and (3) from 11 through 20 in October 1995 with 2.3m Infrared telescope in WIRO.

We used a near-infrared spectrometer PASP2 (Prism Array Spectro-photo Polarimeter 2) with a wavelength coverage from 1.26 to 4.2 μm simultaneously. The parameters of PASP2 are listed in Table 2-1-2. In these observations the prism mode is used. Correspondence between wavelength and channel number of the detector is listed in Table 2-1-3. Two stars, Elias 15 and Tamura 8, were observed by the channel starting 1.333 μm (hereafter 1.33 mode). For others objects the channel starting 1.260 μm was used (hereafter 1.26 mode). We also employed a chopping of the telescope secondary with a frequency of 1 Hz and a separation of 20″ in the direction of east to west.

Table 2-1-1*. PASP2 parameters.

Wavelength coverage	1.26~4.2 μm
resolving power ($\lambda/\Delta\lambda$)	40 (prism mode) 200 (grating mode for 3 μm band) 300 (grating mode for 4 μm band)
Throughput	50%
Aperture Ratio	F/18
Detector	InSb 32ch (Hamamatsu-photonics)
Cooler	Solid Nitrogen (50K)
Readout method	Charge Integrating Amplification
Readout noise	~100e-
Nominal detection limit†	H band: 14.0 mag K band: 12.7 mag L band: 10.0 mag

*: from Honda (1997).

†: assuming 1.3m reflector, prism mode, 1 sec integration, and S/N =1.

Table 2-1-2. Wavelength vs. channel number.

CH	Wavelength (μm)	Wavelength(μm)
1	1.260	1.333
2	1.408	1.479
3	1.548	1.617
4	1.684	1.751
5	1.814	1.878
6	1.938	1.999
7	2.057	2.115
8	2.171	2.227
9	2.280	2.334
10	2.385	2.436
11	2.486	2.536
12	2.658	2.632
13	2.751	2.797
14	2.841	2.885
15	2.928	2.971
16	3.012	3.054
17	3.094	3.135
18	3.175	3.215
19	3.253	3.292
20	3.330	3.368
21	3.405	3.442
22	3.478	3.515
23	3.549	3.584
24	3.619	3.654
25	3.684	3.724
26	3.757	3.791
27	3.823	3.855
28	3.935	3.918
29	3.998	4.030
30	4.060	4.090
31	4.120	4.151
32	4.179	4.208

2-2. Data reduction

The purpose of the data reduction is to obtain the spectra of the sources corrected for both tellulic absorption and instrumental effects, from which we estimate the visual extinction A_V and the optical depth of water ice τ_{ICE}. However, for this purpose, unknown intrinsic spectral energy distribution of each object should be reproduced.

Our data analysis described in detail below has the following advantages over previous observations:

(1) spectral types of individual stars are determined,

(2) continuum levels for spectra features are well determined,

(3) A_V for the individual source is estimated from our own data.

In the previous studies, the extinction A_V is often used from other works (whose derivations differ from source to source), or is estimated roughly by assuming the spectral type of the sources. In addtion, the planck function of blackbody radiation is used for continuum level.

Our reduction procedure is explained in section 2-2-1 and possible problems and error estimations are described in section 2-2-2.

2-2-1. Reduction procedures

2-2-1-1. Determination of spectra

Raw data include : (1) electric dark, which is generated in the detector and electric circuits, (2) uneven sensitivity in individual pixels of the detector, and (3) background level of atmosphere. In order to obtain the correct spectra of objects, these should be removed.

Dark currents and sky background level of atmosphere are canceled by subtraction of two images obtained by secondary chopping. This operation was made on-line.

The uneven sensitivity among pixels is corrected by dividing raw data of object by those of standard star whose spectral energy distribution is known in advance. Let raw data of object to be [OBJ]i, that of standard star [STD]i. The spectrum Fi of the object is derived by,

$$Fi = [OBJ]i / [STD]i * [BB]i, \qquad (2\text{-}1)$$

where i is channel number of PASP2 detector (i=1~32) and [BB]i is the Planck function of blackbody radiation with an effective temperature of the standard star. For better correction, the standard star must be selected which

are observed at the time and air mass similar to the object.

To demonstrate the validity of this procedure, spectra of several standard stars were reduced in the same manner. Three standard stars, HR1394 (F0V, Te=7,700K), HR1497 (B3V, Te=17,900K) and HR1590 (A0V, Te=9,900K) are used. Derived spectra of each standard stars with the Planck function of blackbody radiation with effective temperature are shown in Fig. 2-2-1. Each spectral distribution are in good agreement with the Planck function, although the absolute value of HR1497 is slightly small. Therefore, our procedures provide correct spectra.

2-2-1-2. Estimation of spectral type and determination of continuum level

In order to estimate absorption depth of water ice and visual extinction, we need information of intrinsic spectral energy distribution of the object. Although the spectral types of 12 out of 62 objects have been identified before our work, those of the rest have not yet been known.

We estimate their spectral types as follow. We use a set of "template stars" whose spectral type are known and whose spectra have been observed with PASP2 (Gotoh et al. in preparation, Honda 1997). In addition, spectral type of our objects are predicted to be giant stars (about 90%) by a star count model (Jones et al. 1981). Therefore, the templates of giant stars, not of dwarfs, are used. There is a good relationship between spectral type of giant star and 2.3μm photospheric CO absorption depth (Kleinmann & Hall, 1986). The spectral type of the template with appropriate reddening which minimizes the difference of the CO absorption is used as the intrinsic spectral type of the source.

There are 15 objects whose spectral types cannot be estimated with this method. Seven of the 15 objects do not have sufficient signal-to-noise ratio or have anomalous spectra. Four of the 15 objects have less CO absorption than that of G8III, suggesting that these objects may be G0~G8. Four of 15 have no τ_{CO}, therefore regarded as dwarfs.

Table 2-2-1. Wavelength vs. weight for broad band photometry.

		1.26 mode	1.33 mode			1.26 mode	1.33 mode
band	ch	weight	weight	band	ch	weight	weight
J	1	1.139	1.398	L′	21	0.000	0.005
	3	-0.139	-0.398		22	0.050	0.215
H	2	0.009	0.328		23	0.585	0.856
	3	0.81	0.982		24	0.905	0.888
	4	0.965	0.797		25	0.845	0.836
	5	0.323	0.003		26	0.854	0.872
K	6	0.075	0.353		27	0.869	0.881
	7	0.664	0.841		28	0.970	0.970
	8	0.939	0.960		29	0.936	0.835
	9	0.997	0.700		30	0.695	0.600
	10	0.410	0.184		31	0.501	0.342
	11	0.014	0.000		32	0.122	0.004

These values are derived from Bessell & Brett (1988).

For J band, the weights are that the flux for J band effective wavelength of 1.22μm is derived by extrapolation. However, good accuracy of the photometry cannot be expected.

2-2-1-3. Reddening

The interstellar extinction, A_λ, can be approximated $A_\lambda \propto \lambda^{-\alpha}$ (Martin & Whittet 1990). Therefore, we assume that the reddening law in the Heiles Cloud 2 is $A_\lambda = \beta\lambda^{-\alpha}$. The index α and coefficient β were determined from our data with the following equations:

$$\begin{cases} \dfrac{\lambda_H^{-\alpha} - \lambda_K^{-\alpha}}{\lambda_K^{-\alpha} - \lambda_{L'}^{-\alpha}} = \dfrac{E_{H-K}}{E_{K-L'}} \\ \beta = \dfrac{E_{K-L'}}{\lambda_K^{-\alpha} - \lambda_{L'}^{-\alpha}} \\ A_\lambda = \beta\lambda^{-\alpha} \end{cases} . \qquad (2\text{-}2)$$

Where λi (i=H, K, L′) is effective wavelength of each band, E_{H-K} and $E_{K-L'}$ are color excess of H-K and K-L′, respectively. Since our data cover the whole wavelength range for H, K and L′ bands, the software photometry is conducted by making a transmission of H, K and L′ broad band filters. The weight vs. channel number are listed in Table 2-2-1. The color excesses of

E_{H-K} and $E_{K-L'}$ are derived from the photometry of objects and template stars.

Since only infrared observation have been conducted, A_V is estimated from the infrared color excess with using the next formula (Elias 1978),

$$A_V = 12 \times E_{H-K} \qquad (2\text{-}3)$$

This formula was derived from the V band and infrared photometry of H and K band toward the Taurus dark cloud.

2-2-1-4. Absorption depth of water ice

Absorption depth of water ice, τ_{ICE}, is derived from,

$$\tau_{ICE} = \ln \frac{F_{continuum}(3.1)}{F_{object}(3.1)}, \qquad (2\text{-}3)$$

where $F_{continuum}(3.1)$ is the continuum determined in the procedure 2 and $F_{object}(3.1)$ is the flux of the object. For 1.26 mode, 17 ch (3.094 μm) is used and for 1.33 mode, 16ch (3.054 μm) is used.

2-2-2. Error estimations

(1) Photometry

The results of J, H, K and L′ photometry as well as K magnitude, J-K, H-K, and K-L′ are listed in Table 2-2-2. Error, or deviation derived with the statistical method in eq. (2-1) is typically smaller than 0.01 mag for all bands. But reproduction and effect of software filtering in the photometry must be considered.

The reproduction error was estimated from the scatters of data for standard stars obtained in each night. Typical standard deviation is about ±0.1 mag at K, and ±0.05, ±0.02 and ±0.05 mag in J-K, H-K, and K-L′ colors, respectively. Large error in J-K comes from the large error of the J band photometry since the J magnitude is derived by extrapolation. Therefore, the J band photometry is not used in the discussion below.

For the software filtering effect, since errors of H-K and K-L′ is smaller than that due to reproduction, they can be ignored.

The H-K color for all objects derived in this observation (hereafter simply, [PASP2]) was compared with that by Kim and Itoh (hereafter [KI]) in Fig. 2-2-1. The relationship between this work and Kim and Itoh is [PASP2] = 1.03(±0.019)x[KI]-0.034(±0.012) for H-K. This means that H-K of PASP2 is consistent with that of Kim and Itoh.

(2) Spectral type

Optical depth of the photometric CO bandhead at 2.3μm, τ_{CO}, was derived for all template stars. Fig. 2-2-2. shows the correlation between spectral type and τ_{CO}. The dashed line shows the uncertainty. The uncertainty corresponds to roughly sub-spectral type of ±1, which is equivalent to τ_{CO} of 0.02~0.03 mag. Thus the uncertainty for the estimation of spectral type is roughly sub-spectral type of ±1.5, which corresponds to intrinsic color of (H-K)i = ±0.02~0.03 mag.

(3) color excess and A_V

The observed value of (H-K)o has an error of ±0.02 and the uncertainty of intrinsic color (H-K)i is ±0.02~0.03 mag. Thus color excess E_{H-K} has error of ±0.03 and the error of A_V is ±0.4 mag, when A_V/E_{H-K}=12 is assumed.

It should be stressed that there has been no such systematic determination of A_V of as many as 50 sources, so far. This is the best estimation of A_V of the sources in Taurus.

(4) optical depth of water ice

The statistical error of τ_{ICE} derived is smaller than ±0.01~0.02 mag. However, the error by profile fitting has typically ±0.02~0.03 mag. Thus the error of τ_{ICE} is about ±0.03~0.05 mag, again one of the best and extensive estimates in the Taurus molecular cloud.

Our systematic estimation of the A_V and τ_{ICE} with small errors of as many as 50 sources in the Taurus molecular cloud will thus provide a strong tool for the study of the relationship of A_V and τ_{ICE}.

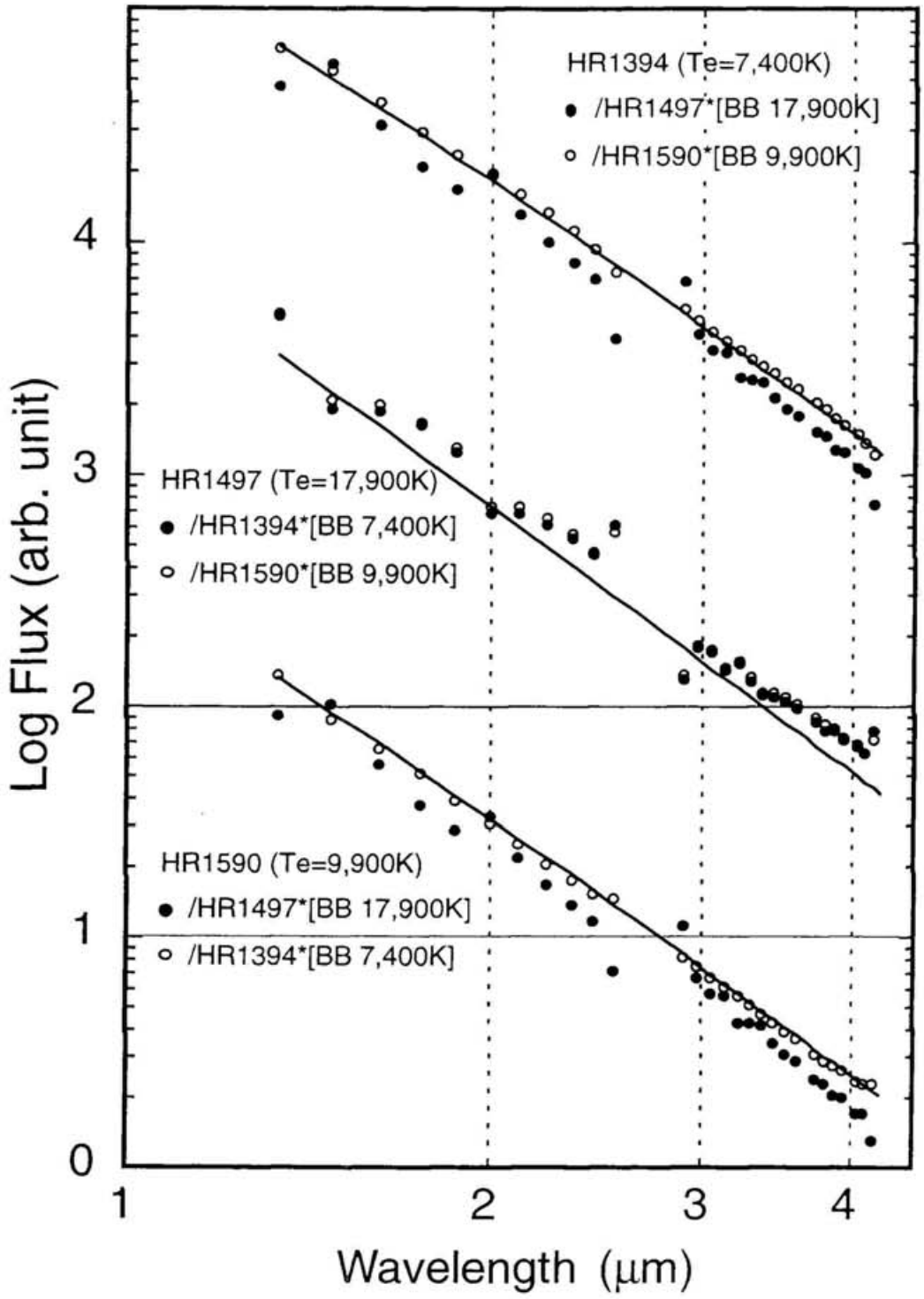

Fig. 2-2-1. Division a standard star by another standard star. Solid lines are the Planck function of blackbody radiation with effective temperature of each standard stars. Spectra of each standard stars are correctly obtained.

Table 2-2-2-(a). Position and photometry.

Object	R.A.(1950)	Dec(1950)	K	J*-K	er.J*-K	H-K	er.H-K	K-L'	er.K-L'
Elias16[1]	4.36340	26.0550	5.37	5.64	0.13	1.92	0.02	1.32	0.05
HCl109_20[2]	4.38431	25.3242	10.06	4.48	0.83	1.71	0.06	1.13	0.06
Tamura8[3]	4.37530	25.4857	7.68	5.31	0.18	1.88	0.03	1.22	0.05
Elias15	4.36228	25.4709	7.14	4.21	0.46	1.46	0.02	0.93	0.05
HC0607_40	4.36462	25.4102	9.97	3.52	0.16	1.15	0.07	0.91	0.59
Kim59[4]	4.38266	25.2120	7.88	2.87	0.05	0.87	0.02	0.52	0.05
Kim49	4.37422	25.2610	9.46	2.61	0.06	0.79	0.03	0.59	0.06
Kim58	4.38259	25.1339	9.62	2.47	0.07	0.77	0.03	0.59	0.06
HC0606_94	4.36476	25.4327	10.22	2.72	0.12	0.83	0.05	0.68	0.08
Kim6	4.34239	26.0430	6.85	2.46	0.05	0.78	0.02	0.48	0.05
Kim52	4.37522	25.2547	7.34	2.17	0.05	0.63	0.02	0.47	0.05
Kim46	4.37097	25.5329	7.55	2.36	0.05	0.69	0.02	0.49	0.05
Kim32	4.36020	25.4416	8.38	2.51	0.05	0.82	0.02	0.52	0.05
Kim34	4.36050	26.1155	8.36	1.92	0.05	0.57	0.02	0.38	0.06
Kim10	4.34444	25.4329	3.20	1.79	0.05	0.65	0.02	0.61	0.05
Kim69	4.39321	25.2137	5.64	1.60	0.05	0.46	0.02	0.33	0.05
Kim23	4.35354	25.4512	10.00	1.78	0.05	0.51	0.02	0.45	0.07
Tamura17	4.40582	25.1442	1.80	1.53	0.04	0.45	0.02	0.42	0.05
Kim15	4.34566	25.2213	5.39	1.54	0.04	0.42	0.02	0.29	0.05
Elias19	4.41143	25.1921	6.19	1.41	0.05	0.36	0.02	0.26	0.05
Kim29	4.35475	25.5350	7.63	1.74	0.05	0.52	0.03	0.39	0.06
Kim30	4.35479	25.2824	4.26	1.46	0.05	0.37	0.02	0.27	0.05
Kim28	4.35416	25.1206	7.48	1.53	0.05	0.40	0.02	0.27	0.06
Kim2	4.34112	26.1016	7.48	1.62	0.05	0.43	0.02	0.42	0.34
Kim14	4.34581	25.5115	8.34	1.27	0.05	0.37	0.02	0.28	0.06
Kim45	4.37079	26.0734	8.44	1.60	0.05	0.51	0.02	0.35	0.05
Kim13	4.34546	25.5814	8.60	1.59	0.05	0.49	0.02	0.38	0.05
Kim65	4.39151	25.1115	8.83	1.54	0.05	0.48	0.02	0.40	0.05
Kim5	4.34212	25.1832	5.84	1.31	0.05	0.32	0.02	0.24	0.05
Elias29	4.34121	25.1131	6.20	1.19	0.05	0.33	0.02	0.24	0.05

Table 2-2-2-(b). Position and photometry.

Object	R.A.(1950)	Dec(1950)	K	J*-K	er.J*-K	H-K	er.H-K	K-L'	er.K-L'
Kim92	4.41033	25.2738	7.13	1.31	0.05	0.31	0.02	0.22	0.05
Kim84	4.40398	25.1752	7.51	1.45	0.05	0.39	0.02	0.09	0.06
Kim22	4.35313	26.0445	8.02	1.24	0.05	0.39	0.02	0.37	0.05
Kim104	4.41367	25.1333	8.38	1.18	0.06	0.25	0.04	0.25	0.07
Kim27	4.35415	25.2052	8.31	1.43	0.05	0.43	0.02	0.26	0.05
Kim21	4.35267	25.2101	8.59	1.40	0.05	0.43	0.02	0.29	0.05
HD283809	4.38205	25.4906	5.56	0.75	0.05	0.29	0.02	0.17	0.05
Kim17	4.35110	25.3618	6.34	1.21	0.05	0.30	0.02	0.20	0.05
Kim94	4.41068	25.4942	7.78	1.24	0.05	0.29	0.02	0.19	0.08
Kim83	4.40321	25.1347	8.47	0.98	0.05	0.26	0.02	0.25	0.06
HD29647	4.38039	25.5350	5.63	0.44	0.05	0.18	0.02	0.15	0.05
Kim108	4.41414	25.5602	7.27	1.03	0.05	0.22	0.02	0.17	0.05
Kim68	4.39293	25.4215	7.24	0.93	0.05	0.25	0.02	0.17	0.05
Kim72	4.39407	25.3041	8.22	0.84	0.05	0.25	0.02	0.13	0.06
Kim85	4.40499	25.5529	8.27	1.04	0.05	0.27	0.02	0.20	0.05
Kim74	4.39499	25.3841	8.53	0.87	0.07	0.21	0.04	0.12	0.06
Kim125	4.42424	25.2359	6.63	0.72	0.05	0.18	0.02	0.10	0.05
Kim91	4.41020	25.3507	7.38	0.87	0.04	0.20	0.02	0.19	0.05
Kim112	4.42002	25.5853	7.57	0.91	0.06	0.20	0.03	-0.09	0.05
Kim122	4.42407	25.4817	8.01	0.77	0.05	0.18	0.03	0.12	0.05
Kim118	4.42283	25.5643	8.06	0.73	0.05	0.19	0.02	0.14	0.05
Kim129	4.42576	25.4229	8.29	0.65	0.05	0.16	0.02	0.16	0.06
Kim123	4.42411	25.5923	8.23	0.73	0.05	0.13	0.02	0.22	0.05
SAO76676	4.34209	25.3740	4.46	0.63	0.05	0.14	0.02	0.19	0.05
SAO76725	4.40003	26.0858	5.10	0.78	0.05	0.19	0.02	0.11	0.05
Kim110	4.41539	26.0216	7.36	0.80	0.05	0.20	0.02	0.15	0.06
Kim43	4.37056	25.2946	7.54	0.72	0.05	0.17	0.02	0.10	0.06
Kim126	4.42447	25.2946	8.52	0.65	0.05	0.12	0.02	0.19	0.05
Kim116	4.42131	26.1111	8.70	0.61	0.05	0.13	0.03	0.15	0.06
HD283807	4.41374	25.5041	8.65	0.36	0.05	0.07	0.02	0.09	0.05

Table 2-2-2-(c). Position and photometry.

Object	R.A.(1950)	Dec(1950)	K	J*-K	er.J*-K	H-K	er.H-K	K-L'	er.K-L'
Kim121	4.42389	25.3734	8.37	0.24	0.05	0.06	0.02	0.08	0.06
SAO76740	4.43075	25.5648	6.93	0.04	0.05	0.03	0.03	-0.16	0.06

Object: 1.Elias 1978, 2.Itoh 1995, 3.Tamura et al. 1987, 4.Kim 1990.

Position: For Right Acention 4.42389 shows 4h42m38s.9 and for declination 25.3734 means 25°37'34". Kim 1990. see also Itoh 1995.

K magnitude: Error is typically 0.1 mag.

J*: estimated by extrapolation, see section 2-2-2 (1) and Table 2-2-1. The error of J photometry is ±0.05 mag. Thus J photometry is not used in after discussion due to such large error.

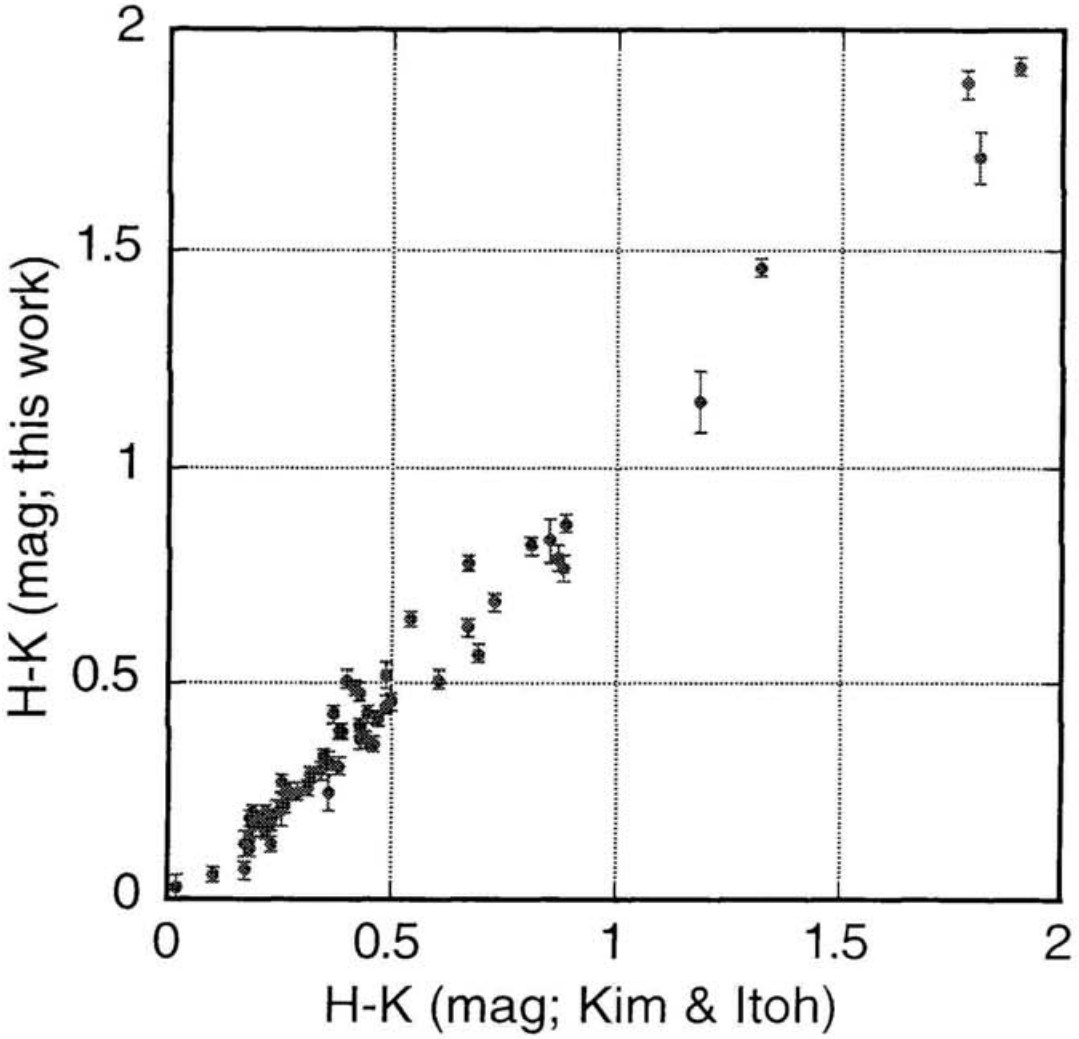

Fig. 2-2-2. Comparison of H-K photometry in this work and Kim and Itoh. The relationship between [PASP2] and [KI] is [PASP2]=1.03(±0.019)x[KI]-0.034 (±0.012). Since the difference between [PASP2] and [KI] is within ±0.03 mag, our software photometry provides consistent result with that used broad band filter.

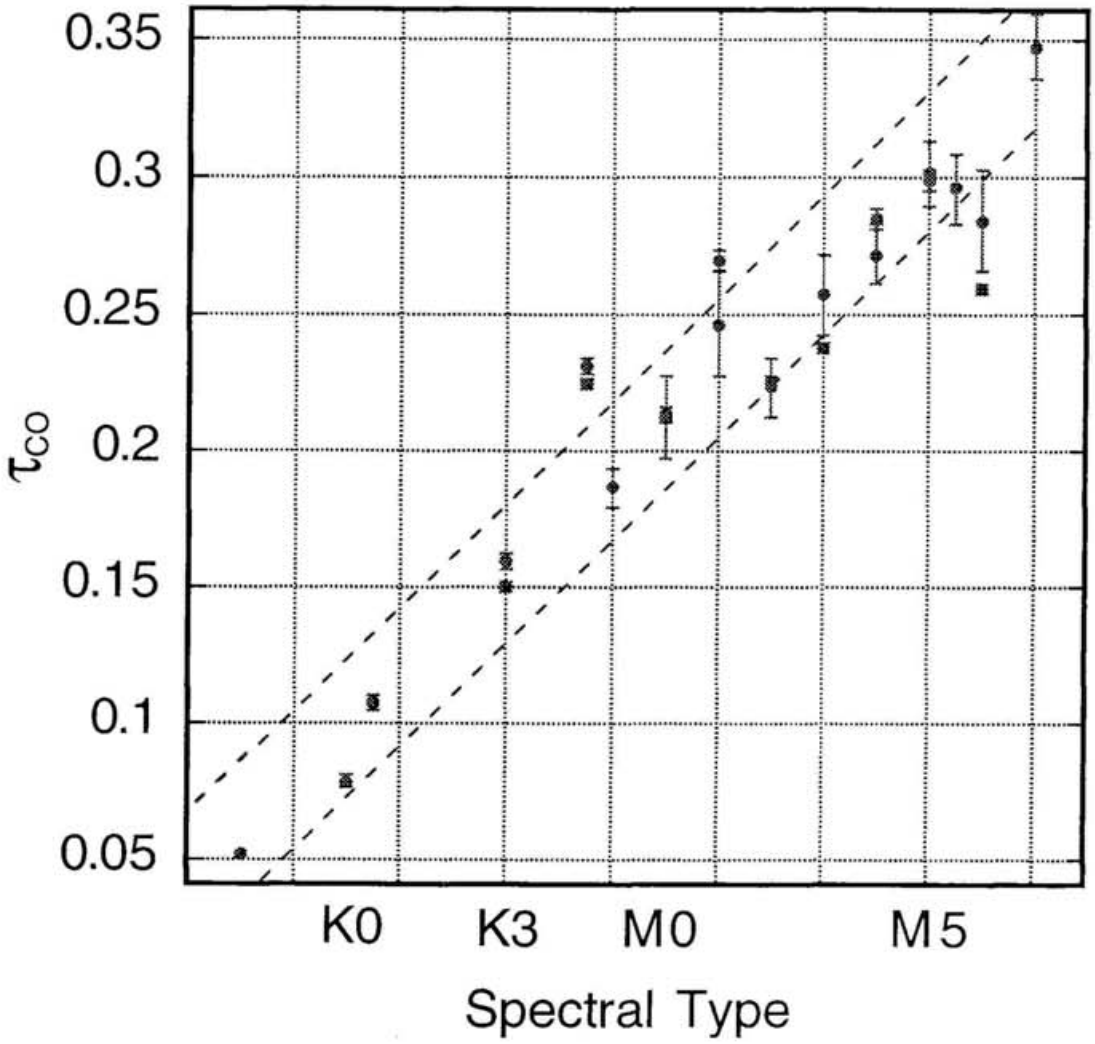

Fig. 2-2-3. Spectral type vs. τ_{CO} of templates. Region between two green dashed lines indicates unceirtanties of τ_{CO} and spectral type. The unceirtanty is ±0.02~0.03 mag for τ_{CO} and is ±1.5 for spectral type.

2-3. Results

Both visual extinction and optical depth of water ice have been estimated for 55 objects in the above procedures. The result of photometry and the spectra of all objects are shown in Table 2-3-1 and Fig. 2-3-1. The determined continuums for 55 objects are also shown.

2-3-1. A_V vs. τ_{ICE}

The relationship between A_V and τ_{ICE} is shown in Fig. 2-3-2. The red filled circles are for this observation and the blue filled circles are for Whittet et al. (1988). Absorption of water ice is detected for above A_V>2~5 mag.

The remarkable point is the threshold A_V, A_{V0}. The A_{V0} of our result is spread in 2~5 mag, while that of Whittet et al. is a constant of 3.3 mag. The scatter in our data does not come from observational error and the data reduction procedure. We will discuss the possible origin of the scatter of A_{V0} in section 3-1-2.

The value of τ_{ICE}/A_V is 0.067±0.003 while that of Whittet is 0.093±0.001. This difference may come from the procedures of determination of continuum level and of estimation of A_V. Some results for objects, which is observed by both us and Whittet et al., are listed in Table 2-3-2. The Table, in addition, includes results obtained by Smith et al. (1993). For absorption depth of water ice, our result is similar to that of Smith et al. and for τ_{ICE}/A_V, each result is slightly different. These similarity and difference come from the reduction procedures. Smith et al. 1993 used spectra of actual template stars for determination of continuum level. Thus similar result of τ_{ICE} was obtained. For A_V estimation, Smith et al. use a relationship of A_V=5.4xE_{J-K}. If equivalent formula for our estimation, A_V=4.6xE_{J-K}, is used, the τ_{ICE}/A_V becomes be consistent with our result. However, Whittet et al. used the Planck function for determination of continuum level and others works for A_V, which is mainly estimated by using the most possible spectral type for object as a representation, not by determination of spectral type for each objects. Therefore, our results are more reliable than those of Whittet et al.

2-3-2. Reddening

The reddening correction method was discussed in section 2-2-1. The result of index α of A_λ is shown in Fig. 2-3-3. Although index α is constant value of 1.8 for standard diffuse region and a dense cloud, ρ Oph, our results for the most objects are clearly different from them. Note that attempt to adopt the power law with index -1.8 is faulse for our data. We will discuss the reason in section 3-2.

2-3-3. Spectral type

It should be checked out that the relationship between our estimated spectral type and their number predicted from the star count (Jones et al. 1981). Figure 2-3-5 shows the histogram of each spectral type. The red bars represent our estimation and the blue bars from star count. Our estimation of spectral type is consistent with that predicted from star count. Note, however, for K0 and K1, our data appear to have overestimated than that of star count, while for K2 and K3, slightly under estimated.

The spectral types of 5 out of 55 objects were identified by previous literetures (Elias 1978, Smith 1993) with employing the same method. Those are listed in Table 2-3-2. Our estimation is in good agreement with the previous results within accuracy of ±1 in the subclass of M and K giants.

Table 2-3-2. Comparison of estimated spectral type.

Object	Elias (1978)	Smith (1993)	This Work
Elias 15	M2III	-	M3III
Elias 16	K1III	K2III	K2III
Elias 19	M4III	-	M3III
Elias 29	G9III	-	K0III
Tamura 17	-	M8III	M6III

* Spectral types of these 5 objects wrer estimated by the same manner, which uses absorption depth of atmospheric CO of the objects at 2.3μm.

Table 2-3-1-(a). Color excess, A_V, τ_{ICE} and spectral type.

Object	E_{J^*-K}	er.E_{J^*-K}	E_{H-K}	er.E_{H-K}	$E_{K-L'}$	er.$E_{K-L'}$	A_V	er.A_V	τ_{ICE}	er.τ_{ICE}	sp.typ.
Elias16	4.89	0.16	1.80	0.03	1.22	0.05	21.6	0.40	1.27	0.03	K2III
HCl109_20	4.26	0.83	1.62	0.06	1.05	0.06	19.4	0.72	1.36	0.09	7,000K[1]
Tamura8	4.67	0.21	1.78	0.04	1.15	0.05	21.4	0.42	1.37	0.03	K0III
Elias15	3.03	0.47	1.21	0.03	0.72	0.05	14.5	0.40	0.74	0.03	M4III
HC0607_40	-	-	-	-	-	-	-	-	-	-	-[2]
Kim59	2.12	0.11	0.76	0.03	0.42	0.06	9.12	0.42	0.32	0.03	K2III
Kim49	2.06	0.12	0.71	0.04	0.54	0.06	8.52	0.45	0.36	0.05	G0~8[3]
Kim58	1.88	0.12	0.68	0.04	0.52	0.06	8.16	0.45	0.30	0.05	G8III
HC0606_94	-	-	-	-	-	-	-	-	-	-	-[2]
Kim6	1.43	0.11	0.59	0.03	0.31	0.05	7.08	0.40	0.24	0.04	M0III
Kim52	1.42	0.11	0.52	0.03	0.37	0.06	6.24	0.40	0.19	0.03	K2III
Kim46	1.39	0.11	0.51	0.03	0.34	0.06	6.12	0.40	0.23	0.03	K5III
Kim32	1.88	0.11	0.72	0.03	0.44	0.06	8.64	0.40	0.32	0.04	K0III
Kim34	0.86	0.11	0.36	0.03	0.21	0.06	4.32	0.40	0.17	0.04	M1III
Kim10	-	-	-	-	-	-	-	-	-	-	-[4]
Kim69	0.64	0.11	0.30	0.03	0.17	0.05	3.60	0.40	0.12	0.02	K5III
Kim23	1.10	0.11	0.41	0.03	0.36	0.07	4.96	0.40	0.13	0.10	K1III
Tamura17	0.26	0.11	0.14	0.03	0.19	0.05	1.68	0.40	0.04	0.02	M6III
Kim15	0.40	0.11	0.19	0.03	0.09	0.05	2.28	0.40	0.03	0.02	M3III
Elias19	0.27	0.11	0.12	0.03	0.07	0.05	1.44	0.40	0.03	0.03	M3III
Kim29	0.92	0.11	0.38	0.03	0.27	0.06	4.56	0.46	0.08	0.04	K3III
Kim30	0.44	0.11	0.18	0.03	0.10	0.05	2.16	0.40	0.00	0.02	M0III
Kim28	0.43	0.11	0.17	0.03	0.09	0.06	2.04	0.40	0.00	0.04	M2III
Kim2	0.94	0.11	0.33	0.03	0.33	0.34	3.96	0.40	0.07	0.15	K1III
Kim14	0.59	0.11	0.27	0.03	0.19	0.06	3.24	0.40	0.05	0.05	K1III
Kim45	1.02	0.11	0.43	0.03	0.28	0.06	5.11	0.40	0.07	0.04	G8III
Kim13	0.90	0.11	0.38	0.03	0.29	0.06	4.56	0.40	0.11	0.05	K1III
Kim65	0.86	0.11	0.38	0.03	0.31	0.06	4.56	0.40	0.13	0.05	K1III
Kim5	0.44	0.11	0.18	0.03	0.10	0.05	2.16	0.40	0.02	0.03	K4III
Elias29	0.51	0.11	0.22	0.03	0.15	0.05	2.64	0.40	0.05	0.03	K1III

Table 2-3-1-(b). Color excess, A_V, τ_{ICE} and spectral type.

Object	E_{J^*-K}	er.E_{J^*-K}	E_{H-K}	er.E_{H-K}	$E_{K-L'}$	er.$E_{K-L'}$	A_V	er.A_V	τ_{ICE}	er.τ_{ICE}	sp.typ.
Kim92	0.17	0.11	0.07	0.03	0.03	0.06	0.78	0.50	0.04	0.03	M3III
Kim84	-	-	-	-	-	-	-	-	-	-	-[4]
Kim22	-	-	-	-	-	-	-	-	-	-	-[4]
Kim104	0.22	0.12	0.08	0.04	0.09	0.07	0.90	0.40	0.05	0.09	K5III
Kim27	0.75	0.11	0.33	0.03	0.17	0.06	3.96	0.40	0.08	0.03	K1III
Kim21	0.72	0.11	0.33	0.03	0.20	0.06	3.96	0.40	0.01	0.04	K1III
HD283809	0.81	0.11	0.31	0.03	0.22	0.05	3.72	0.40	0.11	0.02	B3V[5]
Kim17	0.18	0.11	0.11	0.03	0.03	0.06	1.32	0.40	0.00	0.02	M0III
Kim94	0.15	0.11	0.07	0.03	0.00	0.08	0.88	0.40	0.00	0.1	M2III
Kim83	0.34	0.11	0.16	0.03	0.17	0.06	1.92	0.40	0.00	0.03	K0III
HD29647	0.54	0.11	0.20	0.03	0.17	0.06	2.40	0.40	0.06	0.02	B7IV[6]
Kim108	0.22	0.11	0.08	0.03	0.05	0.06	0.96	0.40	0.01	0.02	K3III
Kim68	0.25	0.11	0.15	0.03	0.08	0.06	1.80	0.40	0.00	0.02	K1III
Kim72	0.25	0.11	0.16	0.03	0.06	0.06	1.92	0.40	0.02	0.03	G8III
Kim85	0.36	0.11	0.17	0.03	0.11	0.06	2.04	0.40	0.02	0.04	K1III
Kim74	0.32	0.13	0.13	0.05	0.06	0.07	1.61	0.57	0.03	0.05	G0~8[3]
Kim125	0.08	0.11	0.08	0.03	0.02	0.05	1.00	0.40	0.00	0.02	K0III
Kim91	0.19	0.11	0.10	0.03	0.10	0.06	1.20	0.40	0.00	0.03	K1III
Kim112	-	-	-	-	-	-	-	-	-	-	-[4]
Kim122	0.19	0.12	0.09	0.03	0.05	0.06	1.12	0.41	0.00	0.03	G8III
Kim118	0.17	0.11	0.11	0.03	0.08	0.06	1.30	0.40	0.02	0.03	G0~8[3]
Kim129	0.00	0.11	0.00	0.03	0.00	0.06	0.00	+0.6	0.00	0.03	6,000K[7]
Kim123	0.09	0.11	0.04	0.03	0.14	0.06	0.44	0.40	0.00	0.05	K0III
SAO76676	-0.11	0.11	0.02	0.03	0.09	0.05	0.24	0.40	0.00	0.03	K2III
SAO76725	0.10	0.11	0.09	0.03	0.02	0.05	1.10	0.40	0.00	0.02	K1III
Kim110	0.16	0.11	0.10	0.03	0.07	0.06	1.18	0.40	0.00	0.03	K0III
Kim43	0.14	0.11	0.08	0.03	0.02	0.07	0.97	0.40	0.04	0.04	G8III
Kim126	0.06	0.11	0.04	0.03	0.11	0.06	0.43	0.40	0.00	0.03	G8III
Kim116	0.06	0.11	0.05	0.03	0.09	0.06	0.58	0.41	0.04	0.05	G0~8[3]
HD283807	0.00	0.11	0.00	0.03	0.00	0.06	0.00	+0.6	0.00	0.03	10,000K[7]

Table 2-3-1-(c). Color excess, A_V, τ_{ICE} and spectral type.

Object	$E_{J'-K}$	er.$E_{J'-K}$	E_{H-K}	er.E_{H-K}	$E_{K-L'}$	er.$E_{K-L'}$	A_V	er.A_V	τ_{ICE}	er.τ_{ICE}	sp.typ.
Kim121	0.00	+0.1	0.00	+0.05	0.00	+0.05	0.00	+0.6	0.00	0.03	8000K[7]
SAO76740	-	-	-	-	-	-	-	-	-	-	-[4]

A_V: A_V is derived from $A_V=12xE_{H-K}$.
1: Assumed the effective temperature of F dwarf, which is predicted as the most possible spectral type in dwarf.
2: The spectral type cannot be estimated due to less S/N.
3: $\tau_{CO} < \tau_{CO}$ of G8III.
4: peculiar spectrum
5: The spectral type was estimated by Straizys 1985.
6: The spectral type was estimated by Crutcher 1985.
7: τ_{CO}~0. Blackbody fitting between K and L'.

Table 2-3-2. Comparison of our result of τ_{ICE} and A_V with previous results.

	E16	T8	E15	T17	29647	283809	283807	τ_{ICE}/A_V	A_{V0}
This work	1.27 ±0.03	1.37 ±0.03	0.74 ±0.03	0.04 ±0.02	0.06 ±0.02	0.11 ±0.02	<0.03	0.067 ±0.003	2~4
Whittet (1988)	1.60 ±0.08	1.40 ±0.08	0.92 ±0.08	0.11 ±0.06	0.10 ±0.06	0.13 ±0.05	<0.07	0.093 ±0.001	3.3
Smith (1993)	1.26 ±0.01	-	-	0.055 ±0.01	0.11 ±0.01	0.075 ±0.01	-	0.059 ±0.003	2.6

This work : Templates of giant stars are used. The A_V was estimated.
Whittet : blackbody fitting was used. The A_V is adopted from others works.
Smith : Templates of giant stars are used. The A_V is adopted from others works.

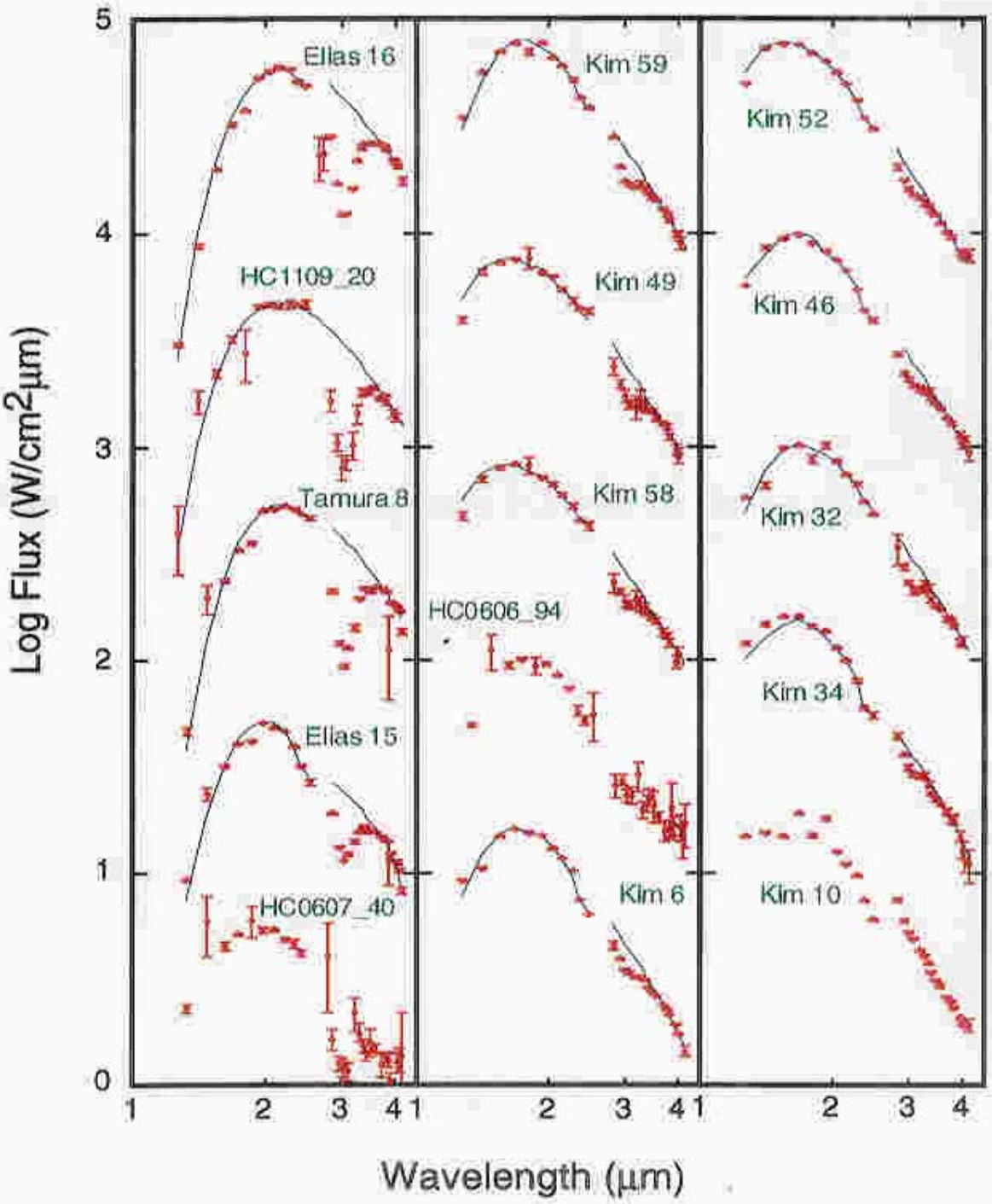

Fig. 2-3-1-(a). Obtained spectra. The red filled circles are for observation and blue solid curves are determined continuum level.

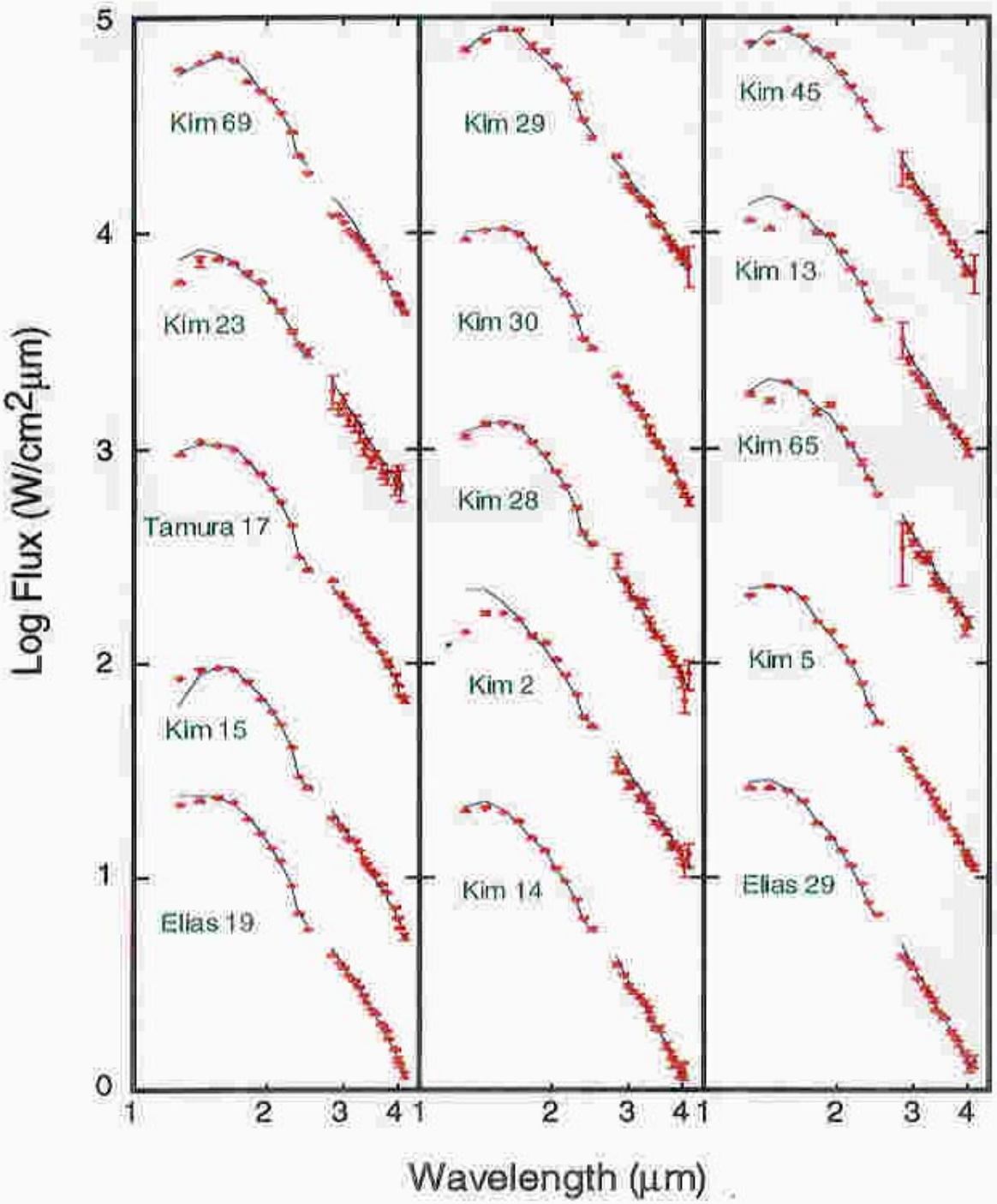

Fig. 2-3-1-(b). Obtained spectra. The red filled circles are for observation and blue solid curves are determined continuum level.

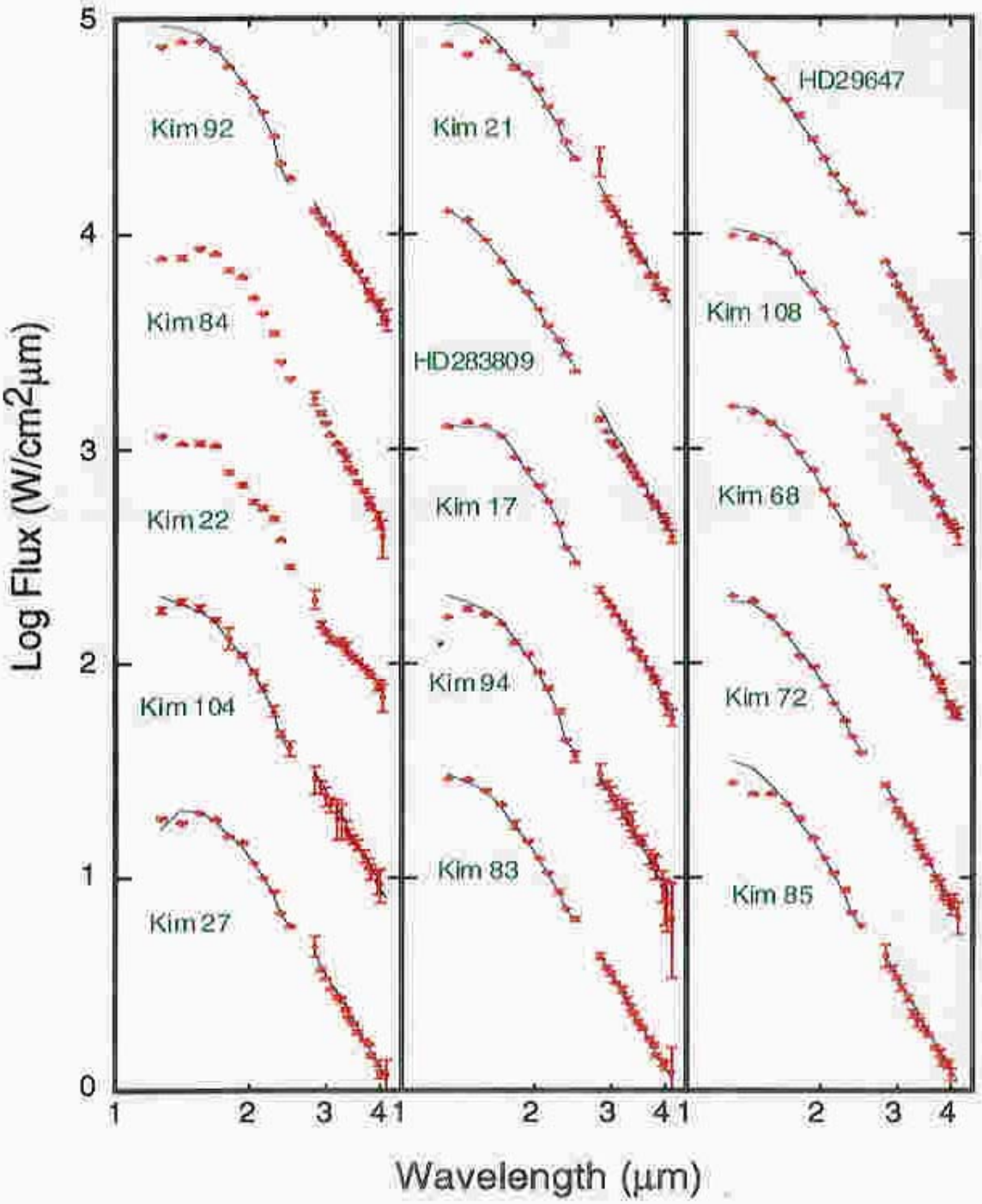

Fig. 2-3-1-(c). Obtained spectra. The red filled circles are for observation and blue solid curves are determined continuum level.

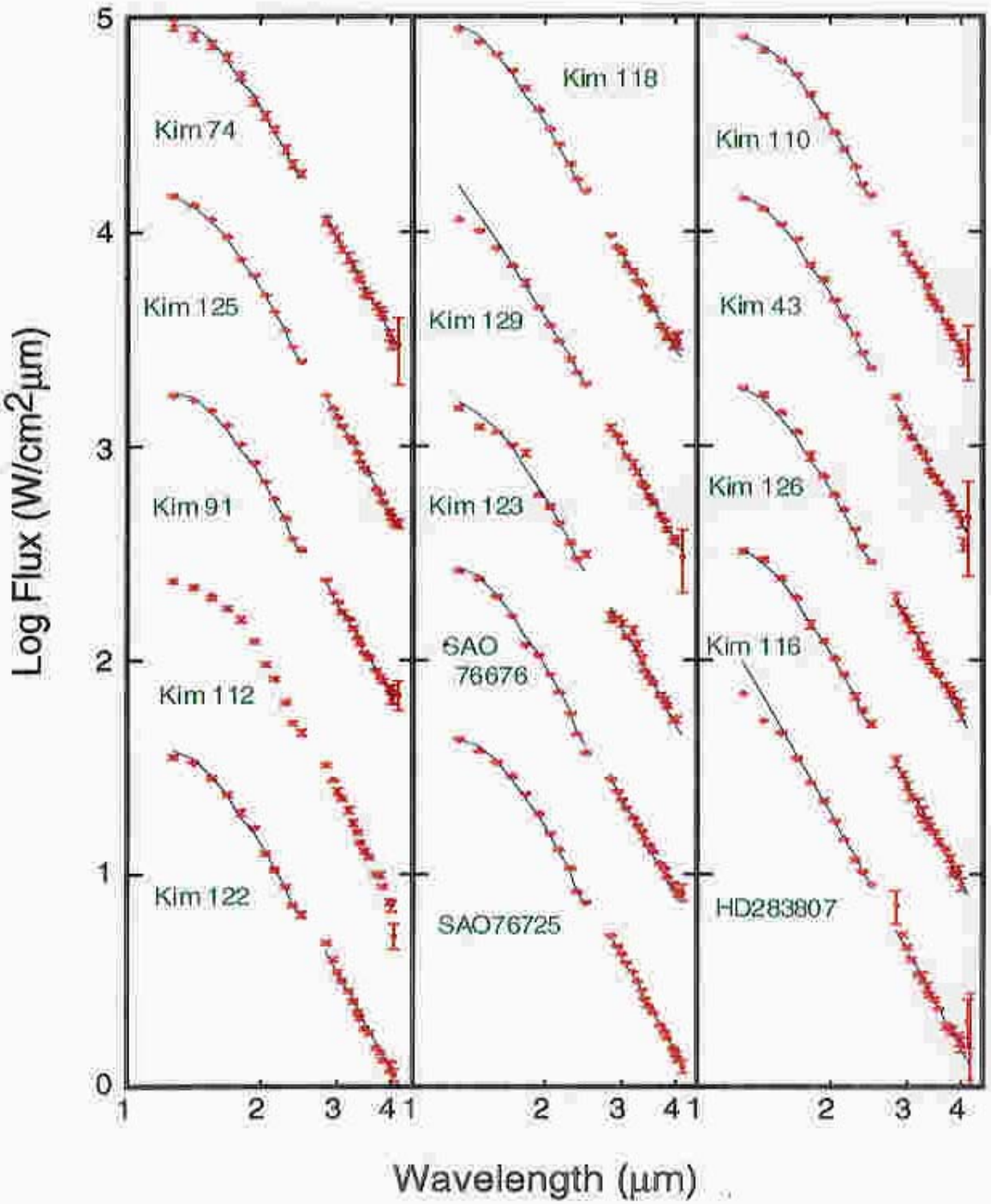

Fig. 2-3-1-(d). Obtained spectra. The red filled circles are for observation and blue solid curves are determined continuum level.

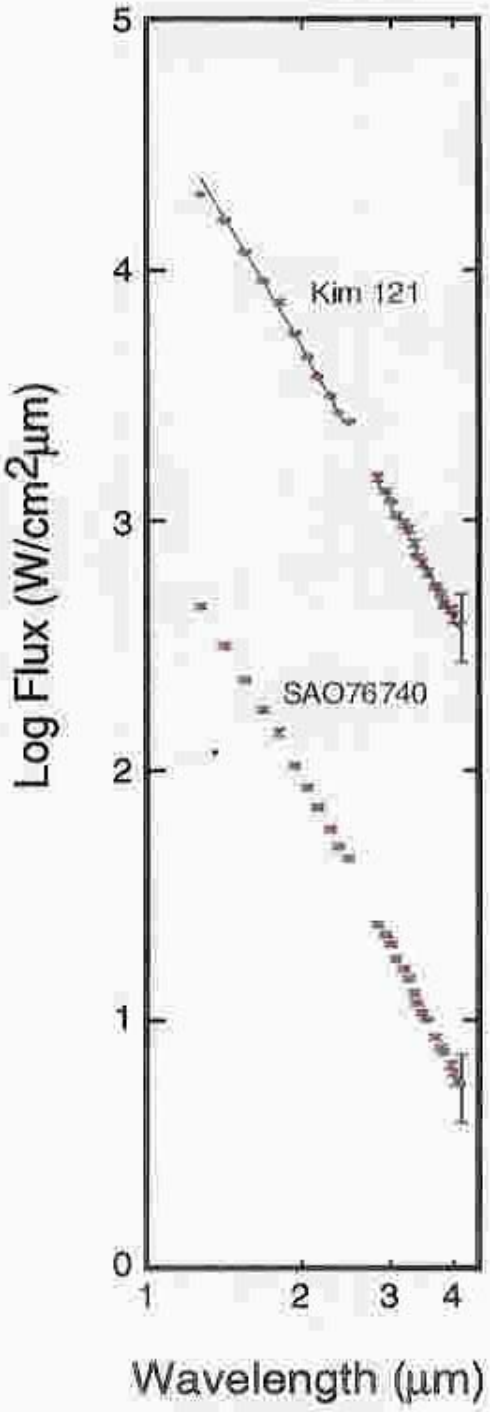

Fig. 2-3-1-(e). Obtained spectra. The red filled circles are for observation and blue solid curves are determined continuum level.

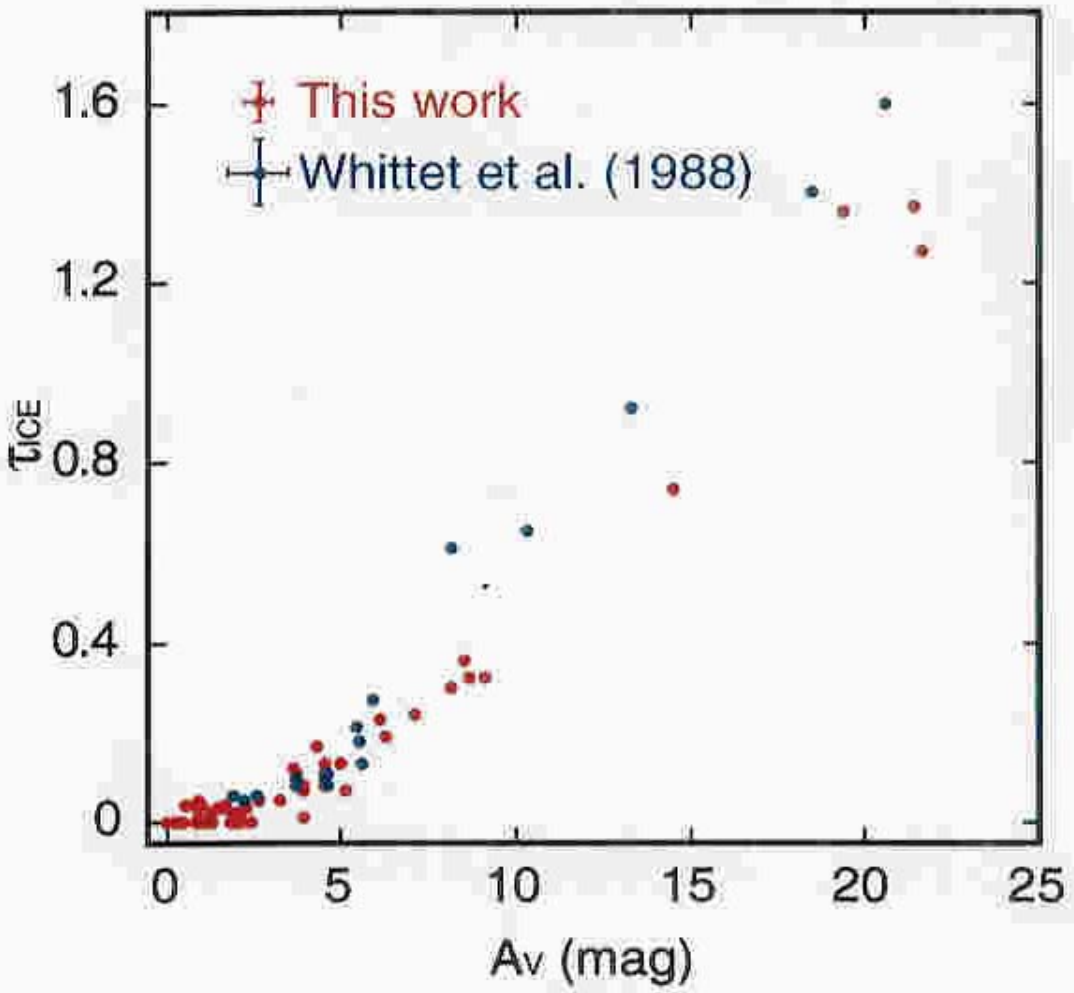

Fig. 2-3-2. A_V vs. τ_{ICE}. The red filled circles are for this observation and blue filled circles are for Whittet 1988. The A_V threshold for our result has some scatter within 2~5 mag, while that for Whittet is 3.3 mag. This scatter is discussed in section 3-1-2. The difference of the value τ_{ICE}/A_V is caused by a difference from reduction procedures (see in section 2-3-1).

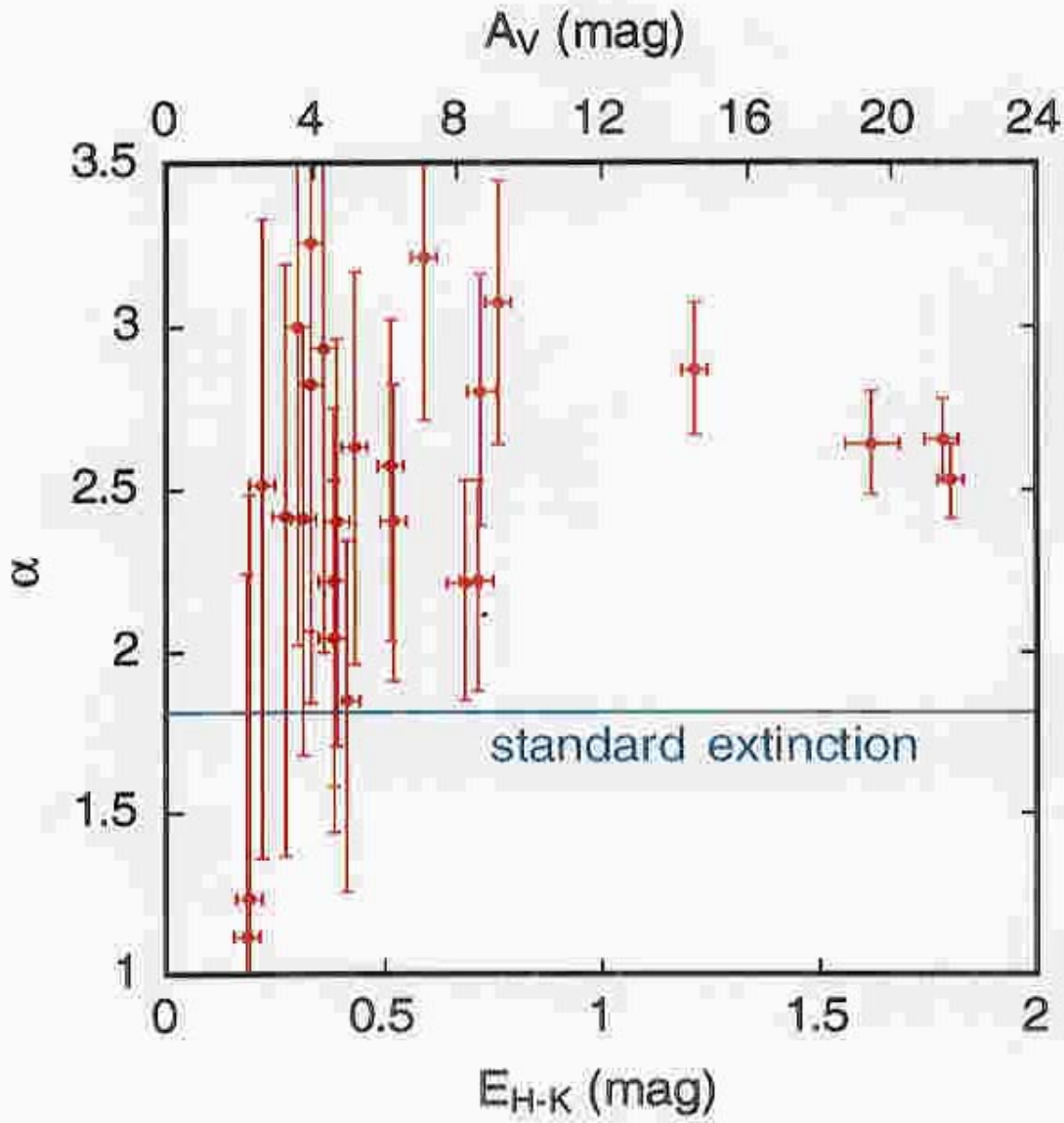

Fig. 2-3-3. Relationship between E_{H-K} and index α. For the most objects, the indecies α are different from the value 1.8 for standard diffuse cloud and a dense cloud , ρ Oph (see section 1-2-2 and Martin & Whittet 1990).

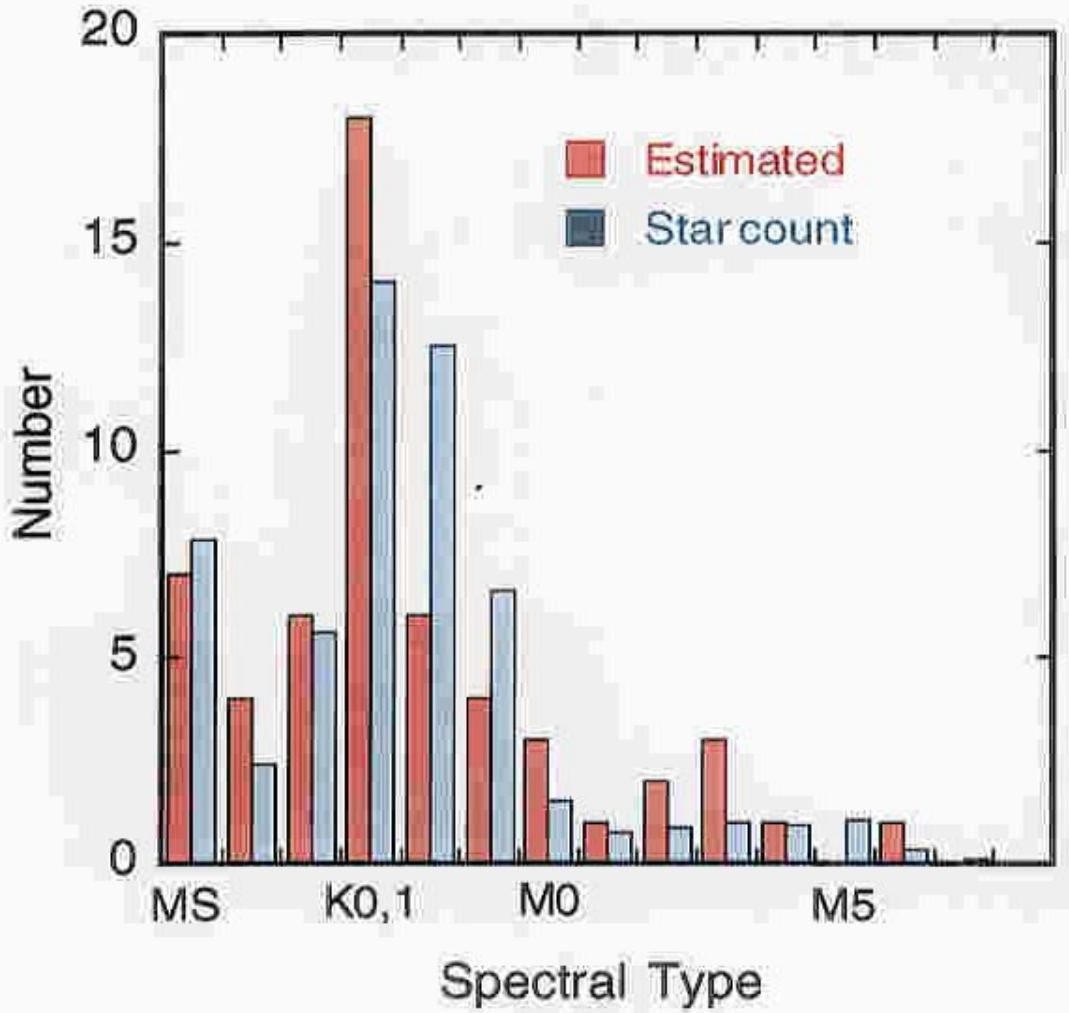

Fig. 2-3-4. Histgram of observed stars by spectral type. The star count model was from Jones (1981). Our spectral type classification is roughly consistent with the star count model.

3. Discussion

3-1. Water ice distribution in Heiles Cloud 2

3-1-1. Water ice map and comparison with $C^{18}O$ map

Sunada & Kitamura (1997) obtained a $C^{18}O$ (J=1-0) map of Heiles Cloud 2 region with the 45m Nobeyama radio telescope. The diameter of the beam is 17 arcsec, providing the highest spatial resolution map of the cloud. Figure 3-1-1 shows a pseudo-color map of the total integrated intensity of $C^{18}O$ emission. The map shows the column density of $C^{18}O$, which is roughly proportional to the total integrated intensity. The real scale of the beam diameter corresponds to 2,400 A.U., assuming that the distance to the Taurus molecular cloud is 140 pc. Because of such a high resolution four filamentary and clumpy structures, TMC1, TMC1-C, TMC1-A and L1527 are distinctly seen in Fig. 3-1-1.

The depth of water ice toward the position of the objects can be plotted in a two-dimensional way with filled circles whose diameters are proportional to the depth of the observed water ice. This is regarded as a "water ice map" and has been reported for the first time. In Fig. 3-1-1 this water ice map is superposed on the $C^{18}O$ map. Open circles show the sources whose water ice is undetectable. Most of these sources are situated outside the region where the $C^{18}O$ was observed. For objects with a lower column density, absorption depth of water ice is shallower. Although water ice absorption is not detected for the most of objects outside the $C^{18}O$ map, such a region is shown to have smaller ^{13}CO column density (Onishi 1997, private communication). Objects with especially strong absorption, Elias 16, HC 1109, Tamura 8 and Elias 15, are located in the regions with a high column density, namely, TMC1, TMC1-A and L1527.

These results show that the absorption of water ice is deep toward the region with a high column density, namely, filaments and clumps, in the $C^{18}O$ map.

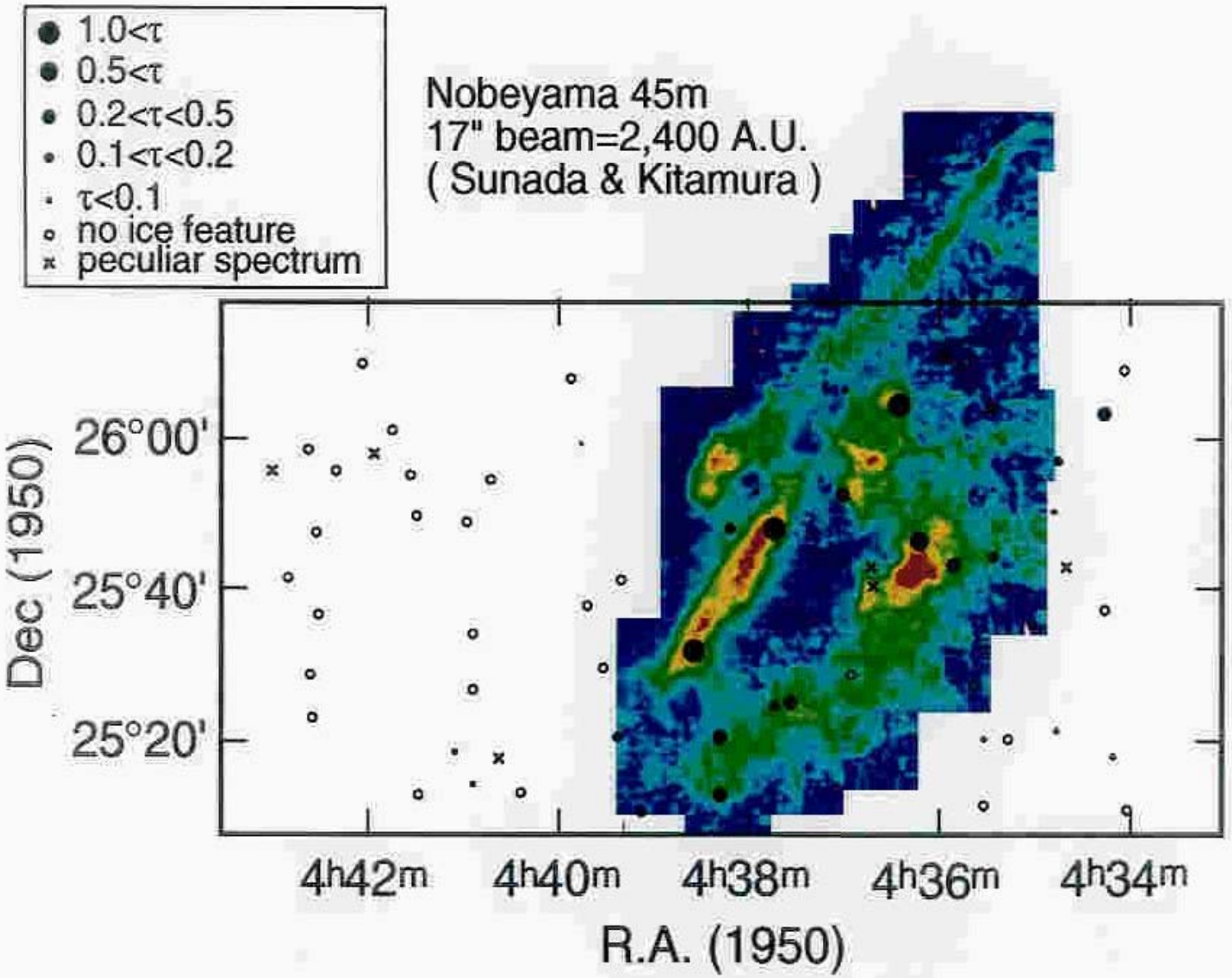

Fig. 3-1-1. Water ice map with $C^{18}O$ map.

3-1-2. Relationship between visual extinction and absorption depth of water ice

The relationship between the visual extinction, A_V, and the absorption depth of water ice, τ_{ICE}, is shown in Fig. 3-1-2. There is a linear relationship for $A_V \geq 3$ mag, and water ice is not detected for $A_V < 2$ mag. This result is consistent with that obtained by Whittet et al. (1988). However, there is a large scatter for $A_V \approx 3$-5 mag. The possible reasons to cause such a scatter are as follows:

(1) Errors in A_V estimation
  1-1. Misidentification of supergiant
  1-2. Uncertainty of the ratio A_V to E_{H-K}
(2) Misidentification of class III objects
(3) Contamination of absorption features other than water ice
(4) Variations of condition for water ice destruction
(5) Effect of geometry of the cloud structure.

These possibilities are discussed below in detail. In summary, the possibilities (1)~(4) are not the main contribution. We suggest the cloud geometry is the most likely origin of the scatter in the A_V threshold.

(1). Errors in A_V estimation

1-1. Misidentification of supergiant

Although we have assumed that the observed objects with the CO absorption at 2.3μm are giant stars, there is a possibility that those are super giants. Supergiants with the same CO absorption depth have an intrinsic color of (H-K)i=0.02~0.04 less than that of giants. Therefore, the A_V is larger by 0.2~0.5 mag. The star count, however, predicts the probability less than one object in all objects (Jones et al. 1981, § 2-3-1). Thus, this effect is negligible.

1-2. Uncertainty of the ratio A_V to E_{H-K}

We have employed the reddening law established by Elias (1978) for the estimation of A_V ($A_V/E_{H-K} = 12$). This value has an uncertainty range of 12~15. This uncertainty causes an underestimation by 20% at most in A_V, Therefore this probably does not greatly change the relationship between A_V and τ_{ICE}.

(2) Misidentification of class III objects

Criterion for identification of the field star is that their colors on the JHK color-color diagram is consistent with those of dwarfs, giants and super giants except for reddening. Class III objects are also located in the same area as those of field stars on the color-color diagram because such objects have no circumstellar matter around it, producing no near-IR excess. This means that class III objects could not be distinguished from field stars by this criterion. Because the class III objects detected so far are considered to exist at the near side of the cloud, there is only one side of the cloud where water ice cannot exist along the line of sight between class III objects and observer, while there are two for field stars. Thus τ_{ICE} of class III is predicted to be larger than that of field stars with the same A_V. This misidentification is predicted by star count to be about 10% in this case.

(3) Contamination of absorption features other than water ice

There are two possible features that could blend with the 3.1 μm absorption feature; one is the long wavelength wing at 2.7 μm of H_2O vapor in the atmosphere of late type stars. Another is the possible absorption of NH_3 ice at 2.97 μm. For the former, the contamination was removed because the template spectrum of actual giant stars were used as continuum for the estimation of τ_{ICE}. For the latter, the NH_3 absorption feature has never been detected for field stars so far. In addition, as the band head of NH_3 absorption is located neighbor channel (between 14 ch, 2.928 μm, and 15 ch, 3.012 μm, for 1.26 mode and 15 ch-2.971 μm for 1.33 mode), this contamination may be negligible.

(4) Variations of conditions for water ice destruction

There is also a possibility that gas temperature and/or intensity of UV field have a local variation. As described in section 1-2-1, such variations of provide the variations of the A_V threshold. However, there is little evidence for local gas temperature changes because no strong UV radiation sources such as OB stars are detected inside or around the Heiles Cloud 2 region. Thus this effect can be ignored.

(5) Effect of geometry of cloud structure.

The structure of the cloud is not as simple as a steamed bun, but will be more complex like in Fig. 3-1-1. Then the relationship between A_V and τ_{ICE} must have a scatter depending on how the direction of the field stars cut the

ice existing region.

From the above discussion, it is found that the most possibility is (5), namely threshold of A_V has scatter caused by the complex density distribution. We consider the geometrical effect of the cloud, (5) in detail below.

In Heiles Cloud 2, the high density regions are located in a ring-like region, which is shown in Fig. 3-1-1, and there are filaments and clumps. The details of 3 dimensional structure of these filaments and clumps can not be determined by our observation since we don't obtain such many objects to cover whole area in the cloud. However, we can find the effect which the structure of the cloud provides the scatter of the threshold of A_V. We assume a simple model of the cloud, which extends to a few pc and has a single clump such as L1527 in the center of the cloud. Let the cloud has ellipsoidal density distribution and the direction of major axis to be the same as the direction of line of sight. The relationship between A_V and τ_{ICE} is estimated by changing the length of the cloud along the major axis.

<Cloud model>

The density distribution of the cloud is assumed:

$$n_H(r,z) = \begin{cases} \dfrac{100}{r^2+(az)^2} & r^2+(az)^2 < 1.0^2 \\ 0 & \text{otherwise} \end{cases} \qquad (3\text{-}1)$$

Where the unit of $n_H(r,z)$ is in N/cm^3, r is the distance along the direction perpendicular to the line of sight and z is the distance along the line of sight, and the unit of both r and z is pc.

The abundance of water ice is assumed to be proportional to n_H. This assumption is consistent with the linear relation between A_V and τ_{ICE}. τ_{ICE}/A_V (=0.067) is used as a mean value of Elias 16, Tamura 8, HC 1109 in this work. The regin where water ice exists is determined by considering the formation and destruction of water ice. The threshold is determined by the criterion that the accretion rate for oxygen atom per surface site, R_{ac}, is equal to UV photodesorption rate of water ice, R_{pd}. R_{ac} can be expressed,

$$R_{ac} \sim 3\times10^{-16}\, n_H\, T_g^{1/2} \qquad s^{-1}, \qquad (3\text{-}2)$$

where n_H is number density of hydrogen and T_g is kinetic temperature of gas and assumed T_g = 50K (Smith et al. 1993, see also Drain & Salpeter 1979). R_{pd} can be expressed,

$$R_{pd} \sim 10^{-12} \exp(-1.84 A_V) \quad s^{-1}. \quad (3\text{-}3)$$

(Smith et al. 1993, see also Boland & de Jong 1982)

<Result>

The relationship between A_V and τ_{ICE} is calculated by changing the parameter a, which is related with the length of the cloud along the major axis. The range is $0.2<a<1.25$, which corresponds to the length of cloud from 0.8 to 5.0 pc.

The region where water ice exists has over 0.2 mag of the threshold of A_V from outside of the cloud. The relationship between A_V and τ_{ICE} for length of 0.8, 1 and 5.0 pc is shown in Fig. 3-1-3. The A_V thresholds are given 0.8, 3.0 and 7.0 for length of 0.8 1 and 5.0 pc, respectively. Therefore the A_V threshold in fact depends on the length of the clump.

Furthermore, we also considered various ellipticities and the net effect on the A_V threshold versus τ_{ICE} were calculated. Fig. 3-1-4. Denser dots indicates a higher probability. The effect of geometry is seen to some extent in Fig. 3-1-4.

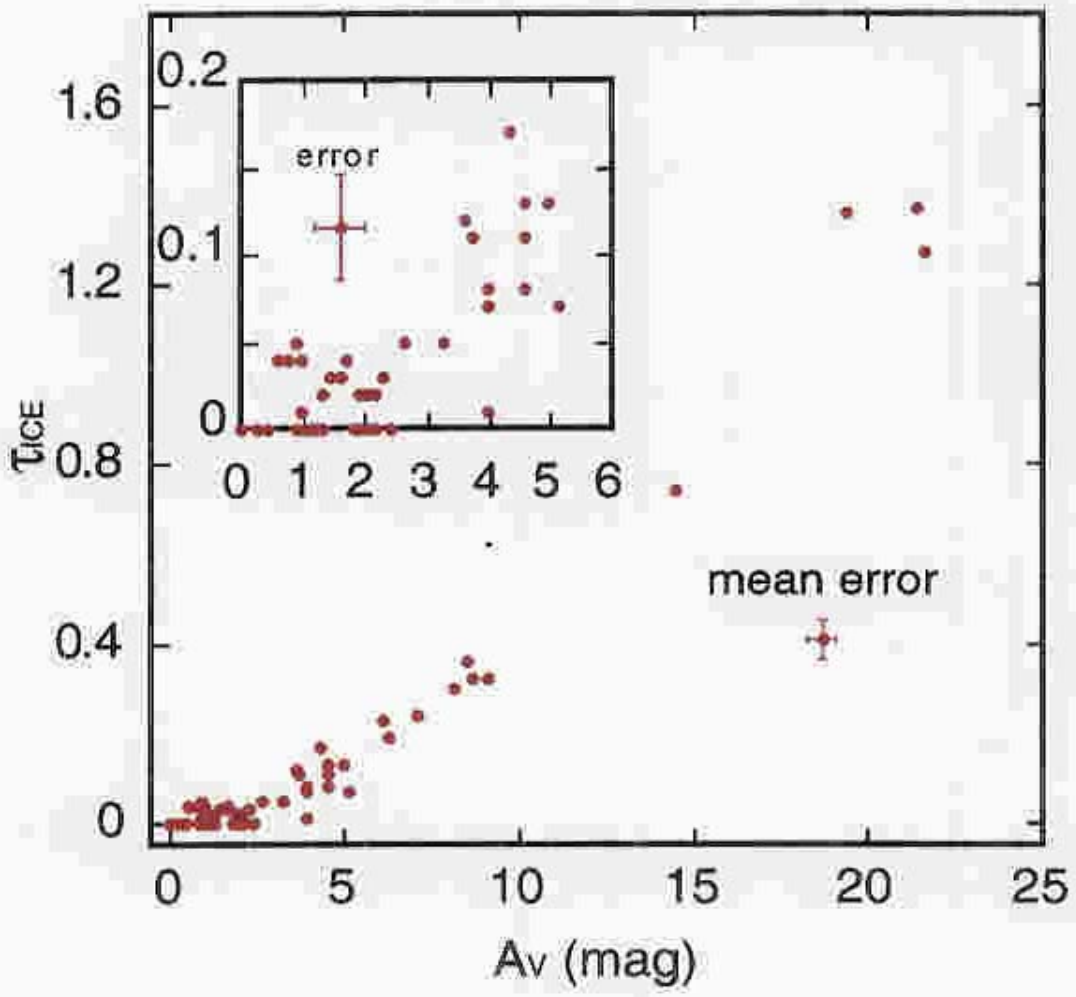

Fig. 3-1-2. A_V vs. τ_{ICE}.

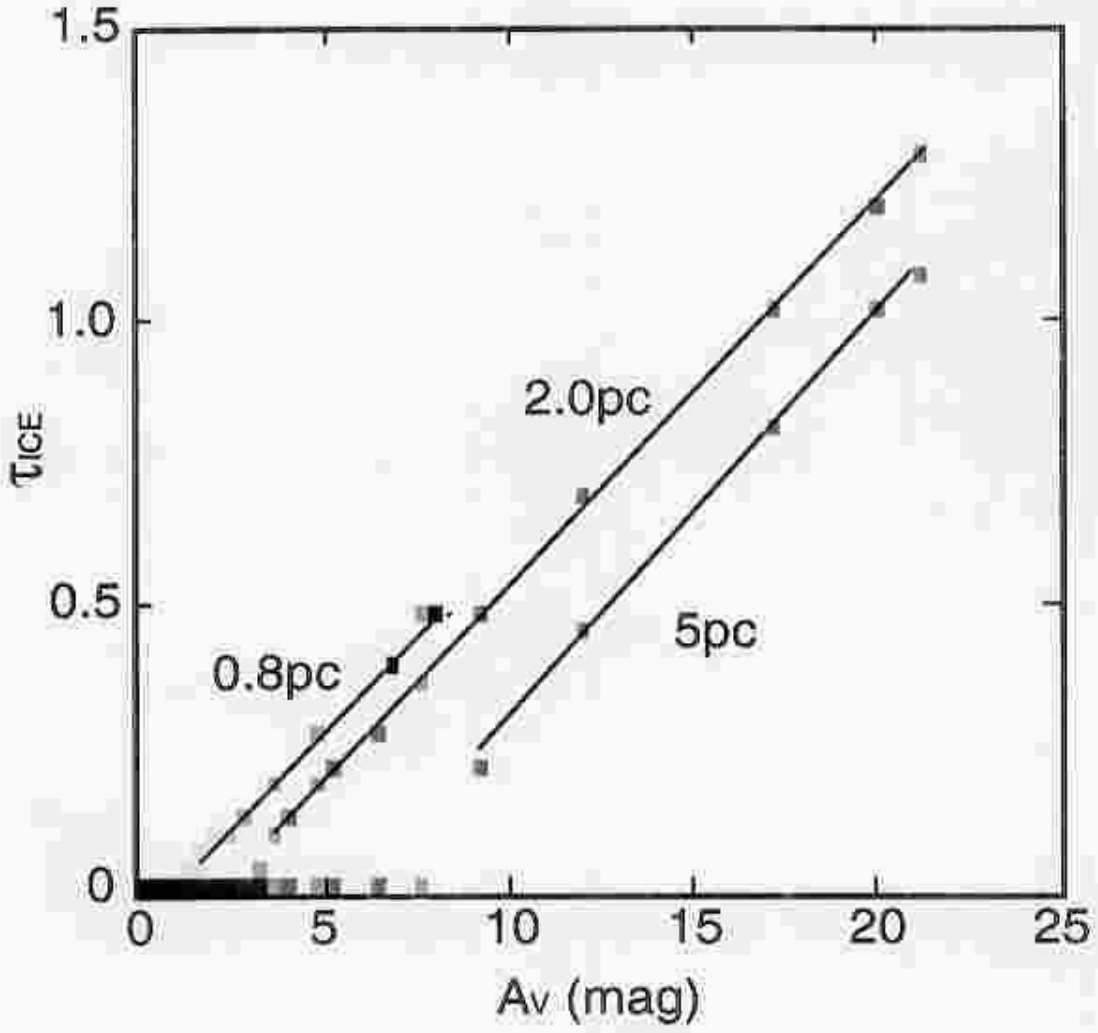

Fig. 3-1-3. Variations of A_V threshold.

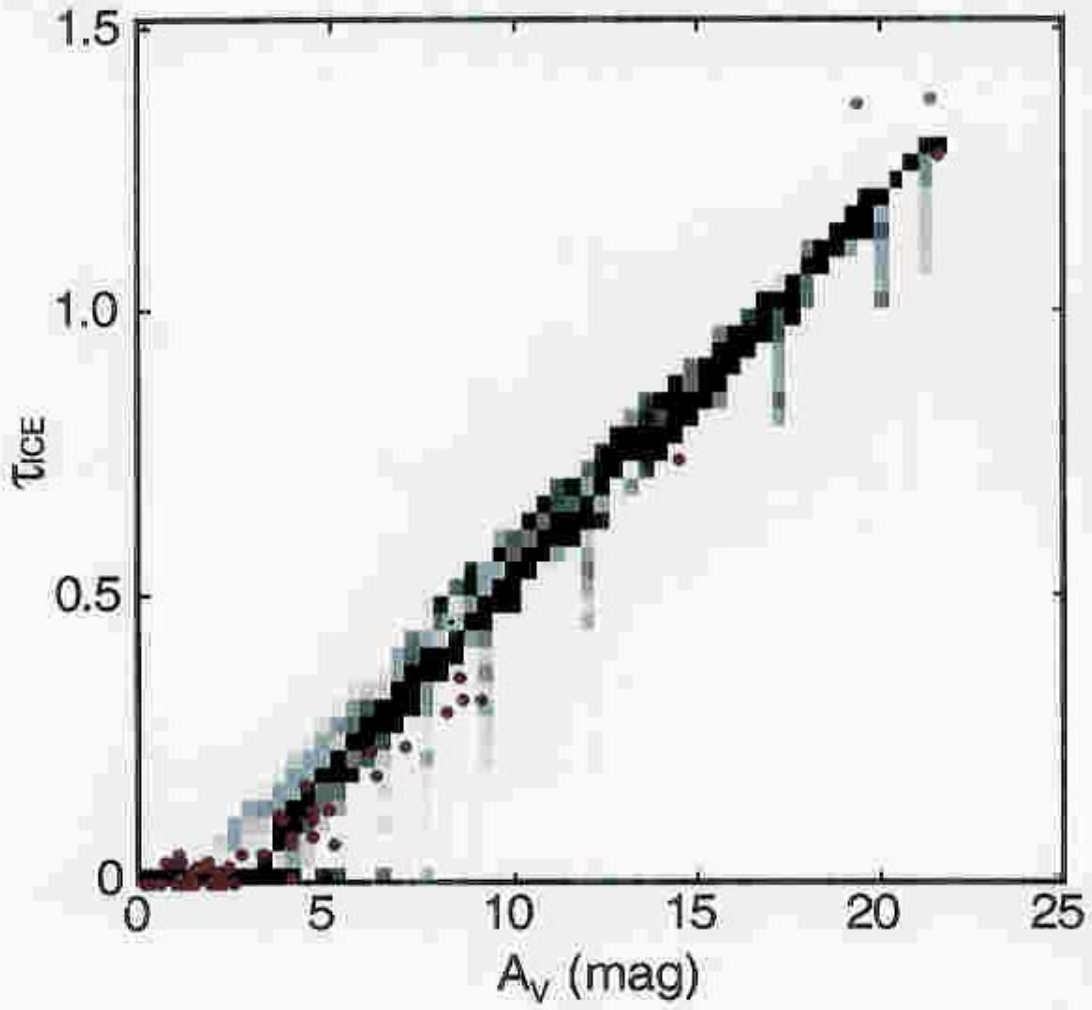

Fig. 3-1-4. Net effect on A_v threshold vs. τ_{ICE}.

3-1-3. 3μm band absorption feature

In previous sections 3-1-1 and 3-1-2, we have discussed the distribution of water ice in Heiles Cloud 2 by concentrating on the depth of water ice absorption and investigating the relationship between τ_{ICE} and A_V. In this section, we will discuss the profile of 3μm band absorption.

As shown in section 1-2-1, comparing with field stars, following two characteristic profiles are seen for massive YSOs;

(1) 3.4μm absorption is deeper than that of field stars.
This is due to water ice deformation by strong UV field radiation from the central young star.

(2) Band width near 3:0μm is narrower.
This means that YSOs have a high temperature component.

Since we have observed 2 low mass protostars, IRAS source 04365+2535 (H-K=2.92) and 04361+2547 (H-K=2.09), toward the Taurus dark cloud, other than 62 field stars, we investigate whether these objects shows such tendency or not.

First we discuss profiles of field stars. 6 profiles of observed field stars, who has enough S/N ratio are shown in Fig. 3-1-5. The red filled circles shows obtained data and the blue dashed curve shows profile of Elias 16, HC1109, Elias 15 and Tamura 8. The latter three sources shows the same profiles as Elias 16. However, Kim 59 and Kim 6 shows peculiar profiles. We select Elias 16, HC1109, Tamura8 and Elias 15 as a standard profile of field stars.

The 2 protostars have similar profiles. A mean of them are used as a YSO profile. In Fig. 3-1-6, this is compared with that of field stars. The red filled circle means field stars and blue curve means YSO profile. For shorter wavelength than 3.0μm, YSO profile shows smaller absorption than Elias 16 and HC1109, while it shows deeper than Tamura 8 and Elias 15. However, for longer wavelength near 3.4μm, YSO profile always shows deeper than field stars. Although our data has a poor spectral resolution to, this YSO profile may have deeper 3.4μm absorption than field stars. If this is real, dust around the low mass YSO deforms enough to change 3.4mm band profile.

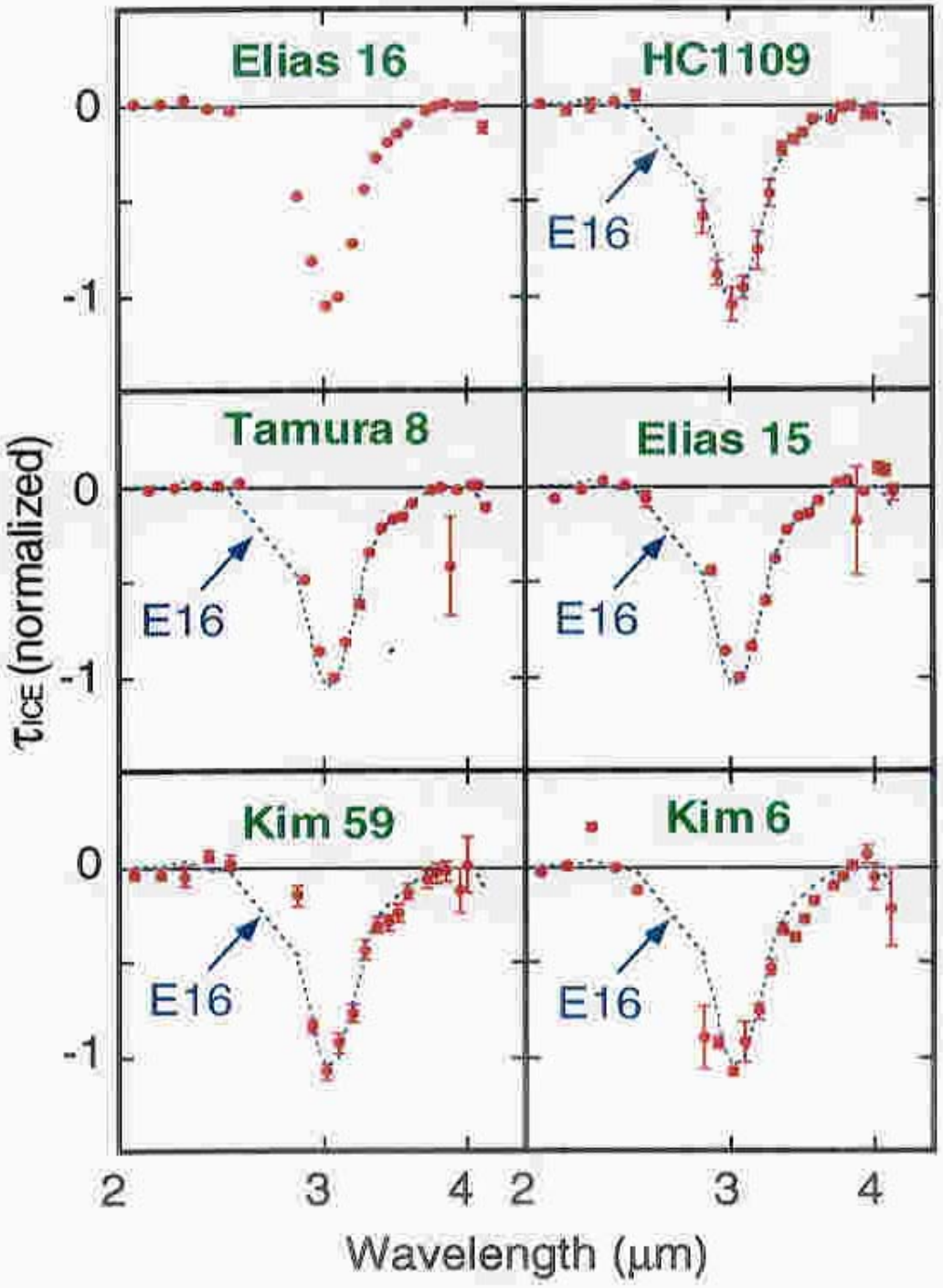

Fig. 3-1-5. Profiles of field stars. The red filled circles mean each field star and blue curve means Elias 16.

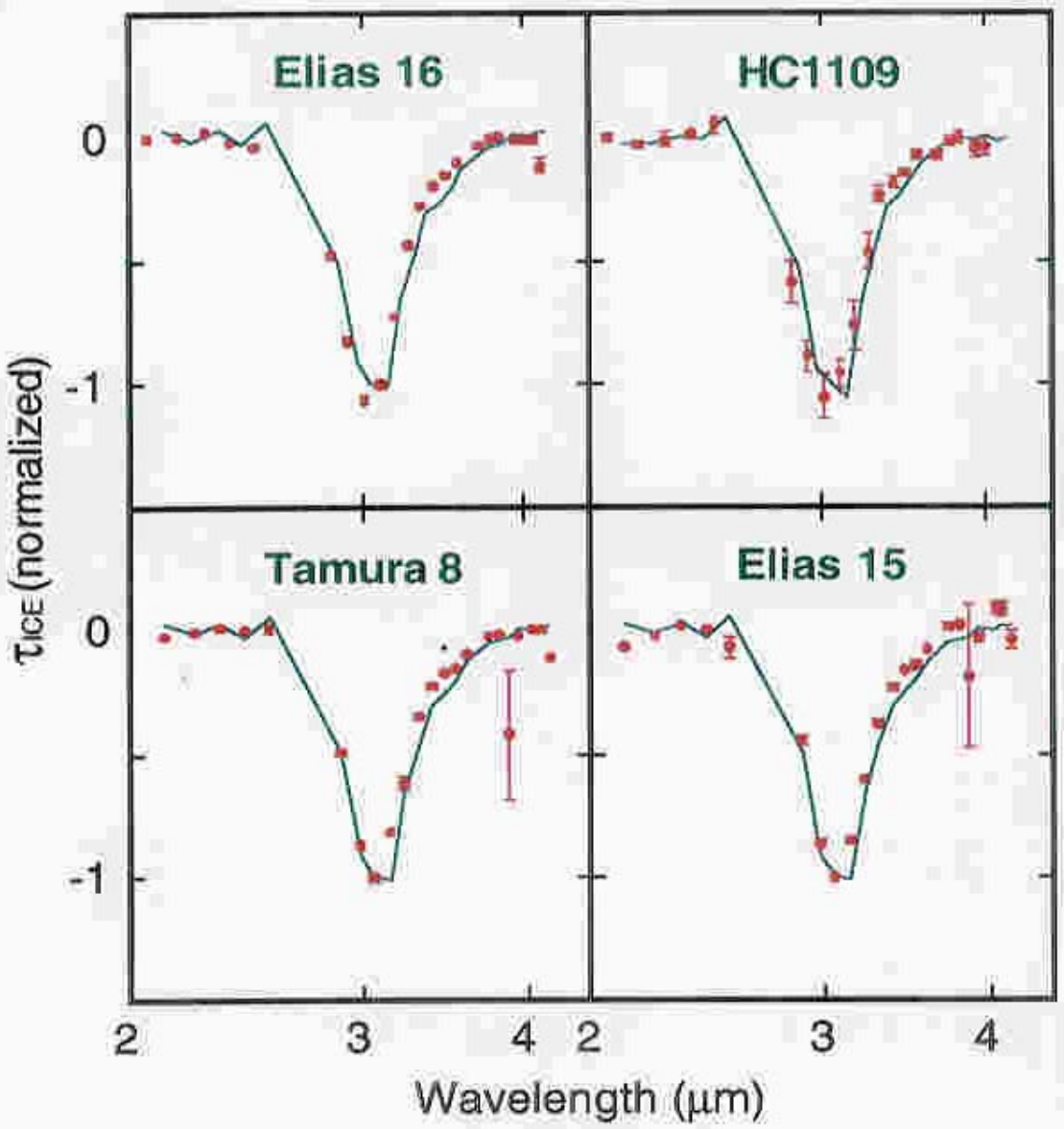

Fig. 3-1-6. comparison with YSO and FS. The red filled circles mean field stars and blue curve means low mass YSO.

3-1-4. Relationship between visual extinction and the column density of $C^{18}O$

Since the carbon monoxide is the most abundant molecule in the molecular cloud next to molecular hydrogen and its emission line in millimeter wavelength can be more readily detected than that of H_2, it has been used as a tracer of cloud. In this section, relationship between the column density of gas such as CO and H_2 and visual extinction, derived from infrared observation, is discussed in detail.

Our A_V was derived by field stars toward the Heiles Cloud 2, while $C^{18}O$, was observed by Sunada and Kitamura (1997), which is an excellent tracer especially for dense clouds because it is optically thinner than ^{12}CO and ^{13}CO. The relationship between A_V in Fig. 3-1-1 and $N(C^{18}O)$ is investigated for 20 objects located on the $C^{18}O$ map shown. Similar attempts were made by Frerking et al. 1982 toward the Taurus molecular cloud complex.

The $C^{18}O$ column density, $N(C^{18}O)$ (N/cm^2), was estimated with the following equation (Mizuno et al. 1996),

$$N(C^{18}O) = 2.4\times10^{14}\frac{\Sigma\tau_A\Delta v/\eta}{1-\exp\left(-\frac{5.3}{T_{ex}}\right)} \qquad (3\text{-}4)$$

where $\Sigma(\tau_A\Delta v)$ is the total integrated intensity, η is the beam efficiency, and T_{ex} is the excitation temperature. The η is adopted 0.5 (Sunada 1997, private communication) and T_{ex} is adopted 8.8 K, is the mean value in the Taurus molecular cloud estimated by Frerking et al. (1982). The result is shown in Fig. 3-1-7 and in Table 3-1-1. The red dots indicates the data of this work while the blue dots are those of Frerking et al. 1982.

For $5<A_V<10$, Elias 15 (A_V=14.6 mag) and Elias 16 (A_V=21.6 mag), our result is consistent with that of Frerking. In this work the region is limited to Heiles Cloud 2, while the entire region in the Taurus dark cloud is sampled by Frerking et al. 1982. Because no clear evidence for the existence of UV sources or shocks in the Taurus region, this is consistent with the previous observations (Schloerb et al. 1984, Onish et al. 1995, Mizuno et al. 1996).

For our result, the following linear relations are obtained,

$N(C^{18}O) = 6.67_{\pm0.90}\times10^{13}\,(A_V+2.46_{\pm1.81})$ $\quad A_V > 4$ mag, $\qquad$ (3-5-a)

$N(C^{18}O) = 1.33_{\pm0.33}\times10^{14}\,(A_V-1.78_{\pm1.14})$ $\quad 10 > A_V > 4$ mag, $\qquad$ (3-5-b)

while that of Frerking,

$N(C^{18}O) = 1.7 \times 10^{14} (A_V - 1.3)$ $21 > A_V > 4$ mag, (3-6)

in which the correlation was corrected by using rarer species $C^{17}O$ and $^{13}C^{18}O$. Our result of (3-5-b) is consistent with (3-6). For $A_V \geq 10$ mag, we interpret that the dependence of $N(C^{18}O)$ on A_V deviates from the linear relationship. The possible reasons are described below;

(1) Optical depth of $C^{18}O$

The column density of $C^{18}O$ which reaches optical thickness becomes 2.4×10^{15} (N/cm^2). This seems to be unlikely as a posible reason, although the parameters used to derive $N(C^{18}O)$ have much unceirtanty.

(2) Beam dilution

Our estimation of A_V is effectively made with a very high spatial resolution because field stars were observed as light source, while the beam diameter is 17" for Sunada & Kitamura and 1'.6 for Frerking et al. Thus a much large area is observed in radio observations than in infrared observations. The scatter for the relationship between A_V and $C^{18}O$ is predicted if there is density distribution in the beam. There are 3 objects with $A_V \sim 20$ mag, namely, Elias 16, Tamura 8 and HC1109. Both Tamura 8 and HC1109 are located in a filament of TMC1 and the column density around the objects are also high, while Elias 16 is located at near peak of a clump of L1527 and there is density gradient. Therefore the column density of Elias 16 is slightly smaller than those of Tamura 8 and HC1109.

In contrast, Kim 43 has A_V of 0.97 mag and $N(C^{18}O)$ of 6.8×10^{14} (N/cm^2), and therefore, there are some denser regions inside the beam than that of the direction of the object.

Whittet et al. (1985) discussed the relationship among $N(^{13}CO)$, A_V, and the optical depth of solid CO, and A_V. The absorption of solid CO whose absorption band head is at 4.67μm, is detected for $A_V > 6$ mag, and this is just coincident with the deviation of the linear relationship between $N(^{13}CO)$ and A_V. The dependence of $N(^{13}CO)$ and A_V deviates from the linear relationship for $A_V > 6$ mag, too. They concluded that the saturation of $N(^{13}CO)$ is partially due to the depletion of CO onto the dust. However, the effect of depletion is not seen in the relation between $N(C^{18}O)$ and A_V. Thus the effect of beam dilution is probably more dominant than that of the depletion.

Table 3-1-1. A_V vs. $N(C^{18}O)$.

objects	A_V (mag)	$N(C^{18}O)$ (10^{+} N/cm^2)	place
Elias 16*	21.6	12.9	L1527
HC1109_20	19.4	14.8	TMC1
Tamura 8	21.4	17.0	TMC1
Elias 15†	14.5	11.7	TMC1-A
Kim 59	9.12	7.16	-
Kim 49	8.52	9.74	-
Kim 58	8.16	7.84	-
Kim 52	6.24	7.21	-
Kim 46	6.12	5.64	L1527
Kim 32	8.64	10.9	TMC1-A
Kim 34	4.32	0.996	-
Kim 23	4.96	7.99	TMC1-A
Kim 29	4.56	2.80	TMC1-A
Kim 30	2.16	3.01	-
Kim 45	5.11	3.43	-
Kim 13	4.56	4.97	-
Kim 65	4.56	2.32	-
HD283809	3.72	6.64	TMC1
HD29647	2.40	3.69	TMC1
Kim 43	0.97	6.82	-

* A_V = 20.6 mag, $N(C^{18}O)$ = 11.1-∞, by Frerking et al. 1982.

† A_V = 13.3 mag, $N(C^{18}O)$ = 10.8-∞, by Frerking et al. 1982.

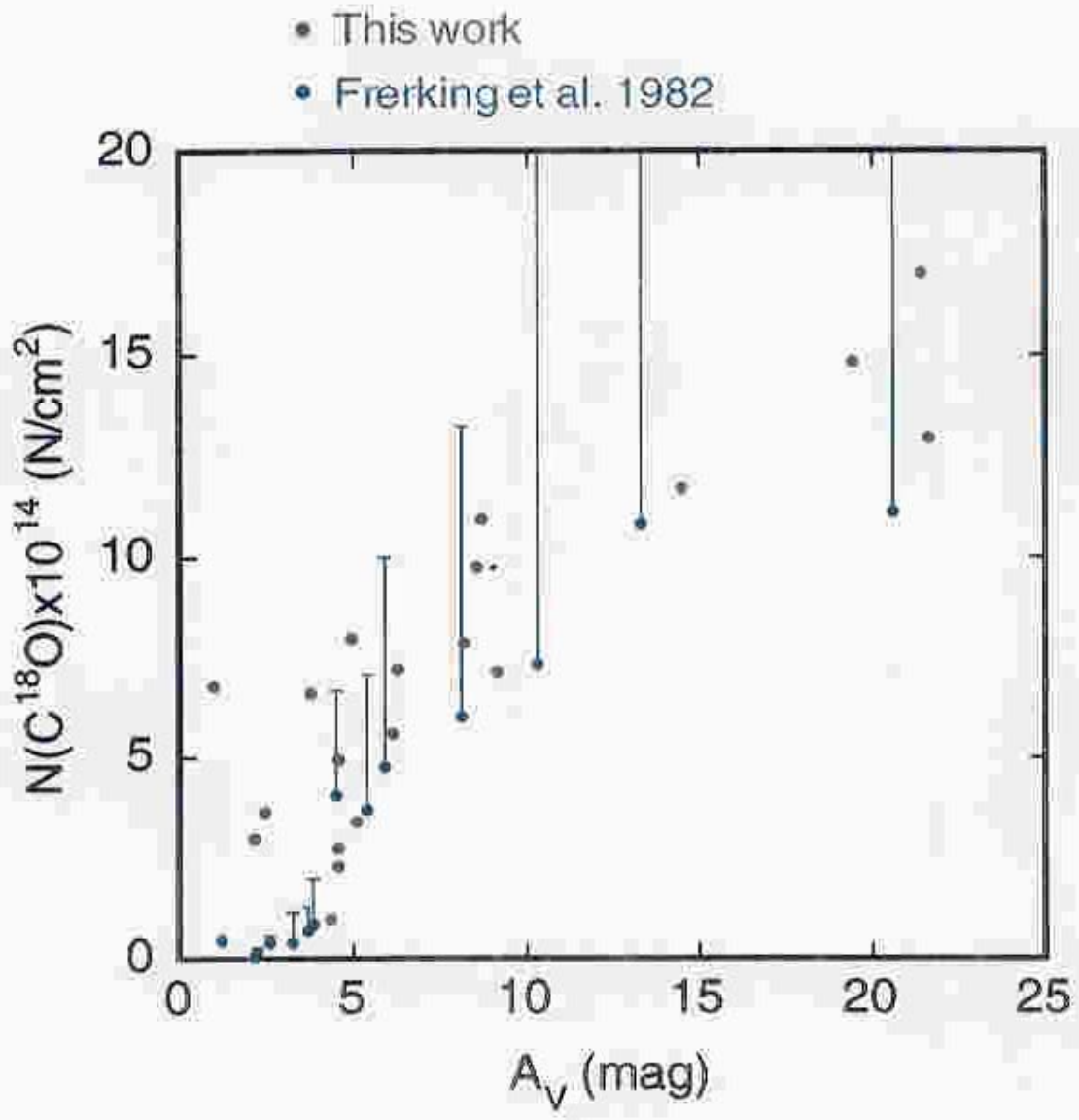

Fig. 3-1-7. Relationship between A_V and $N(C^{18}O)$.

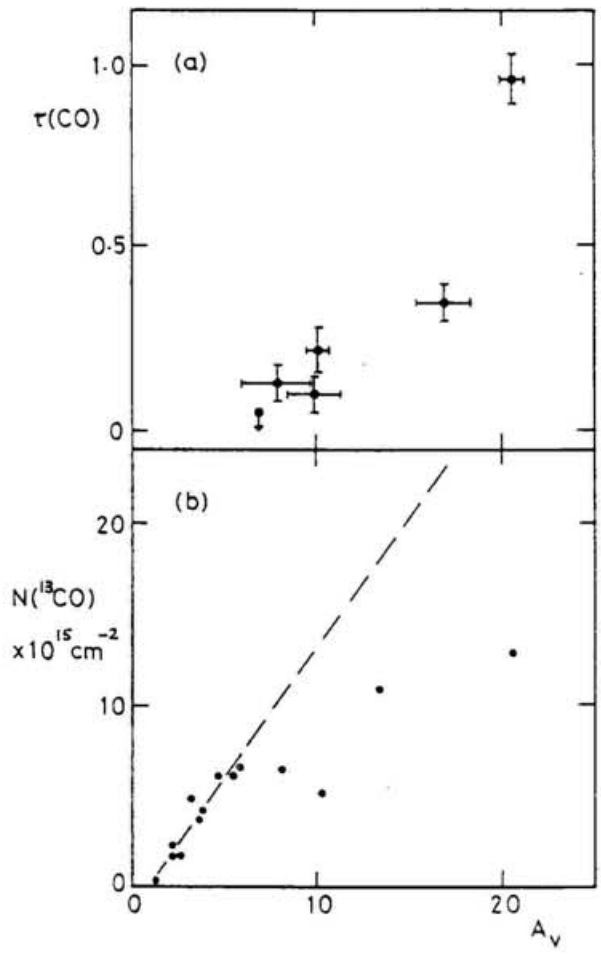

Fig. 3-1-8. Relationship between N(^{13}CO), A_v and the optical depth of solid CO (Whittet et al. 1985)

3-2. Interstellar extinction in Heiles Cloud 2

When we tried a correction of reddening for our data described in section 2-2-1-3, we found that the standard extinction law, $A_\lambda \propto \lambda^{-1.8}$, cannot be adopted for the most objects. Therefore, we need to derive the extinction law in Heiles Cloud 2 from our data in this section. Furthermore, we will try to estimate the size distribution and chemical component of the dust in this region which is expected by calculation of Mie scattering theory.

3-2-1. PASP2 observation of interstellar extinction

First we tried to fit the continuum of the PASP2 spectra between J and K with adopting the standard extinction law. The results of Elias 16, Kim 6 and Kim 83 are shown as purple dashed curves in Fig. 3-2-1. For Elias 16 and Kim 6, there is a significantly discrepancy for wavelengths longer than 2.0μm. The blue dashed curve is the result that the continuum is fitted between K and L′ with index α of 1.8. This method is often used in 3μm band spectroscopy. In this case, there is a significant discrepancy between J and H.

The green solid curve is the result of the method adopted in this reduction, namely index α of $A_\lambda=\beta\lambda^{-\alpha}$ is derived by E_{H-K} and $E_{K-L'}$. Good fittings are obtained for all objects. In this method, the index a is determined 2.22, 3.21, 2.53 for Kim 83, Kim 6 and Elias 16, respectively. These values are larger than index of standard extinction law.

In addition, the result of derived index α for the objects with both the errors E_{H-K} and $E_{K-L'}$ larger than 1σ is shown in Fig. 3-2-2. The index is larger than 1.8 for the most objects and a mean value is 2.6. It is difficult to determine the extinction law for the objects with smaller color excess (E_{H-K} < 1). For Kim 83, a good fitting is obtained for all cases, but, the color excess of E_{H-K} is small (E_{H-K}=0.16), therefore the fitting error is small, too.

In Fig. 3-2-3, a mean extinction curve of our 20 objects with over 1 σ of error of both E_{H-K} and $E_{K-L'}$ is shown. The horizontal axis is wavenumber (1/μm) and the vertical axis is extinction $E_{\lambda-K}/E_{H-K}$. The red filled circles denote obtained data and red dashed curve denote fitted curve by the following equation,

$$\frac{E_{\lambda-K}}{E_{H-K}} = e\lambda^{-\alpha} - R_K. \qquad (3\text{-}7)$$

This curve shows a good fit between λ=1.3 and 4.2μm.

In Table 3-2-1, our result is compared with previous one, which is already reviewed in Table 1-2-6 in section 1-2-2-1. Elias (1978) and Straizys (1985) investigated toward the Taurus dark cloud. Although the power law index was not mentioned in these two literature, they become about 2.4. This shows our 3 observations obtained the same power law index and might suggest that the Taurus dark cloud has anomalous extinction law, power law index, compared to the diffuse region and ρ Oph dark cloud.

Table 3-2-1. Extinction law

Sample	Range	α	R_V	references
Diffuse region				
diffuse clouds	M to I	1.84±0.03	3.05±0.01	1
		1.64	~3.1	2
	4.5 to 1.5	1.85±0.05	-	3
	N to U	1.51	3.04	4
Dense clouds				
ρ Oph cloud	M to I	1.85±0.09	4.26±0.04	1
		1.8	4.3	5
Taurus dark cloud	N to V	2.4	3.5	6
		2.4	-	7
(Heiles Cloud 2)	**L′ to J**	**2.6**	**-**	**this work**
Herchel 36		-	5.3	8
Galactic center				
Tr 14/16	K to J	1.87	4.17	1
	N to J	-	3.09±0.03	9

1. Martin & Whittet 1990. 2. Savage & Mathis 1979. 3. Landini et al. 1984. 4. van de Hulst 1949. 5. Elias 1978b. 6. Straizys et al. 1985. 7. Elias 1978a. 8. Mathis 1990. 9. Rieke et al. 1985.

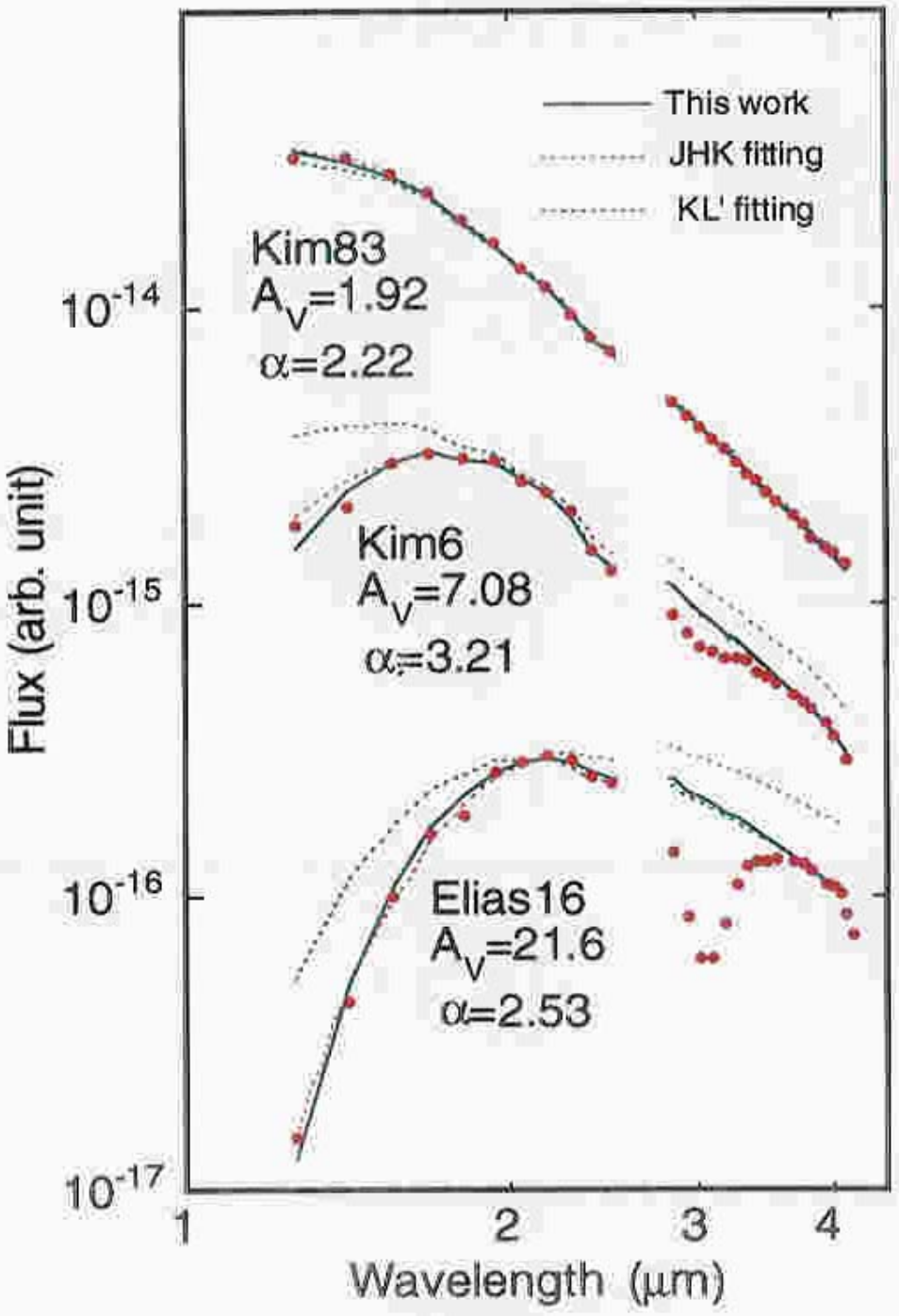

Fig. 3-2 -1. Power law fittings.

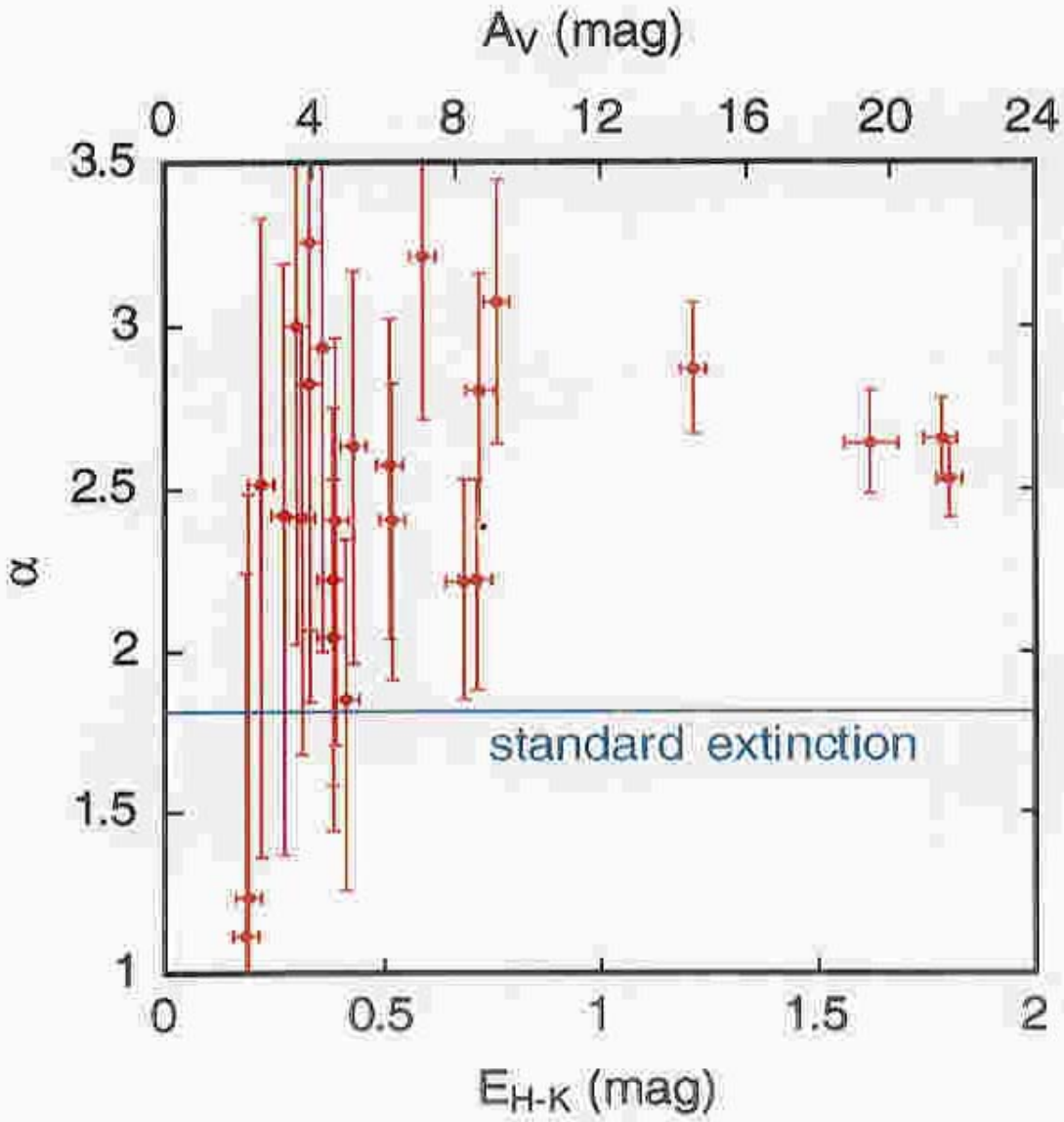

Fig. 3-2-2. Relationship between E_{H-K} and index α See also section 2-3-2.

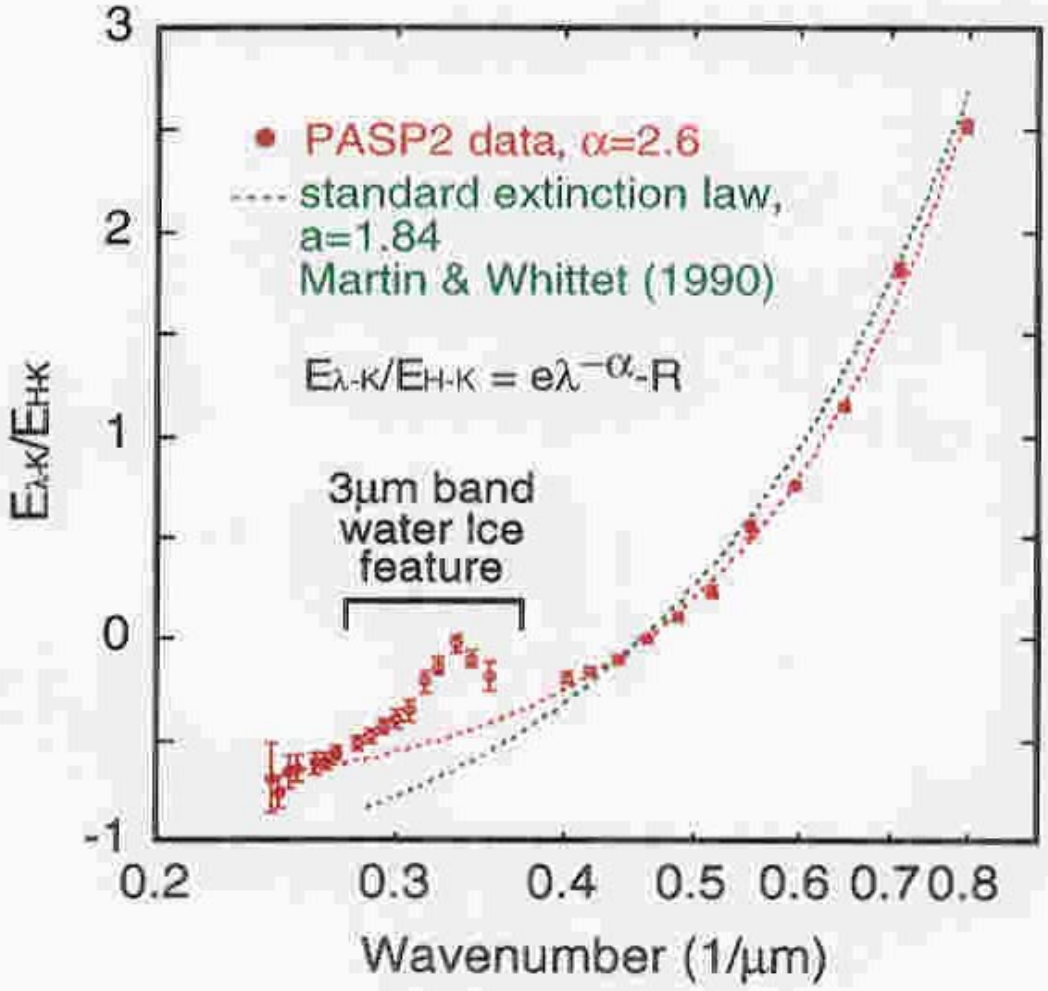

Fig. 3-2-3. The extinction law in Heiles Cloud 2.

3-2-2. Dust properties

We the try to estimate the size distribution and chemical component of dust in Heiles Cloud 2. The modified MRN model is used as an initial value of these parameters. The properties of Mie scattering theory is considered to modify these parameters, namely, express extinction with function of the dust particle size of a;

(1) $Q_{ext} \sim Q_{abs} \propto \lambda^{-1}$ when $a << 2\pi/\lambda$.

(2) $Q_{ext} \sim Q_{abs} \propto \lambda^{-4}$ when particle size a becomes larger and Rayleigh scattering is dominant.

(3) Q_{ext}~constant when $a >> 2\pi/\lambda$.

From above properties, (2) should be dominant to increase index of α.

<Modification of the size distribution>

In the MRN model, number density n(a) is proportional to $a^{-3.5}$ and the range of size is $0.005<a<0.25$ (μm). We consider following size distribution:

(1) $n(a) \propto a^{-1.5}$, $0.005<a<0.25$ (μm)

(2) $n(a) \propto a^{-1.5}$, $0.1<a<0.25$ (μm)

(3) Only 0.18μm

The power indices for these cases and the MRN model are summarized in Table 3-2-2.

In the case (3), the power index becomes a maximum.

Table 3-2-2. Effect of modulation of size distribution

size distribution	power index
MRN model	2.07
$n(a) \propto a^{-1.5}$, $0.005<a<0.25$ (μm)	2.27
$n(a) \propto a^{-1.5}$, $0.1<a<0.25$ (μm)	2.26
only 0.18μm	2.40

<Modification of the chemical component>

In the modified MRN model, bear dust particle has graphite and silicate, whose composition is graphite : silicate = $10^{-25.16}$:$10^{-25.11}$ (Draine & Lee 1984). The complex refractive indices of these materials are m_g=4.6-2.6i and m_s=1.7-0.03i, respectively, and graphite with large imaginary part of refractive index

has strong absorption while silicate with small has weak absorption. Since the Mie scattering theory predicts that the power index for weaker absorption is larger than that for strong absorption, we consider the three cases to increase the silicate abundance:

(1) Graphite : Silicate = 1 : 2

(2) Graphite : Silicate = 1 : 10

(3) Only silicate

The power indices for these case includes MRN model are calculated as in Table 3-2-3.

As we expect, the power index increases with increasing the ratio of silicate.

Table 3-2-3. Effect of modulation of chemical component

size distribution	power index
modified MRN model	2.07
Graphite : Silicate = 1 : 2	2.11
Graphite : Silicate = 1 : 10	2.30
Only silicate	2.53

<Discussion>

According to the above consideration, the dust is expected to have:

(1) Anomalous size distribution, and/or

(2) small abundance of graphite.

Seab et al. (1987) derived extinction curve in UV for HD29647 in Heiles Cloud 2 and other 7 bright stars. Their extinction curve which is shown in Fig. 3-2-4. The solid curve is standard extinction curve and the solid curve with vibration is thier data. Weak absorption feature at 220nm appears for HD29647. Both (1) and/or (2) can be adopted as possible reasons. These two results will support that the dust in Heiles Cloud 2 has an anomalous size population and/or small abundance of graphite.

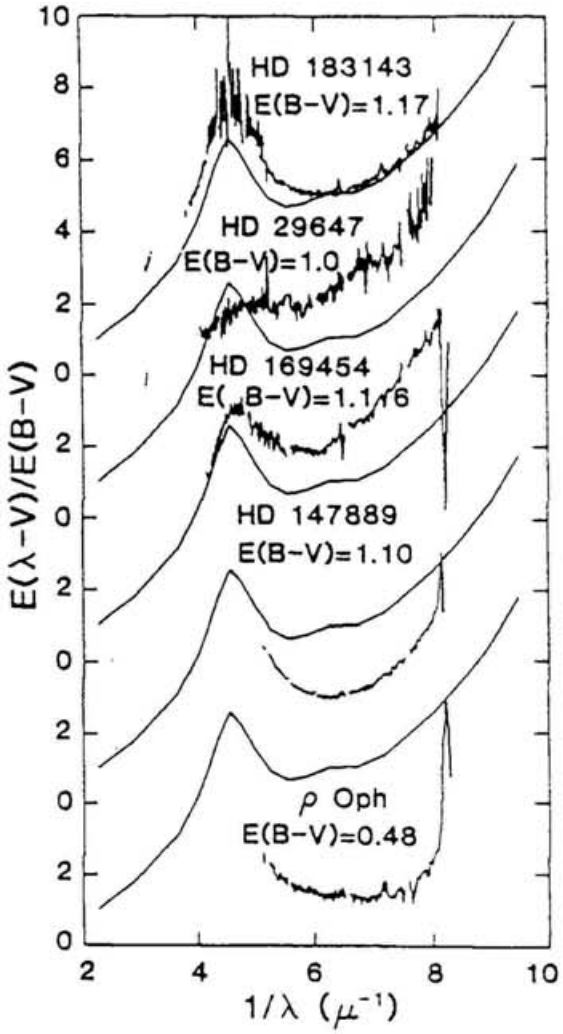

Fig. 3-2-4. UV extinction curve (Seab et a. 1981)

Conclusion

We have conducted near-infrared spectroscopic observations toward the Taurus molecular cloud. The spectra between 1.3 and 4.2μm for 62 background stars shining through Heiles Cloud 2, a part of the Taurus molecular cloud, have been obtained by using the PASP2. Spectral type, visual extinction A_V, and water ice depth at 3.1μm τ_{ICE} have been estimated for 55 out of the 62 stars.

The depth of water ice toward the position of the objects is plotted in a two-dimensional way, regarded as a "water ice map". The map is compared with the millimeter $C^{18}O$ map. These maps clearly show that the water ice is detected toward the high column density region of filaments and clumps and its absorption depth systematically decreases toward the outer region. Water ice is not detected outside the cloud delineated by $C^{18}O$.

The relationship between A_V and τ_{ICE} shows that water ice is detected when A_V is greater than 2~5 mag and τ_{ICE} proportionally increases with increasing A_V. The slope of the relationship, τ_{ICE}/A_V, is 0.067, which implies that 10% of oxygen atom depleted into the water ice. This result is consistent with that of Whittet et al. (1988), although the threshold of detecting water ice has a significant scatter in our data.

Geometrical structure of the dense cloud is modeled in a simple way for an explanation of the scatter of the A_V threshold. The variation in the threshold is due to the different contribution of the inner water-containing portion of the cloud along the line of sight. Our geometrical model could explain that the A_V threshold has variations of 2~5 mag, reproducing the observational results.

The water ice band feature of too deeply embedded low mass YSOs (also observed by ourselves for the first time) and field stars with sufficiently large absorption were compared. The field stars have similar profiles with each other, therefore absorption feature of low mass YSOs at 3.4μm seem to be deeper than that of field stars. This might suggest that dust around the YSOs is deformed to change the absorption feature.

Interstellar extinction for Heiles Cloud 2 has also been discussed. We

have found that the power law of the standard diffuse region can be used for the limited wavelength, between J and K, and between K and L′, but it cannot fit the obtained continuum spectra for the whole wavelength range between 1.3 and 4.2 μm. The indices α of the power law of each object was determined by using E_{H-K} and $E_{K-L'}$. The indices are significantly different from that for the standard diffuse region in many objects, suggesting that the reddening law in Heiles Cloud 2 might be peculiar.

Appendix 1. Previous observations for YSOs.

Table A1-1. Previous observations for YSOs

Region	Objects	τ_{ICE}	Nature	References
Taurus	Elias 1	0.51	PMS	1
	Elias 2	<0.05		
	Elias 7	0.52		
	IC2087 IRS	0.80		
	Elias 23	0.4		
	Tamura 12	0.06		
	HK Tau	0.20		
	HL Tau	0.85		2,3
	XL Tau	<0.05		2
	XZ Tau	0.12±0.02		3
	DG Tau	0.13±0.02		
	T Tau	0.29±0.02		
	FS Tau	0.33±0.05		
	L1536 IRS	0.72±0.15	proto-star	
	L1551 IRS5	2.1±0.2		
	L1489 IRS	2.9±0.2		
Perseus	HH7-11 IRS	0.77±0.05	proto-star	
	NGC1333SSV12	2.9±0.2		
	B5 IRS1	1.0±0.2		
ρ Ophiuchi	Elias 21	0.77±0.1	proto-star	4
	Elias 29	1.8±0.05		
	Elias 33	1.0±0.05		
	WL 5	2.0±0.5		
	WL 6	2.1±0.2		
	WL 12	1.2±0.2		
	WL 16	1.0±0.1		
	Elias 23	0.23±0.03	PMS	
	Elias 24	0.21±0.03		
	Elias 27	0.26±0.1		
	Elias 28	0.18±0.03		

Table A1-2. Previous observations for YSOs

Region	Objects	τ_{ICE}	Nature	References
ρ Ophiuchi	Elias 30	0.22±0.03	PMS	4
	Elias 49	<0.05		
	Elias 9	0		
	Elias 18	0.19±0.05		
	Elias 19	0.29±0.1		
	Elias 25	0.21±0.03		
	Elias 32	1.1±0.2		
	Elias 36	0.26±0.05		
	SR 3	0.008±0.01		5
	GS 31	0.032±0.015		
	GS 32	0.028±0.03		
	GS 26	0.175±0.06		
	VS 18	1.05±0.1		
	GS 30	0.694±0.07		
	VS 17	1.05±0.1		
	VS 26	3.1±0.5		
	RNO 91	1.29		6
Corona Australis	SVS 2	0.25	PMS	7
	SVS 4	1.58		
	SVS 20	1.0		
	HH100-IR	0.9±0.1	proto-star	8
	TS 2.5 (IRS5)	1.7±0.3	Association	
	TS 13.1	0.7±0.1	Embedded	8,9
	R1 (IRS7)	2±0.5		
	VVGA-IR	0.4±0.1	Association	8
	R CrA	0.2±0.1	Visible	8,9
	T CrA	0.18±0.05		
	S CrA	0.26±0.05		
	TY Cr A	0		8
	DG CrA	0		

Table A1-3. Previous observations for YSOs

Region	Objects	τ_{ICE}	Nature	References
Corona Australis	HD176368	0		8
	HH54	-	proto-star	10
	HH57	-		
	TS 2.4	2.3±0.2		9,10
Orion	BN	1.57±0.04		5,11
	NGC2024 No.1	0±0.04		5
	NGC2024 No.2	1.3±0.1		
Other Massive Star Forming Regions	W3/IRS5	3.48	Massive YSOs	12
	Mon R2/IRS2	2.54		
	Mon R2/IRS3	1.14		
	S255/IRS1	1.48		
	GL961E	2.46		
	GL2591	0.92		
	W33A	>5.4		13
	S140/IRS1	1.28		
	NGC7538/IRS1	1.29		
	NGC7538/IRS9	3.28		
Other Low-mass Star Forming Regions	AS 353	0.15±0.05	PMS	3
	PV Cep	0.48±0.03		
	Elias 1-12	0.06±0.05		

1. Whittet et al. 1998, 2. Whittet et al. 1983, 3. Sato et al. 1990, 4. Tanaka et al. 1990, 5. Harris et al. 1978, 6. Weintraub et al. 1994, 7. Eiroa & Hodapp 1989, 8. Chen & Graham 1993, 9. Tanaka et al. 1994, 10. Graham & Chen 1991, 11. Gillett & Forrest 1973, 12. Smith et al. 1989, 13. Willner et al. 1982.

Appendix 2. Extinction coefficient - for calculation of interstellar extinction

The extinction coefficient is derived by van de Hulst (1949) and is based on Mie's scattering theory. Here, some useful extinction coefficients for calculation of MRN model and icy grain will be described.

Notations of some common parameters:

n_1: refractive index of sphere

n_2: refractive index of coating material

a_1: radius of sphere

a_2: thickness of coating

λ: wave length of star light

k: wavenumber, $k= 2\pi/\lambda$

q_1: size parameter, $q_1=ka_1$

q_2: size parameter, $q_2=k(a_1+a_2)$

(1) Single sphere (for standard model of dust)

Except of treatment of complex problems of polarization, shape of interstellar dust is usually employed as sphere. The extinction coefficient of Q_{ext}, which is written in Eq. (1-10) in section 1-2-2, is expressed by,

$$Q_{ext} = \frac{2}{q_1^2}\Re\sum_{\ell=1}^{\infty}(2\ell+1)\left({}^{e}B_\ell+{}^{m}B_\ell\right), \qquad \text{(A2-1)}$$

where ${}^{e}B_\ell$ and ${}^{m}B_\ell$ are given by,

$$\begin{aligned} {}^{e}B_\ell &= \frac{n_1\psi_\ell(n_1q_1)\psi_\ell'(q_1)-\psi_\ell'(n_1q_1)\psi_\ell(q_1)}{n_1\psi_\ell(n_1q_1)\zeta_\ell'(q_1)-\psi_\ell'(n_1q_1)\zeta_\ell(q_1)}, \\ {}^{m}B_\ell &= \frac{n_1\psi_\ell'(n_1q_1)\psi_\ell(q_1)-\psi_\ell(n_1q_1)\psi_\ell'(q_1)}{n_1\psi_\ell'(n_1q_1)\zeta_\ell(q_1)-\psi_\ell(n_1q_1)\zeta_\ell'(q_1)}. \end{aligned} \qquad \text{(A2-2)}$$

Furthermore, scattering coefficient Q_{sca} and absorption coefficient Q_{abs} are expressed by,

$$\begin{aligned} Q_{sca} &= \frac{2}{q_1^2}\sum_{\ell=1}^{\infty}(2\ell+1)\left(\left|{}^{e}B_\ell\right|^2+\left|{}^{m}B_\ell\right|^2\right), \\ Q_{abs} &= Q_{ext}-Q_{sca}. \end{aligned} \qquad \text{(A2-3)}$$

In Eq. (A2-2) and (A2-3), $\psi_\nu(\rho)$, $\chi_\nu(\rho)$ and $\zeta_\nu(\rho)$ are the Riccati-Bessel functions and are expressed by using the ν-ordered Bessel function $J_\nu(\rho)$, Neumann function $Y_\nu(\rho)$ and Hankel function $H_\nu(\rho)$,

$$\psi_\ell(\rho) = \sqrt{\frac{\pi\rho}{2}} J_{\ell-\frac{1}{2}}(\rho),$$

$$\chi_\ell(\rho) = -\sqrt{\frac{\pi\rho}{2}} Y_{\ell-\frac{1}{2}}(\rho), \qquad \text{(A2-4)}$$

$$\zeta_\ell(\rho) = \sqrt{\frac{\pi\rho}{2}} H_{\ell-\frac{1}{2}}(\rho) = \psi_\ell(\rho) - i\chi_\ell(\rho).$$

The differentiation of these functions are given by,

$$\Phi'_\ell(\rho) = \Phi_{\ell-1}(\rho) - \frac{\ell}{\rho}\Phi_\ell(\rho), \qquad \text{(A2-5)}$$

where $\Phi(\rho)$ is $\psi(\rho)$, $\chi(\rho)$ or $\zeta(\rho)$.

(3) Anisotropic material (for graphite)

Graphite, which is one of the main component of interstellar dust, is anisotropic material. Thus it has two principal indices of refraction. In actual dust, effective Q_{ext} is derived as mean value of Q_{ext} with each refractive index, since optical axis may have any direction with same probability.

The extinction coefficient is defined for each refractive index and these are written Q_o and Q_e, where Q_o is for ordinal wave and Q_e is for extra ordinal wave. The effective coefficient Q_{eff} can be approximately as,

$$Q_{eff}=(2/3Q_o + 1/3Q_e). \qquad \text{(A2-6)}$$

(4) Mixture (Especially Graphite and Silicate)

In case of a dust model proposed Drain and Lee (1984), in which there are graphite core and silicate core, effective extinction coefficient Q_{eff} is given by summation of each extinction coefficient with mixing ratio,

$$Q_{eff}=A_{sil}Q_{sil}+A_{gra}Q_{gra}. \qquad \text{(A2-7)}$$

Where A_{sil} and A_{gra} are mixing ratio for silicate and graphite, respectively and Q_{sil} and Q_{gra} are extinction coefficients for silicate and graphite, respectively.

(5) Coated sphere (for icy dust)

Consider dust with ice mantle with same thickness. The formulae of such situation are written in a reference (Bohren and Huffmann, 1983).

Although the basic formulae are similar to (A2-1) and (A2-3), q_1 before sigma must be replace q_2 and the coefficient ${}^eB_\ell$ and ${}^mB_\ell$ must be redefined as,

$$
{}^{e}B_{\ell} = \frac{\psi_{\ell}(q_2)\left\{\psi'_{\ell}(n_2 q_2) + {}^{e}A_{\ell}\chi'_{\ell}(n_2 q_2)\right\} - n_2\psi'_{\ell}(q_2)\left\{\psi_{\ell}(n_2 q_2) + {}^{e}A_{\ell}\chi_{\ell}(n_2 q_2)\right\}}{\zeta_{\ell}(q_2)\left\{\psi'_{\ell}(n_2 q_2) + {}^{e}A_{\ell}\chi'_{\ell}(n_2 q_2)\right\} - n_2\zeta'_{\ell}(q_2)\left\{\psi_{\ell}(n_2 q_2) + {}^{e}A_{\ell}\chi_{\ell}(n_2 q_2)\right\}},
$$

$$
{}^{m}B_{\ell} = \frac{n_2\psi_{\ell}(q_2)\left\{\psi'_{\ell}(n_2 q_2) + {}^{m}A_{\ell}\chi'_{\ell}(n_2 q_2)\right\} - \psi'_{\ell}(q_2)\left\{\psi_{\ell}(n_2 q_2) + {}^{m}A_{\ell}\chi_{\ell}(n_2 q_2)\right\}}{n_2\zeta_{\ell}(q_2)\left\{\psi'_{\ell}(n_2 q_2) + {}^{m}A_{\ell}\chi'_{\ell}(n_2 q_2)\right\} - \zeta'_{\ell}(q_2)\left\{\psi_{\ell}(n_2 q_2) + {}^{m}A_{\ell}\chi_{\ell}(n_2 q_2)\right\}},
\tag{A2-8}
$$

where ${}^{e}A_{\ell}$ and ${}^{m}A_{\ell}$ are

$$
{}^{e}A_{\ell} = \frac{n_2\psi_{\ell}(n_2 q_1)\psi'_{\ell}(n_1 q_1) - n_1\psi'_{\ell}(n_2 q_1)\psi_{\ell}(n_1 q_1)}{n_1\psi_{\ell}(n_1 q_1)\chi'_{\ell}(n_2 q_1) - n_2\psi'_{\ell}(n_1 q_1)\chi_{\ell}(n_2 q_1)},
$$

$$
{}^{m}A_{\ell} = \frac{n_2\psi_{\ell}(n_1 q_1)\psi'_{\ell}(n_2 q_1) - n_1\psi'_{\ell}(n_1 q_1)\psi_{\ell}(n_2 q_1)}{n_1\psi'_{\ell}(n_1 q_1)\chi_{\ell}(n_2 q_1) - n_2\psi_{\ell}(n_1 q_1)\chi'_{\ell}(n_2 q_1)}.
\tag{A2-9}
$$

References

Allamandola, L. J., & Sandford, S. A., 1988, in *Dust in the universe* (Cambridge University Press).

Aitken, D. K., Smith, C. H., & Roche, P. F., 1989, Mot. Not. R. astr. Soc., **236**, 919.

Bergin, E. A., & Langer, W. D., & Goldsmith, P. F., 1995, Ap. J., **100**, 1134.

Bessell, M. S., & Brett, J. M., 1988, PASP, **100**, 1134.

Blitz, L., & Shu. F. H., 1980, Ap. J., **238**, 148.

Bohlin, R. C., Savage, B. D., & Drake, J. F., 1978, Ap, J., **224**, 132.

Bohren, C. F., & Huffman, D. R., 1983, *Absorption and Scattering of Light by Small Particles* (New York: Wiley).

Boland, W., & de Jong, T., 1982, Ap. J., **261**, 110.

Born, M., & Wolf, E., *Principles of Optics* (Pergamon press)

Chen, W. P., & Graham, J. A., 1993, Ap. J, **409**, 319.

Chronological Scientific Tables, 1997, National Astronomical Observatory of Japan (ed.), Maruzen Co., Ltd. p. 188.

Code, A. D., Davis, J., Bless, R. C., & Hanbury B, R. 1976, Ap. J., **203**, 417.

Cohen, M., 1975, Mon. Not. R. astr. Soc., **173**, 279.

Cohen, M. & Kuhi, L. V., 1979. Astrophys. J. Suppl. **48**, 743.

Crutcher, M. R., 1985. Ap. J., **288**, 604.

Draine, B. T. & Salpeter, E. E., 1979, Ap. J., **231**, 438.

Draine, B. T. & Lee, H. M., 1984, Ap. J., **285**, 89.

Draine, B. T., 1985, Ap. J. S, **57**, 587.

Duley, W. W. & Smith, R. G., 1995, Ap. J., **450**, 179.

Eiroa, C., & Hodapp, K.-W., 1989, A&A, **210**, 345.

Elias, J. H., 1978a, Ap. J., **224**, 857.

Elias, J. H., 1978b, Ap. J., **224**, 453.

Flannery, B. P., Roberge, W., & Rybicki, G. B., 1980, Ap. J., **236**, 598.

Frerking, M. A., Langer, W. D., & Wilson, R. W. 1982, Ap. J., **262**, 590.

Geballe, T. R., 1986, A&A, **162**, 248.

Gillett, F. C., & Forrest, W. J., 1973, Ap. J., **179**, 483.

Goto, M., Sasaki, Y., Imanishi, M., Nagata, T., & Jones, T. J., in preparation

Graham, J. A., & Chen, W. P., 1991, Ap. J., **102**, 1405.

Hagen, W., Allamandola, L. J, & Greenberg, J. M., 1979, Ap&SS, **65**, 215.

Harris, D. H., Woolf, N. J., & Rieke, G. H., 1978, Ap. J., **226**, 829.

Hayashi, C., 1981, Prog. Theor. Phys. Suppl. **70**, 35.

Itoh, Y., 1995, Master thesis, university of Tokyo.

d'Hendecourt, L. B., Allamandola, L. J., Baas, F., & Greenberg, J. M., 1985, A&A, **109**, L12.

d'Hendecourt, L. B., Allamandola, L. J., & Greenberg, J. M., 1985, A&A, **152**, 130.

Honda, K., 1997, Master thesis, Nagoya university.

Jenniskens, P., Baratta, G. A., Akira, K., de Groot, M. S., Greenberg, J. M., & Strazzulla, G., 1993, Proceeding of "Grain Formation Workshop vol. XV", (Research Group of Grain Formation)

Jones, T. J., & Hayland, A. R., 1980, Mon. Not. R. astr. Soc., **192**, 359.

Jones, T. J., Michael A. Hyland, A. R., & Ruelas-Mayorga, A., 1981, Mon. Not. R. astr. Soc., **197**, 413.

Kim, C. Y., 1990, *Memories of the Faculty of Science, Kyoto University, Series A of Phys., Astrophys, Geophys. and Chem.*, vol. XXXVIII, 1.

Koorneef, J. 1983, Astr. Ap., **128**, 84.

Lacy, J. H., Bass, F. Allamandola, L. J., Persson, S. E., McGregor, P. J., Lonsdale, C. J., Geballe, T. R., & van de Bult, C. E. P., 1984, Ap. J., **276**, 533.

Landini, M., Natta, A., Oliva, E., Salinari, P., & Moorwood, A. F. M., 1984, Astr. Ap., **134**, 284.

Larson, R. B., 1985, in *Structure and Dynamics of the Interstellar Medium*, eds. G. Tenorio-Tagle, M. Moles & J. Melnick (Springer-Verlag, Berlin).

Leger, A., Jura, M., & Omont, A., 1985, A&A, **144**, 147.

Martin, P. G., & Whittet. D. C. B., 1990, Ap. J., **357**, 113.

Mathis, J. S., Rumpl, W., & Nordsieck, K. H., 1977, Ap. J. **217**, 425.

Mathis, J. S., 1979, Ann. Rev. Astr. Ap., **28**, 37.

Merrill, K. M., Russell, R. W., & Soifer, B. T., 1976, Ap. J., **207**, 763.

Merrill, K. M., & Stein, W. A., 1976, PASP, **88**, 285.

Mie, G., Ann. d. Physik, 1909, **25**, 377.

Mizuno, A., Onishi, T., Yonekura, Y., Nagahama, T., Ogawa, H., & Fukui, Y., 1995, Ap. J., **445**, L161.

Nakagawa, K., & Nakagawa, Y., 1981, Prog. Theor. Phys. Suppl. **70**, 11.

Nandy, K., Thompson, G. I., Jamar, C., Monfils, A., & Wilson, R. 1975 Astr. Ap., **44**, 195.

Onishi, T., Mizuno, A., Kawamura, A., Ogawa, H., & Fukui, Y., 1996, Ap. J., **465**, 815.

Rieke, G. H., & Lebofsky, M. J., 1985, Ap. J., **288**, 618.

Sandford, S. A., & Allamandola, L. J., 1990, Ap. J, **355**, 357.

Sato, S., Nagata, T., Tanaka, M., & Yamamoto, T., 1990, Ap. J, **359**, 192.

Savage, B. D, & Mathis,J. S., 1979, Ann. Rev. Astr. Ap., **17**, 73.

Seab, C. G., Snow, T. P., & Joseph, Cl. L., 1981, A. J., **246**, 768.

Schutte, W. A., in *The cosmic Dust Connection* eds. J. M. Greenberg, 1995.

Schutte, W. A., & Greeberg, J. M., 1991, A&A, **244**, 190.

Smith, R. G., Sellgren, K., & Tokunaga, A. T., 1989, Ap. J., **344**, 413.

Smith, R. G., Sellgren, K. & Brooke, T., 1993. Mon. Not. R. Astron. Soc. **263**, 749.

Straizys, V., Wisniewski, W. Z. & Lebofsky, M. J., 1982, Astrophys. and Space Science **85**, 271.

Straizys, V., Cernis, K. & Hayes, D. S., 1985, Astrophys. and Space Science **112**, 251.

Tamura, M., Nagata, T., Sato, S. & Tanaka, M., 1987. Mon. Not. R. astr. Soc. **224**, 413.

Tanaka, M., Sato, S., Nagata, T., & Yamamoto, T., 1990, Ap. J., **352**, 724.

Tanaka, M., Nagata, T., Sato, S., & Yamamoto, T., 1994, Ap. J., **430**, 779.

Tielens, A. G. G. M. & Hagen, W., 1982. Astr. Astrophys., **114**, 245.

Tielens, A. G. G. M., Allamandola, L. J., Bregman, J., Goebel, J., d'Hendecourt, L. B., & Witteborn, F. C., 1984. Ap. J., **287**, 697.

van de Bult, C. E. P. M., Greenberg, J. M., & Whittet, D. C. B., 1985, Mon, Not. R. astr. Soc., **214**, 289.

van de Hulst, H. C. 1943, Ned. Tijdschr. v. Natuurkunde **10**, 251.

van de Hulst, H. C. 1949, Recherche Astron. Observatoire Utrecht **11**, part 2.

van de Hulst, H. C. 1975, *Light Scattering by Small Particles* (New York: Dover).

Weintraub, D. A., Tegler, S. C., Kastner, J. H., & Rettig, T., 1994, Ap. J., **423**, 674.

Westley, M. S., Baragiola, R. A., Johnson, R. E. & Baratta, G. A., 1995, Planetary and Space Science.

Whittet, D. C. B., Blades, J. C., 1980, Mon. Not. R. astr. Soc., **191**, 309.

Whittet, D. C. B., Bode, M. F., Longmore, A. J., Baines, D. W. T., Evans, A., 1983, Nature, **303**, 218.

Whittet, D. C. B., Longmore, A. J., & McFadzean, A. D., 1985, Mon. Not. R. astr. Soc., **216**, 45p.

Whittet, D. C. B., Bode, M. F., Longmore, A. J., Adamson, A. J., McFadzean, A. D., Aitken, D. K., & Roche, P. F., 1988, Mon. Not. R. astr. Soc.,

233, 321.

Whittet et al. 1988, in *Dust in the Universe*, Eds. by Bailey, M. E., & Williams, D. A., (Cambridge University Press).

Whittet, D. C. B., 1992, in *Dust in the Galactic Environment* (Cambridge University Press).

Willams, D. A., Hartquist, T. W., & Whittet, D. C. B., 1992, Mon. Not. R. astr. Soc., **258**, 599.

Willner, S. P., Gillet, F. C., Herter, T. L., Jones, B. Krassner, J., Merrill, K. M., Pipher, J. L., Puetter, R. C., Rudy, R. J., Russell, R. W., & Soifer, B. T., 1982, Ap. J., **253**, 147.